Exploring new catalysts for conversion of sustainable energy in µ-reactors
Study of mass-selected atoms, clusters, and nanoparticles

Krabbe, Alexander

Publication date:
2023

Document Version
Publisher's PDF, also known as Version of record

DTU Physics
Surface Physics and Catalysis

Exploring new catalysts for conversion of sustainable energy in μ-reactors

Study of mass-selected atoms, clusters, and nanoparticles

PhD Thesis

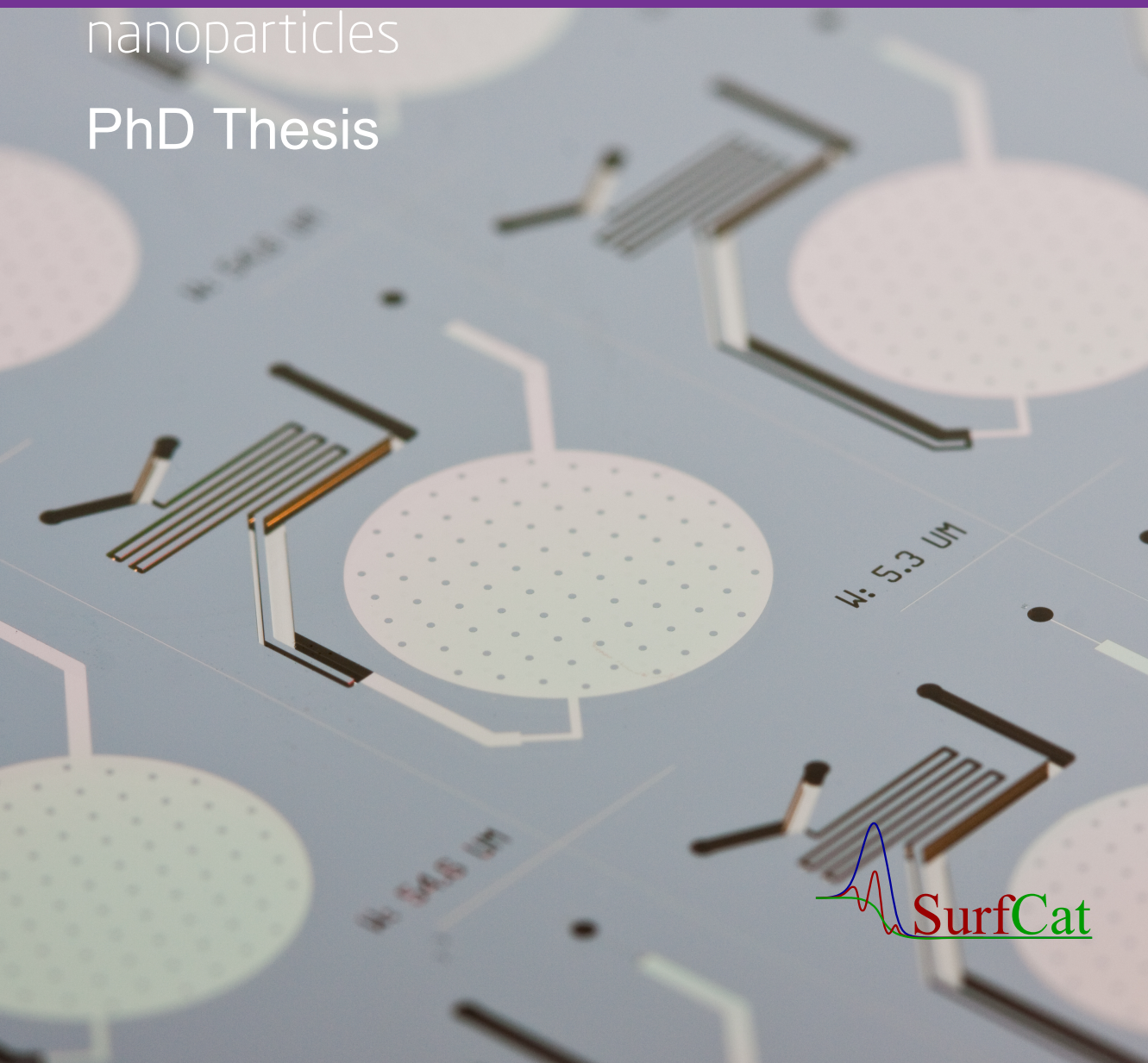

SurfCat

Exploring new catalysts for conversion of sustainable energy in μ-reactors
Study of mass-selected atoms, clusters, and nanoparticles

PhD Thesis
November, 2023

By
Alexander Leegaard Krabbe

Supervisor: Professor Ib Chorkendorff
Co-supervisor: Professor Jakob Kibsgaard

Cover photo: Thomas Pedersen
Published by: DTU, Surface Physics and Catalysis, Fysikvej, Building 312, 2800 Kgs. Lyngby Denmark
www.fysik.dtu.dk

Approval

The work described in this thesis was carried out under the supervision of Professor Ib Chorkendorff and Professor Jakob Kibsgaard. Over a period of five years from 2018 to 2023, including paternity leave, this thesis was prepared at the Section for Surface Physics and Catalysis, SurfCat, of the Department of Physics, at the Technical University of Denmark, DTU, as a partial requirement for the PhD degree at DTU.

Alexander Leegaard Krabbe

.....

Signature

.....

Date

Abstract

This PhD thesis investigates catalytic reactions under reaction conditions that is comparable to industrial catalysts.

Heterogeneous catalysis plays a pivotal role in the transition to a renewable energy future, moving away from fossil fuel-based energy sources and contributing to clean energy access for all, in accordance with United Nation (UN) Sustainable Development Goal 7 (SDG 7). In this thesis, a Si-based µ-reactors is used to investigate heterogeneous catalysis, bridging the pressure gap between traditional academic surface science and industrially viable catalytic reaction conditions.

The µ-reactor, a state-of-the-art testing platform, allows for activity testing and analysis of catalytic reactions under a wide range of conditions. In this work, the primary study is the investigation of AuTi mass selected nanoparticles in the size range of 2-8 nm for their potential application in thermal catalysis. By alloying Au with Ti, AuTi nanoparticles is expected to exhibit enhanced stability compared to Au on SiO_2, which is then evaluated systematically for their catalytic performance using the µ-reactor.

The key reaction studied in this thesis is CO oxidation, a well known process with industrial applications.

Through this work, the µ-reactor platform has demonstrated the versatility and potential as a powerful tool for investigating heterogeneous catalysis it is.

During this work, it has been important to enhance the technical aspects of the µ-reactor. This research examines the calibration processes of the quadrupole mass spectrometer (QMS). An understanding of this procedure is important, as it sets the stage for accurate and reliable data analysis in subsequent experimental stages. Complementing this is the validation the molecular flow through the capillary of the µ-reactor to enable calibration of gasses not available as a pure gas or as a gas mixture for direct calibration in the QMS. Technical effort is put into setting up and optimising protocols for using the µ-reactors in catalysis research. Detailed attention is given to the heating methods and monitoring of temperatures in vacuum, ensuring that the reactors are heated homogeneous and the true temperature is reported for optimal performance across various experimental scenarios.

The platform relies heavily on the anodic bonding procedure to hermetically close the reactor prior to testing. This step has proven to include huge variation and unreliable catalytic testing for the AuTi system investigated and effort is put into designing and conceptualising a new re-usable µ-reactor-platform for thermal catalysis as is the case for Electrochemical Catalysis (EC) and is proven to work for Photocatalysis.

Resume

Denne PhD-afhandling undersøger katalytiske reaktioner under reaktionsbetingelser, der er sammenlignelige med industrielle katalysatorer.

Heterogen katalyse spiller en afgørende rolle i overgangen til en fremtid baseret på vedvarende energi, hvor man bevæger sig væk fra energikilder baseret på fossile brændstoffer og bidrager til adgang til ren og billig energi for alle, i overensstemmelse med FN's verdensmål for bæredygtig udvikling (SDG 7). I denne afhandling udforskes brugen af Si-baserede µ-reaktorer til at undersøge heterogen katalyse, som kan agere bindeled i mellem traditionel UHV forsøg og industrielle katalytiske reaktionsbetingelser.

µ-reaktor platformen muliggør aktivitetstest og analyse af katalytiske reaktioner under forskellige reaktionsbetingelser med høj tryk og hurtig temperaturændringer. I dette arbejde er AuTi masse-selekteret nanopartikler i størrelsesorden 2-8 nm undersøgt for deres potentielle anvendelse i termisk katalyse med fokus på stabilitets potentialerne for metallegerigner med Ti. AuTi legeringen og Au nanopartikler er evalueret for deres katalytiske aktivitet og undersøgt for deres stabilitet på SiO_2,

Den primære reaktion, der studeres i denne afhandling, er CO oxidation, en velkendt proces som også bruges i industrien.

Gennem dette arbejde har µ-reaktorplatformen demonstreret potentialet som et kraftfuldt værktøj til at undersøge termisk heterogenkatalyse.

Under dette arbejde har det været vigtigt at forbedre de tekniske aspekter af µ-reaktoren. Denne afhandling undersøger kalibreringsprocesserne af kvadrupol-massespektrometeret (QMS). En forståelse af denne procedure er vigtig, da den danner grundlaget for nøjagtig og pålidelig dataanalyse i de efterfølgende eksperimenter. Dette suppleres af valideringen af flowet gennem µ-reaktorens kapillar for at muliggøre kalibrering af gasser, der ikke er tilgængelige som en ren gas eller gasblanding til direkte kalibrering i QMS. Der er optimeret protokoller til opvarmningsmetoderne og temperaturermålingerne i µ-reaktoren i vakuum, som sikrer, at reaktorerne opvarmes homogent, og den korrekte temperatur rapporteres for optimal udnyttelse af platformen på tværs af forskellige eksperimentelle scenarier.

Platformen er stærkt afhængig af anodisk bonding procedure for hermetisk at lukke reaktoren før aktivitets testning. Dette trin har vist sig at give stor variation i udfaldet af succesfulde µ-reaktorer og er den primære kilde til upålidelig katalytisk aktivitets testning for AuTi-system. Der er derfor lagt påbegyndt en indsats i at designe og udvikle en ny µ-reaktorplatform til genbrugelige µ-reaktorer til brug i termisk heterogenkatalyseforskning. Det er blevet gjort med succes for µ-reaktorer til brug i fotokatalyse.

Acknowledgements

I would like to express my sincere gratitude to the following individuals for their invaluable contributions and support throughout the preparation of this thesis:

First and foremost, I would like to express my deepest appreciation to my supervisors, Ib Chorkendorff and Jakob Kibsgaard, for their guidance, expertise, and encouragement throughout the entire process. Their support has been instrumental in the successful completion of this thesis.

I am also grateful to Ole Hansen, Peter Vesborg, Christian Damsgaard, and Stig Helveg for their thoughtful insights and exchange of ideas during our weekly meetings. Their input has been invaluable in shaping my research.

I would like to extend my heartfelt thanks to the floormanagers, Jakob Ejler Sørensen, Brian Peter Knudsen, Robert Jensen, and Kenneth Nielsen, for their technical support and troubleshooting when the going got tough.

Special thanks go to Niklas Secher, Karl Toudahl, Rikke Plougmann, Julius Lucas Needham, and Jens Ringsholm for their contributions in preparing nanoparticles, and to Olivia Fjord Sloth, Robert Steven Boyed, and Filippo Romeggio for their help in testing, analyzing, and improving the microreactor setup.

I would also like to express my gratitude to Stefan Kei Akazawa and Mads Lützen for their assistance with electron microscopy, and to my colleagues at Surfcat, especially Søren Scott, Thomas Smitshuysen, Helene Hagemann Jakobsen, Jakob Bruun Pedersen, Suzanne Zamany Andersen, and Degenhart Hochfilzer for their support, scientific discussions and camaraderie during lunch and coffee breaks.

Finally, I would like to acknowledge the unwavering love and support of my family, especially my wife Elise. Without her understanding and encouragement, this thesis would not have been possible.

Thank you all for being a part of this journey.

List of papers

Paper I

Degenhart Hochfilzer, Clara Aletsee, Kevin Krempl, Thomas Pedersen, Alexander Krabbe, Martin Tschurl, Ole Hansen, Peter Vesborg, Jakob Kibsgaard, Ueli Heiz, and Ib Chorkendorff
Enabling real-time detection of photocatalytic reactions by a re-useable micro-reactor
2024 Meas. Sci. Technol. 35 015903
DOI: 10.1088/1361-6501/acfe2c

Paper II

Soren B. Scott, Anna Winiwarter, Alexander Krabbe, Caiwu Liang, Kevin Krempl, Daisy Thornton, Rose Oates, Benjamin Moss, Reshma R. Rao, Ib Chorkendorff, Ifan E. L. Stephens, Kenneth Nielsen
The in-situ experimental data tool, ixdat: An open-source python package for electrochemistry data
In preparation, 2023
https://ixdat.readthedocs.io/en/latest/index.html, 2023

Not included

Paper III

Debasish Chakraborty, Thomas Erik Lyck Smitshuysen, Arvin Kakekhani, Sebastian Pirel Fredsgaard Jespersen, Sayan Banerjee, Alexander Krabbe, Nicolai Hagen, Hugo Silva, Justus Just, Christian Danvad Damsgaard, Stig Helveg, Andrew M. Rappe, Jens K. Nørskov, and Ib Chorkendorff
Reversible Atomization and Nano-Clustering of Pt as a Strategy for Designing Ultra-Low-Metal-Loading Catalysts
J. Phys. Chem. C 2022, 126, 38, 16194–16203
DOI: 10.1021/acs.jpcc.2c05213

Contents

Chapter 1

Introduction

As the world faces an energy crisis both to meet the increasing energy demand in the terawatt scale while moving away from fossil fuel based energy source, it is important to develop new, sustainable ways to produce chemicals and fuels [1, 2, 3]. Catalysts, which are usually nanoparticles with a high number of under-coordinated surface atoms, are necessary for chemical reactions to occur efficiently.

Catalysis plays a vital role in the energy transition towards a more sustainable future. As we shift from fossil fuels to renewable sources of energy, it is essential to develop efficient and cost-effective ways to convert these sources into usable chemicals. Catalysis enables us to achieve this by accelerating chemical reactions and increasing their selectivity, thus reducing waste and improving energy efficiency [4].

However, catalysis research faces an inherent problem between academic research, which is typically conducted on well-defined single crystals and under well-controlled atmospheres in ultra high vacuum chambers; and, industrial catalysis, which occurs at high pressures, temperatures, and with less well-defined atmospheres and catalysts. This so-called ”pressure gap” and ”material gap” pose significant challenges in translating fundamental insights gained from model systems to practical applications.

Several articles [5, 6, 7, 8] discuss the need to bridge this gap both computationally and experimentally and highlight the opportunities and challenges that is. These articles emphasize the importance of designing catalysts that can operate under industrial conditions, understanding the fundamental principles that govern intrinsic catalyst performance, and developing new experimental techniques that can capture the dynamic behavior of catalysts under real-world conditions.

Overall, catalysis research has a crucial role to play in the transition to a more sustainable energy future. The pressure and material gaps pose significant challenges that require innovative solutions, and the articles discussed above provide valuable insights into the opportunities and challenges associated with bridging these gaps. By developing new catalysts and understanding the fundamental principles that govern their performance under industrial conditions, we can make significant strides towards achieving a more sustainable and cleaner energy future.

By producing well-characterized mass-selected nanoparticles, we can manipulate the activity of these catalysts and study their relationship between structure and reactivity. The μ-reactor developed at SurfCat allows for measuring the activity of these nanoparticles, which is necessary for studying processes such as the hydrogenation of CO and CO_2 into methanol or higher alcohols [9]. In this PhD project the cluster source at SurfCat has been used to produce these mass-selected atoms, clusters, and nanoparticles for testing in the μ-reactor setup. The goal is to increase the understanding of catalytic activity and selectivity of mass-selected catalysts and potentially develop new catalysts for converting CO, CO_2, and N_2 into chemicals and fuels through hydrogenation.

1.1 Heterogeneous catalysis

Heterogeneous catalysis is a type of catalysis in which the catalyst and the reactants involved in the chemical reaction are present in different phases, usually as a solid catalyst and gaseous or liquid reactants. This contrast distinguishes it from homogeneous catalysis, where the catalyst and reactants exist in the same phase [10].

In heterogeneous catalysis, the reactant molecules interact with the surface of the solid catalyst, forming temporary bonds. This interaction typically leads to a weakening of the reactant's chemical bonds, making it easier for the reaction to occur. A potential energy diagram can be seen in figure 1.1 where the activation energy E_a for the reaction pathway with a catalyst is lower than without. The process can be broken down into several key steps:

Adsorption: The reactant molecules adsorb onto the catalyst's surface, which means they attach themselves through weak physical or stronger chemical interactions.

Dissociation: As the reactant molecules adsorb onto the surface, their bonds are weakened or broken, lowering the energy barrier needed for the reaction to occur.

Reaction: The activated reactants undergo the desired chemical reaction on the catalyst's surface, forming the product molecules.

Desorption: The product molecules detach from the catalyst's surface, freeing up active sites for new reactant molecules to adsorb and repeat the process.

A significant advantage of heterogeneous catalysis is that the solid catalyst can often be easily separated from the reaction mixture, making it convenient for industrial applications. Heterogeneous catalysis plays a vital role in numerous industrial processes, such as the production of ammonia through the Haber-Bosch process, the catalytic cracking of hydrocarbons in oil refining, and the reduction of automobile exhaust emissions [10].

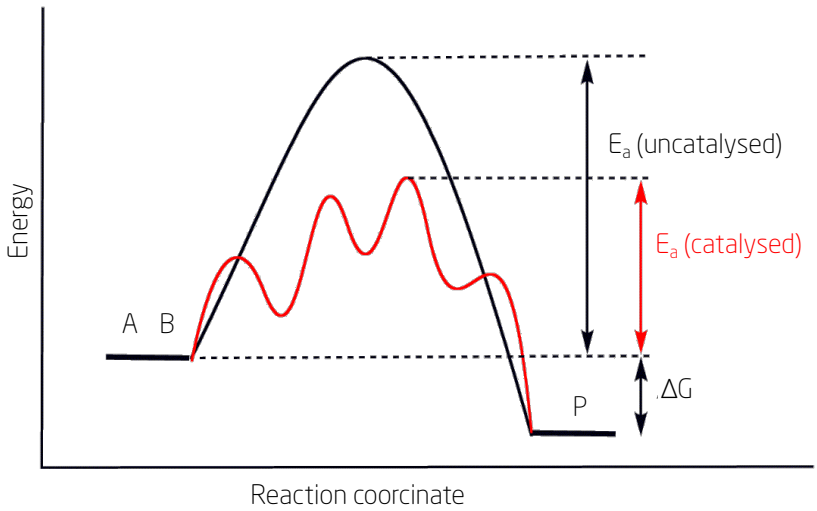

Figure 1.1: Simple potential energy diagram of an exothermic reaction. Adapted and updated from [11].

1.1.1 Studying surface science and catalysis

The study of catalysis is highly complex due to the numerous intermediate states and possible by-products, the time-scale at which the reactions occur and the diffusion on/off the catalytic surface making it challenging to investigate catalysts in action and fully understand their underlying mechanisms. Traditionally, catalysis has been developed through trial and error and knowledge of a catalyst's effects in a specific reaction [10]. However, to enhance academic knowledge and understand the physical properties of catalysis, investigations must take place in a highly controllable environment such as a ultra-high vacuum (UHV) chamber in which the reaction can occur.

To stress out the importance of good UHV to perform surface science experiments the langmuir unit can be used. One langmuir (1 L) is defined as the exposure equivalent of 10^{-6} Torr or 1.33×10^{-6} mbar in one second. Assuming every molecule that hits the surface sticks to it, i.e., has a sticking coefficient of one then, 1 langmuir corresponds to a monolayer of adsorbates on the surface. To prevent contaminants from covering the entire surface, the UHV pressure must be in the order of 10^{-10} mbar, which provides only a few hours of work time [12] before the entire catalytic surface has been exposed to crap from the vacuum chamber.

Although UHV is excellent for controlling the atmosphere, experiments conducted with this method has limitations. The experiments can provide information about the structural and electronic properties of surfaces and how reactions are influenced by adsorbates on surfaces [6, 10], but a single

crystal catalyst may behave entirely differently in UHV than under industrial conditions with high pressure (>30 bar) and high temperatures (>700 °C). This difference between UHV experiments and real catalyst applications is known as the pressure and material gap [6]. To bridge this gap, different in-situ techniques have been developed, and the introduction of chemical potential in density functional theory (DFT) has made it more common to combine UHV techniques with ab initio calculations [13]. To overcome this gap, the μ-reactor developed at DTU in the SurfCat group is an extremely useful tool [9]. By reducing the reactor volume and increasing the area to volume ratio, one can have better control of the reactants and their flow in the reactor over the catalyst. The small reactor volume results in a short residence time in the reactor, giving a fast time response. Moreover, by using this μ-reactor, one can study a catalyst under more realistic conditions. It is easy to expose the sample to a pressure of 2-3 bar and temperatures up to 300-500 °C and still use UHV techniques, such as a quadrupole mass spectrometer (QMS), to investigate the products, yielding a high sensitivity.

1.1.2 Kinetics of chemical reactions

Chemical kinetics plays a role in the field of heterogeneous catalysis as it helps to understand the rate and mechanism of chemical reactions occurring on the surface of the catalyst. Thermal catalysis is a process in which the reactants adsorb on the surface of a solid catalyst, and the resulting chemical reaction occurs on the surface at elevated temperatures [10].

The rate of the reaction on the surface of a catalyst can be described by the Langmuir-Hinshelwood mechanism, which is commonly used to model surface reactions. This mechanism considers the adsorption of reactants on the surface of the catalyst, the formation of an intermediate complex, and the desorption of the product from the surface [10].

The rate of the reaction can be expressed as:

$$r = k \cdot \theta_A \cdot \theta_B \tag{1.1}$$

where r is the reaction rate, k is the rate constant, θ_A and θ_B are the fractional surface coverage of the reactants A and B, respectively. The Langmuir-Hinshelwood mechanism assumes that the rate-determining step is the reaction of the adsorbed intermediate complex.

In thermal catalysis, the reaction rate is also dependent on the temperature of the system, which can be described by the Arrhenius equation:

$$k = A \exp\left(-\frac{E_{\text{act}}}{k_{\text{B}}T}\right) \tag{1.2}$$

where k is the reaction rate constant, A is the pre-exponential factor, E_{act} is the activation energy, k_{B} is the Boltzmann constant, and T is the abso-

lute temperature. The activation energy, E_{act}, denotes the minimum energy needed for a reaction to occur, while the pre-exponential factor, A, signifies the theoretical rate at infinite temperature, also referred to as the frequency factor. By plotting the natural logarithm of the reaction rate against the reciprocal of the absolute temperature, the activation energy can be obtained from the slope of the resulting straight line, as depicted in Figure E.1 in the appendix. However, some reactions may display non-Arrhenius behavior, where the slope fluctuates with temperature.

CO oxidation reactions at low temperatures exemplify this, as the reaction rate is influenced not only by the activation energy but also by the reactant coverage on the catalyst surface. At lower temperatures, CO molecules tend to bind more firmly to the catalyst surface, causing a reduction in the reaction rate. Conversely, at higher temperatures, the activation energy prevails, and the reaction rate increases with temperature, adhering to the Arrhenius equation [10].

Understanding the kinetics of the catalytic reaction is important for designing and optimizing catalysts for industrial processes. By controlling the surface structure and composition of the catalyst, it becomes possible to fine-tune the reaction rate and selectivity to produce the desired outcome.

1.1.3 Nanoparticles

The surface properties of catalysts are essential, as reacting molecules bind to their surfaces. Increasing the surface area leads to a higher number of active sites available for reactions. Consequently, boosting the catalyst's activity can be achieved by enhancing the available surface area per volume of the catalyst material [4]. Furthermore, since many state-of-the-art catalysts comprise non-abundant elements, this approach also improves the economic feasibility of catalytic processes. This has led to the development towards smaller catalyst particles, as the surface area-to-volume ratio for a sphere with radius r scales accordingly:

$$\frac{\mathrm{A}}{\mathrm{V}} \propto \frac{1}{r}. \tag{1.3}$$

As a result, the smaller the particle, the more precious material like Pt or Au is at the surface and able to participate in catalytic processes. Nanoparticles, which range from 1-100 nm in size, have various shapes, so the ratio of surface atoms to volume does not strictly follow equation (1.3). For a catalytic material to have a significant global impact, it must be abundant, easily accessible, and cost-effective, enabling its use for terawatt-scale energy conversion [3].

The Wulff-construction model is a common method for modeling nanoparticle structure. This method scales the relative areas of different crystalline facets based on their surface energies to minimize the total surface energy of the nanoparticle. One intriguing aspect of catalytic nanoparticles is that

as the particle size reduces to less than tens of nanometers, the distribution of various undercoordinated sites increases due to the insufficient number of atoms forming low-energy facets. These diverse undercoordinated sites possess different binding energies, suggesting that particle size can influence catalytic properties. This phenomenon, known as the particle size effect, has been observed in nanoparticles for various reactions, such as CO oxidation on Au particles [14, 15]. When particle size is further reduced to below 1-2 nm, quantum mechanical effects may impact catalytic properties [16, 17]. Particles of these sizes are typically referred to as clusters. Notable size effects have been reported in this size regime, with significant differences in catalytic activity observed upon adding a single atom [18, 19]. Therefore, controlling nanoparticle and cluster size is vital for examining fundamental catalytic properties.

Chapter 2

Experimental method

This chapter will first describe the design of the µ-reactor and emphasis the strength of this. Secondly a detailed description of the experimental setup used together with activity measurements with a quadruple mass spectrometer and lastly a description of the UHV related techniques used to analyse and characterise the catalyst.

2.1 The µ-reactor

The µ-reactor chip developed at CINF was first reported in 2009 [9], with a comprehensive description of the device and its fabrication process available in [20]. The µ-reactor platform has been further developed at DTU by multiple PhD students from CINF/SurfCat and is detailed in [9, 21, 20, 22, 23, 24]. Briefly, the µ-reactor is made from a 4" silicon wafer and can hold up to 12 µ-reactors per wafer. The design features four holes: two inlets (I1 and I2) and two outlets (O1 and O2), as shown in Figure 2.1.

The Si-based µ-reactor, fabricated in a clean room, measures 27x16.1 mm and includes two inlets, a mixing zone, an outlet, a reactor volume, and a capillary for gas extraction from the reactor volume. The mixing and outlet channels have a depth of 250 µm, while the reactor and capillary have a depth of 3 µm. A 50 nm layer of SiO_2 is grown on the entire structure to serve as an inert substrate for the catalyst being tested.

The reactor volume, which measures 10 mm in radius and 3 µm in depth, giving a total volume of 240 nL is located at one end of the reactor. A meander like structured mixing channel extends between the two inlet holes and the reactor volume, ensuring homogeneous gas mixing by diffusion before entering the reactor volume. All reactants and products within the reactor volume are directed out of outlet O2, which connects to a quadrupole mass spectrometer (QMS) through a capillary. This capillary transitions the high-pressure gas flow into molecular flows under ultra-high vacuum (UHV) pressure conditions, allowing for accurate gas product analysis after the reaction.

To maintain a constant pressure during reactions, a pressure controller is connected to outlet O1. The channel leading to O1 connects with the channel from the two inlets in front of the reactor volume with a smaller tube leading the gas into the reactor volume to prevent back diffusion [9]. This

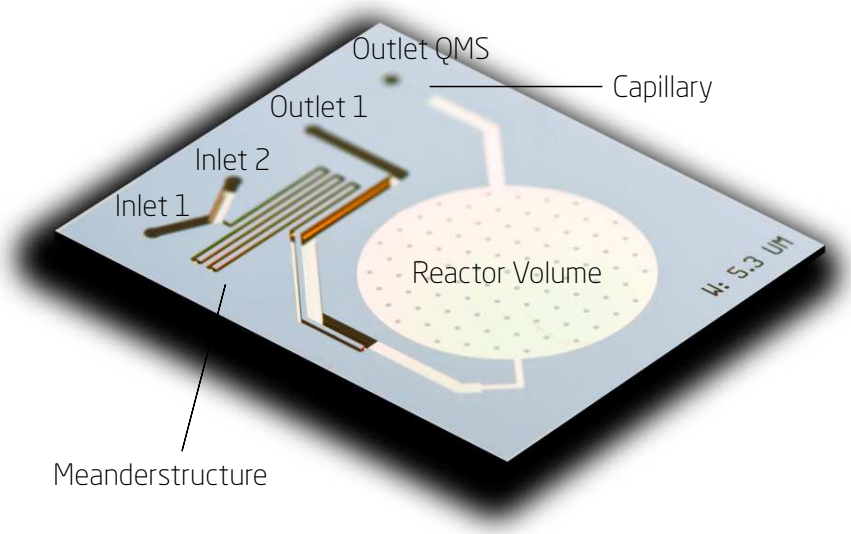

Figure 2.1: The design of the µ-reactor. Image taken by Thomas Pedersen [9]

design guarantees a constant ”buffer” of the gas mixture in front of the reactor volume and ensures that all gas entering the reactor volume is analyzed after leaving only through O2. The backside of the µ-reactor, seen in figure 2.2a, shows the placement of two heating elements and a four point probe resistance temperature detector (RTD) for measuring the temperature of the µ-reactor.

The unique design of the µ-reactor allows for highly sensitive measurements by leading every molecule that enters the reactor volume into the mass spectrometer, despite most of the incoming gas being pumped away immediately. This design offers several advantages over traditional catalytic reactors, such as a low thermal mass enabling rapid temperature changes, the capability to measure small amounts of catalyst, and the ability to safely handle explosive or dangerous mixtures. The glass lid also provides easy optical access to the catalyst, making it suitable for photo-catalysis. Additionally, the diffusion length of the reactants and product gases in the reactor volume ensures full contact with the catalyst. However, traditional surface science techniques cannot be applied to the catalyst due to the hermetically sealed reactor design. The maximum achievable temperature is theoretically limited by the lid’s melting point (approximately 700°C), much lower than that of traditional UHV setups.

The µ-reactor’s design, featuring a high area-to-volume ratio, facilitates the study of low catalyst loading required for mass-selected nanoparticles from the nanobeam cluster source. The capillary design allows experiments to

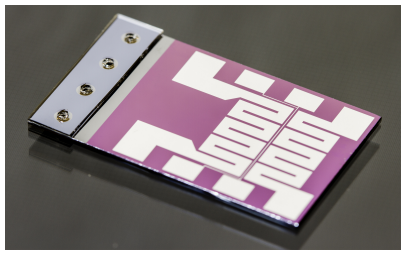

(a)

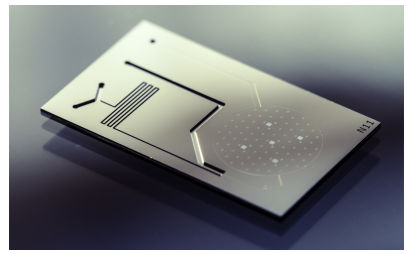

(b)

Figure 2.2: a) The design of the dual heater structure and 4 point probe resistance measurement for the RTD temperature detection. b) The design of the latest edition of the μ-reactor with 5 visible areas containing grids for identical location inspection. Image taken by Thomas Pedersen.

operate at high pressures while maintaining ultra-high vacuum (UHV) conditions on the backside, ensuring high sensitivity measurements of reaction products and by-products with a quadrupole mass spectrometer (QMS).

2.1.1 Introducing catalyst into the μ-reactor

The μ-reactor is not effective without a catalyst to measure. Two methods have been used to introduce a catalyst into the reactor: drop casting and physical vapor deposition.

In drop casting, a catalyst (e.g., CuZn on alumina) is milled and sieved with the smallest sieve available 50 μm before put in a solution of 18.2MΩ ultrapure water or 97% ethanol and sonicated. Ethanol solutions have the advantage of lower surface tension, allowing for smoother flow to the reactor chamber edges and more uniform catalyst distribution. However, if the catalyst is highly reactive at room temperature, carbon from ethanol may bind to it, forming carbides and reducing the catalyst's activity. A rule of thumb is to prepare a catalyst concentration of c = 1 g L^{-1} and drop a 40 μL droplet. Different catalyst activities may require varying amounts to avoid full conversion, which then becomes mass transport limited and hinder the study of the properties of the catalyst.

Thin film deposition is another method for introducing catalysts, used at SurfCat. This technique requires a vacuum, as it relies on a long mean free path of the molecules. A target material (e.g., Ti) is mounted in the sputter chamber, and ionized Ar gas is accelerated towards it to sputter off the metal. The metal then moves towards the sample and deposits uniformly over the reactor, creating a clean, homogeneous thin film. Introducing minute amount of oxygen in the vacuum chamber creates an oxide thin film which can be used to alter the support substrate of the nanoparticles in the μ-reactor (TiO_2).

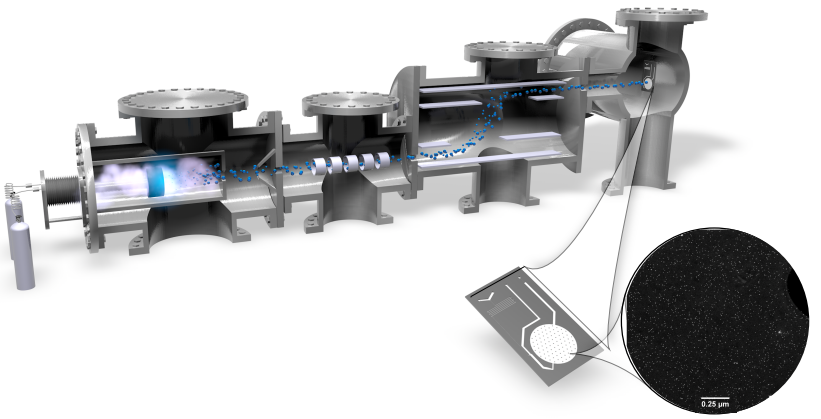

Figure 2.3: Utilizing magnetron sputtering, the Nanobeam cluster source sputter atoms off from a target, which then combine into clusters and nanoparticles. These are then directed into a lateral time-of-flight mass filter, which separates particles according to their mass to charge ratio. The system is tuned to a desired particles size, and the atoms are then deposited onto a µ-reactor. Image courtesy of Jakob Kibsgaard.

Mass selected nanoparticles

To study size effects on catalyst one has to make well defined nanoparticles. This is done by the Omicron cluster source team at SurfCat. The cluster source has been operated by master's student Jens Ringsholm and PhD students Niklas Secher, Karl Toudahl, Julius Needham, and Rikke Plougmann and post doc researcher Fransesco Presel for the deposition of particles on the µ-reactors.

Figure 2.3 presents a schematic illustrating the working principle of the cluster source.

The cluster source uses magnetron sputtering to sputter of material from a target. During this PhD work it has been either a pure Cu target, 50/50 AuTi target, pure Pt target or dual target Cu and Co for study on CuCo in-flight alloys.

During magnetron sputtering, a strong electric field accelerate ionized Ar^+ ions towards a target, causing material to be sputtered into the vacuum. The atoms and clusters subsequently engage in gas-phase aggregation, resulting in the formation of various-sized clusters ranging from single atoms to large nanoparticles [25, 26].

The gas-phase aggregation occurs in the aggregation zone, where the magnetron sputtering target is situated, as depicted in the left side in Figure 2.3.

Several particles exiting the aggregation zone carry an electric charge. The

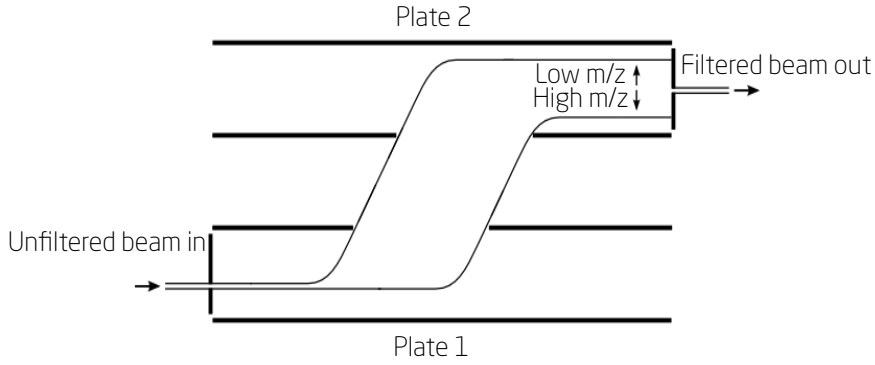

Figure 2.4: An illustration of a lateral time-of-flight mass filter in which an unfiltered particle beam enters the time-of-flight chamber. Upon applying an electrical pulse on plate 1 and plate 2 subsequently, the particles are displaced based on their mass-to-charge $\frac{m}{z}$ ratio. The the small exit slit allowing for a precise range of masses to pass through. Adapted from [28].

charged particles are focused and accelerated using electrostatic lenses and ion optic lenses. To achieve a narrow particle size distribution deposited on the μ-reactor the particles enter a lateral time-of-flight mass filter, where high-voltage pulses applied to two plates cause vertical acceleration based on their mass-to-charge ratio ($\frac{m}{z}$). Particles are then laterally displaced and filtered through a narrow exit aperture [27]. The working principle of the ToF can be seen in figure 2.4.

Most of the charged particles carry one elementary charge, which effectively results in a filtering based on the particle mass.

For more on the cluster source the reader is referred to former PhD students dissertations [28, 29, 30]

2.1.2 Anodic Bonding

To ensure the necessary sealing from the outside atmosphere for the silicon-based μ-reactors, a Pyrex lid is anodically bonded to the reactor's surface. Anodic bonding provides a hermetic seal, unlike o-rings which can allow gas leakage through the polymer compound. During the anodic bonding process, covalent bonds form between the sodium ions (Na^+) in the Pyrex lid and the oxide in the SiO_2 layer, resulting in an atomically thin seal. This process leaves a minimal height of approximately 3 microns, yielding a total reaction volume of 240 nL. Figure 2.5 illustrates the working principle of an anodic bonding process. The bonding takes place at temperatures around 450 °C, which unfortunately can cause most catalysts to sinter or change their morphology.

To address this issue, a specialized setup for bonding while cooling the sensitive active catalyst-containing area is employed, as shown in figure 2.6.

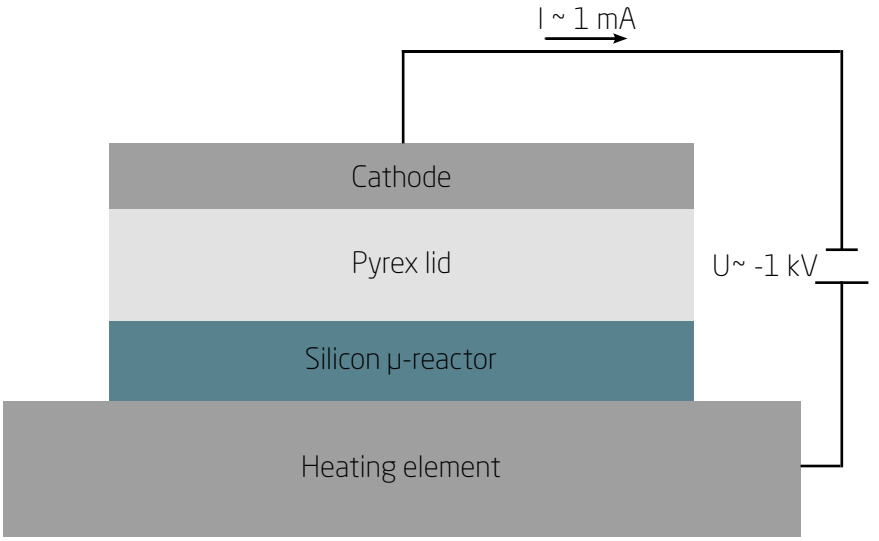

Figure 2.5: This schematics display the working principals of the anodic bonding setup.

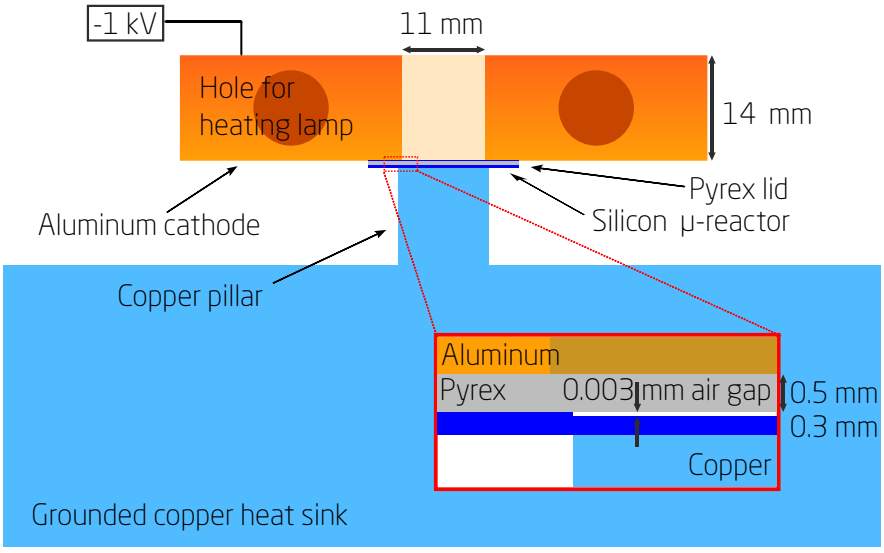

Figure 2.6: This figure displays the working principals of the cold anodic bonding setup. Adapted from [31].

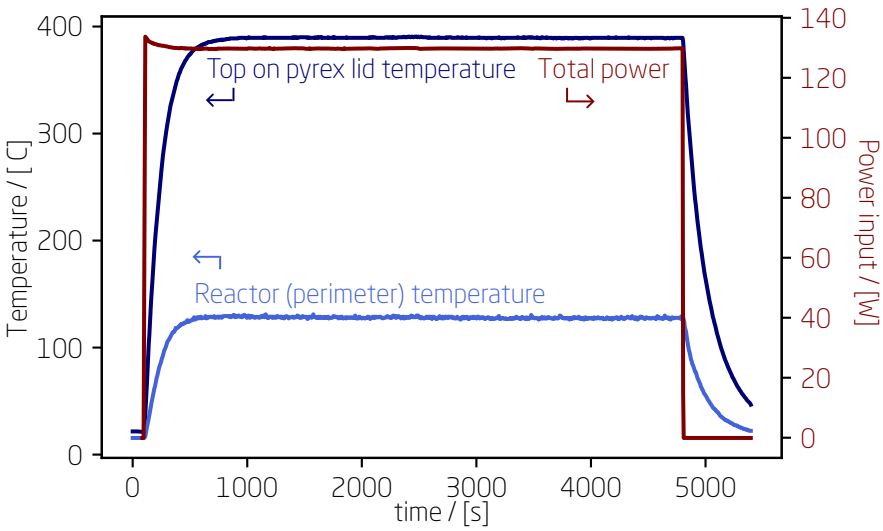

Figure 2.7: Monitoring the temperature on top of the reactor and beneath the reactor at the perimeter of the active area since the Cu-coldfinger is taking up the space directly under the sensitive reactor area containing the catalyst. This is the microreactor MR 65 loaded with 5% 160k amu, 3.5nm AuTi on TiO2. The cooling water was kept at 11 °C to avoid condensation on the outside of the equipment.

A copper block with an extruded finger is kept cold by 10 °C cooling water, and heat paste is applied on top of the cold finger to ensure a good thermal connection between the cooling block and the reactor's sensitive area. The reactor and Pyrex glass lid are then placed firmly on the cold finger. An aluminum heating block with an 11 mm diameter cylindrical hole is placed on top of the reactor, with the hole positioned over the heat-sensitive reactor area. The cathode is placed on top of the aluminum block to keep the entire structure in place during bonding. The aluminum block is heated to 350-450°C by two light bulbs. In figure 2.7, a plot of an anodic bonding process monitored by two thermocouples placed on top of the Pyrex lid and underneath the µ-reactor at the perimeter of the catalyst-deposited reactor area is shown.

The success rate of the anodic bonding process varies significantly and is highly dependent on the operator's expertise. Some operators may have a success rate as low as 50%, while experienced ones can maintain a rate of approximately 80%. Incomplete bonding is common, preventing the reactor from being hermetically sealed and causing gas leaks. This incomplete bonding is frequently attributed to particles or scratches in the µ-reactor that prevent close atomic contact between the pyrex lid and the SiO_2. Unsuccessful bonding can also be the result from issues like misplaced pyrex lids,

which occurs due to obstructed views from the heating block. To mitigate this issue multiple attempts has been tried and failed to manufacture a form in non-electrical conductive materials to guide and place the pyrex lid exactly on top of the µ-reactor. However, these attempts all increased the amount of incomplete bondings lowering the total success-rate.

Currently, new operators undergo training using empty reactors, as well as reactors with drop-casted catalysts and reactors with sputtered thin films. This training is essential before they handle reactors containing mass-selected nanoparticles from the cluster source.

2.2 Setup - microreactorNG

The µ-reactor is mounted in the various setups tailored to the specific type of µ-reactor. The photo-reactor setup is used for photocatalytic catalysis, the sniffer setup is used for electrochemical catalysis (EC-MS, electrochemical mass spectrometry) and the microreactorNG setup is used for thermal catalysis together with another older designed setup. In this section, a description of the microreactorNG setup will be provided. While this setup is the primary focus of the PhD research, some work has also been conducted using the other setups.

In figure 2.8 a schematic of the entire gas handling of the microreactorNG setup is displayed.

The microreactor is mounted in a steel interface block, as seen in Figures 2.9 and B.1. This block features eight (8) pogo pins that ensure electrical connections to the two heaters and the resistance temperature detector (RTD) on the µ-reactor's backside.

Viton O-rings are used to seal the µ-reactor's inlets and outlets to the interface block. A steel bar and two screws carefully press the µ-reactor onto the O-rings in the block, requiring cautious manual tightening to avoid breaking the Pyrex glass on the µ-reactor.

The mounting block is positioned within a containment chamber that can be evacuated or filled with Ar gas to control the atmosphere around the O-rings. This ensures that any gas leaking through the O-rings is either inert gas leaking in to the µ-reactor or gas directed out into the containment chamber, preventing unrelated gas from entering the µ-reactor and subsequently the mass spectrometer, which would lead to inaccurate measurements of gas molecules unrelated to the chemical reaction.

The older design setups lack a containment chamber around the interface block to control the atmosphere surrounding the O-rings. Instead, these setups utilize argon as an inert gas to flush the O-rings, making sure that only inert gas leaks into the QMS.

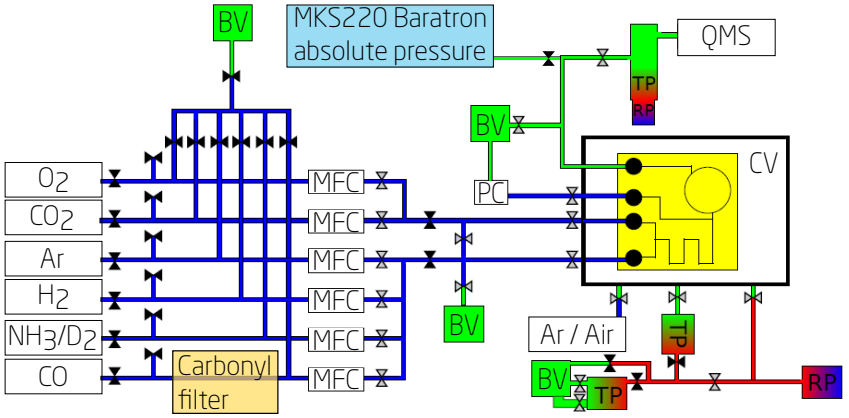

Figure 2.8: The schematic of the gas handling system at the microreactorNG setup includes various components. Black valves represent manual needle valves, while gray valves denote automatic pneumatic pressure valves. MFCs are MKS mass flow controllers, ranging from 1 ml/min (CO line) to 10 ml/min (CO_2 and O_2 lines). The Buffer Volume (BV) is utilized to release large volumes of gas at high pressures, expanding the gas and reducing the pressure by orders of magnitude (below 1 mbar range). TP and RP stand for the different turbo pumps and roughing pumps, respectively. PC is a Bronkhorst pressure controller with a capacity of up to 2.5 bar. A Cu catalyst-based carbonyl filter is installed on the 6th gas flow line to eliminate any carbonyls from the CO gas stream before entering the microreactor system. An MKS220 Baratron absolute pressure transducer is placed after the capillary outlet and before the QMS to measure flow rates of various µ-reactors and calibrate the mass spectrometer. The containment volume (CV) is employed to address issues with leaking Viton O-rings, functioning either as an evacuated chamber or with approximately 15 mbar Ar gas.

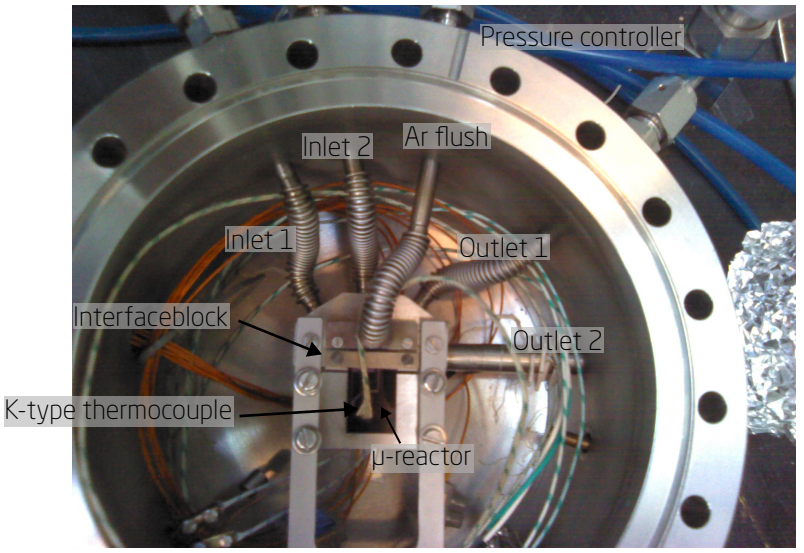

Figure 2.9: Image of a mounted µ-reactor in the microreactorNG setup. The containment volume is encapsulated within the visible stainless steel wall.

Table 2.1: PID settings for TC and RTD controlled heating

	P	I	D
RTD	0.5	0.2	0
TC	0.1	0.01	0

2.2.1 Heating and temperature control

The heating of the µ-reactor is controlled by a Raspberry Pi, which receives temperature readings from either the Resistance Temperature Detector (RTD) or K-type thermocouple (TC), as well as user-defined set points. A PID (Proportional-Integral-Derivative) algorithm calculates the required power supply to achieve the desired temperature. The RTD is located on the back-side of the µ-reactor, while the K-type thermocouple is positioned on the Pyrex glass lid for enhanced reliability and safety.

Tuning strategy of the PID

After an SD-card malfunction, the PID settings were lost and needed to be experimentally re-established. This involved conducting various temperature ramps while adjusting the Proportional and Integration terms, with the Derivative term set to zero, to achieve optimal temperature control.

Two sets of PID settings were identified for stable temperature control. The first set used the RTD as the feedback temperature for the PID controller, while the second set relied on the TC for temperature control. See table 2.1.

The RTD is much faster at detecting temperature changes compared to the

TC, which is slower due to the low thermal conductivity of the Pyrex glass lid. Consequently, using the RTD-based PID settings with the TC would result in significant overshoot and temperature oscillation. Therefore, the two sets of PID settings were determined to ensure stable temperature control for both input temperature sources.

Heating

The μ-reactor is heated by two resistance heating elements, Heater 1 and Heater 2, situated on the backside of the reactor beneath the reactor volume. These heating elements are fabricated in the same process as the Resistance Temperature Detector (RTD), consisting of a 10 nm TiO_2 adhesive layer and 100 nm of platinum on top. The two heating elements are independently controlled using a CPX400DP PowerFlex Dual DC Power Supply, which typically operates in the range of 0.1 A - 0.4 A and 5 V - 40 V, providing up to around 16 W of power to heat the μ-reactor to approximately 350°C.

To ensure even heating across the entire reactor volume, a brief study was conducted using a thermal camera and various power settings. The test examined multiple power ratios, from power supplier 1 being 2.5 times higher than power supplier 2, to the opposite ratio of 1:2.5. The temperature was adjusted from 30°C to 300°C for each power ratio setting. The images were analyzed using ImageJ processing software to estimate the settings that yielded the most uniform heating across the reactor volume [32]. The optimal setting was found to be a 2:1 ratio, with the heating element closest to the outlet and inlet holes receiving the most power, as shown in Figure 2.10. Although the most uniform heating was observed at a ratio of 1.8 to 1 at higher temperatures, the settings were fixed at 2 to 1 for all temperatures due to the acceptable loss in uniformity compared to the additional programming needed and the increased risk of software failure in the temperature program that follows.

Resistance Temperature Detector

An RTD (Resistance Temperature Detector) works on the principle of the temperature-dependent change in electrical resistance of certain metals, such as platinum. As the temperature increases, the resistance of the metal increases as well. This change in resistance can be measured and converted to a temperature using the known temperature coefficient of resistance for the metal. Platinum was chosen as the material for the RTD due to its resistance changing approximately linearly within the temperature range of interest (50 - 350°C) following

$$R_T = R_0(1 + \alpha T) \tag{2.1}$$

with a table value for alpha of 3.927 x 10^{-3} [33].

At the beginning of every experiment the RTD on the μ-reactor is calibrated

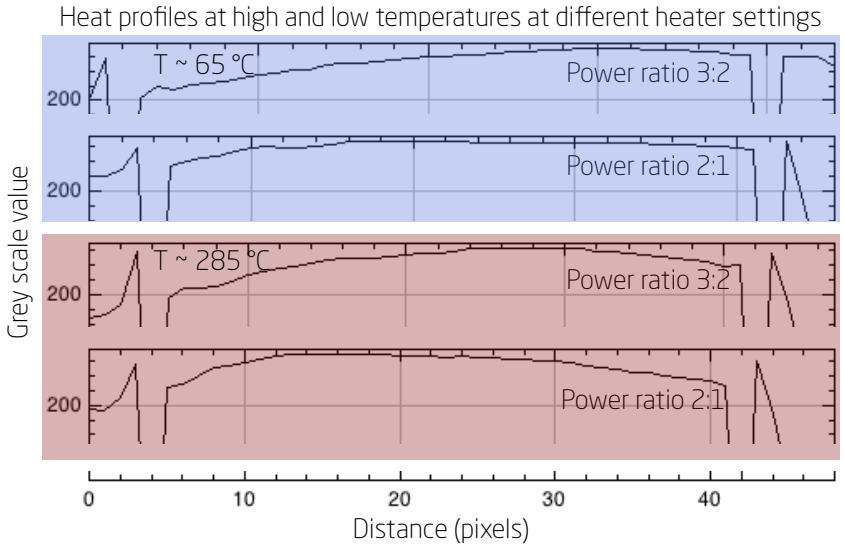

Figure 2.10: 4 heating profiles of a µ-reactor obtained with a FLIR E50 camera and analysed with ImageJ at various temperatures and power ratio settings for heater 1 and heater 2. Top two profiles in blue are done at low temperatures 65 °C and the two bottom profiles are done at high temperatures 285 °C. A power ratio of 2 to 1 (providing the most power to heater 1 closest to the mounting block) yields the most uniform heating of the µ-reactor up until the higher temperature regime.

using the Callendar-Van Dusen equation

$$R_T = R_0 \left(1 + AT + BT^2 + C(T - 100)T^3\right) \tag{2.2}$$

with

$$A = 3.985x10^{-3} \tag{2.3}$$
$$B = -5.85x10^{-7} \tag{2.4}$$
$$C = 0 \tag{2.5}$$

because the temperature is above 0°C [33].

To calibrate the RTD, its actual resistance is measured using a 4-point probe resistance measurement with an Agilent 34410A. This measurement is then compared to the actual temperature measured with a K-type thermocouple. The calibration resistance and temperature are used in equation 2.2, which includes table lookup values for constants A and B. This determines the resistance at T = 0°C, denoted as R_0. This value is used to calculate the temperature at any given resistance during a catalytic activity experiment performed with the µ-reactor.

The annealing process for the RTD on the µ-reactors was improved by post-doc employee Hoà Lê Thanh, who developed a 24-hour procedure that made the platinum more resilient to high temperatures and prolonged experiments.

2.2.2 Gas flow in µ-reactor capillary

Catalytic reactions in industry often occur at high pressures. The reaction rate and selectivity can be influenced greatly by the pressure of the reactants. However, studying these reactions can be challenging as many analytical techniques require a highly controlled vacuum environment. To regulate the gas flow from the reactor volume, which can reach up to 3 bar in the µ-reactor, into the UHV chamber, a narrow capillary is placed in between. Understanding the gas flow through the capillary is important, as it can lead to noticeable artefacts in the total gas flow due to the properties of the capillary and the gases flowing through it.

The flow through the capillary effectively determines the Gas Hourly Space Velocity (GHSV). The µ-reactor has proven to be a valuable tool for investigating catalysis, and it can help bridging the pressure gap with its well-designed capillary [34]. The capillary, located at the end of the channel just before outlet O2, is designed to manage the gas flow and decreases the pressure so the amount of products can be analyzed in the quadropole mass spectrometer (QMS) in a UHV chamber.

Through the capillary the pressure transition from the bulk flow regime to the molecular flow regime reducing the pressure by 10 orders of magnitude,

from 1 bar to 1e^{-7}mbar. The fabrication dimensions of the capillary in the µ-reactor is

$$\begin{aligned} w_{cap} &= 5 \cdot 10^{-6}\,\text{m} \\ h_{cap} &= 3 \cdot 10^{-6}\,\text{m} \\ l_{cap} &= 1.5 \cdot 10^{-3}\,\text{m} \end{aligned} \tag{2.6}$$

with unknown uncertainties.

The equation for the molecular flux has been extensively investigated and described in [9, 21, 20, 22, 34] and elaborated further more in [35]. The following representation of the equation originates from [35]:

$$\dot{N}_{cap} = \frac{1}{k_B T}\frac{1}{l_{cap}}\left[\left(\frac{\pi}{8\eta}a^4\bar{p} + \frac{2\pi}{3}a^3\bar{v}\frac{1+2\frac{2\sqrt{2}}{\sqrt{\pi}}\frac{a}{\eta}\frac{\bar{p}}{\bar{v}}}{1+2.48\frac{2\sqrt{2}}{\sqrt{\pi}}\frac{a}{\eta}\frac{\bar{p}}{\bar{v}}}\right)(p_1 - p_{tran}) + \frac{2\pi}{3}a^3\bar{v}(p_{tran} - p_2)\right] \tag{2.7}$$

This mathematical expression demonstrates that the changes in molecular flux through the capillary are inversely proportional to the absolute temperature, indicating the importance of accounting for temperature-dependent artefacts.

$$\dot{N}_{cap} \propto \frac{1}{T}p_1 \tag{2.8}$$

In thermal catalysis studies in the µ-reactor, where catalytic activity is measured over a temperature range of 300 to 650 Kelvin, the molecular flux decreases by a factor of two. It is important to be aware of this temperature-dependent flux when studying a reaction, as a decrease in signal could result from either deactivation and sintering effects or an inherent behavior of the capillary.

The equation 2.7 is complex and dependent on multiple parameters, including temperature, pressure, and dynamic viscosity of the gas composition, which can be controlled to some degree during experiments. It is crucial to recognize that these parameters directly impact the gas flow, with temperature and pressure playing a particularly significant role as well as the design parameters of the capillary. For instance, increasing the pressure in the reactor leads to an increase in flow, while heating the reactor decreases the gas flow. Such changes are significant because experiments typically involve varying temperatures and therefore varying gas flow, which, in turn, impacts the molecular residence time in the reactor and the reactant conversion factor.

Through the capillary, the flow changes from a bulk laminar viscous flow, mostly dominated by collisions between molecules, to a molecular flow,

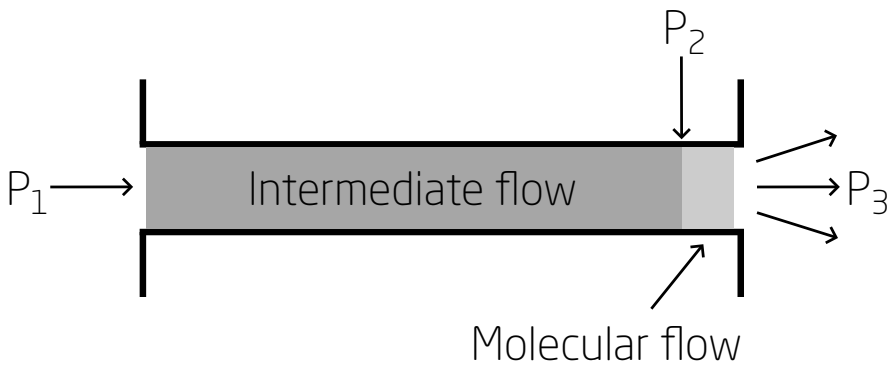

Figure 2.11: Visual figure to explained the flow through the capillary of the µ-reactor. Adapted and updated from [9].

mostly dominated by collisions between the molecules and the wall. A schematic of the capillary, adapted from [20], can be seen in Figure 2.11.

The figure provides a visual representation of the gas flow, which begins with pressure p_1, equivalent to the pressure in the reactor chamber, typically ranging from 1 to 3 bar. At the opposite end, the pressure is labeled p_3 and corresponds to the pressure in the main chamber connected to the mass spectrometer. The pressure in the main chamber is on the order of 10^{-7} to 10^{-10} mbar, allowing us to consider p_3 effectively zero compared to p_1. The intermediate pressure, denoted p_2, marks the point where the gas flow transitions from viscous to molecular flow.

The nature of gas flow through a cylindrical tube with a cross-sectional diameter of d can be understood through two different dimensionless numbers, namely, the Knudsen number Kn and the Reynolds number Re, which are defined as follows [36]:

$$\mathrm{Kn} = \frac{\lambda}{\mathrm{d}} \tag{2.9}$$

$$\mathrm{Re} = \frac{\rho \nu d}{\eta} \tag{2.10}$$

Here, λ is the mean free path of the molecules, and d is the cross-sectional diameter of the tube. The last three parameters, ρ, ν, and η, are the density, velocity, and viscosity of the gas, respectively. The flow can be in one of three different states. The first state is the bulk or viscous state, which applies to gases with Kn < 0.01 [20, 37]. In the viscous regime, gas flow can be either turbulent or laminar, determined by the Reynolds number (Re). If Re exceeds 2200, the flow is fully turbulent, while Re below 1200 results in entirely laminar flow, with gases mixing solely by diffusion. When the

Reynolds number falls between these values, the flow can be either turbulent or laminar, depending on the tube's geometry and surface roughness. The second state is the intermediate state, with a Knudsen number (Kn) between 0.01 and 1. The third state is the molecular state, where the gas has a Kn above 1, meaning that molecules, on average, collide with the wall before encountering each other [34, 37].

The mean free path of molecules is given by

$$\lambda = \frac{\mathsf{k_B T}}{\sqrt{2}\pi d_0^2 \mathsf{P}} \tag{2.11}$$

where k_B, T, d_0, and P denotes Boltzmann's constant, absolute temperature of the molecule, the diameter of the molecule (10^{-8} m), and pressure, respectively. We can use this to calculate at which pressure the gas flow goes from laminar and viscous flow through intermediate further down to a molecular flow.

The expected flux of molecules into the main chamber with the QMS can be calculated with Equation (2.7) using the dimensions of the µ-reactor in (2.6) and choosing a gas like Ar at 1 bar at one end of the capillary [1]. Ar has a dynamic viscosity at room temperature $T = 298.15$ K of $\eta_{Ar} = 2.27 \cdot 10^{-5}$ Pa·s . This gives a flux of molecules out of the capillary of

$$\dot{n} = 7.2 \cdot 10^{-10} \frac{\mathsf{mol}}{\mathsf{s}}$$
$$\dot{N} = 4.34 \cdot 10^{14} \frac{\mathsf{molecules}}{\mathsf{s}}.$$

The turbo pump attached the main chamber with the QMS has a pumping speed of $S = 68$ L/s.

The base pressure expected in the mass spectrometer P_{ms} can then be calculated

$$P_{ms} = \frac{k_B T}{S} \dot{N}$$
$$P_{ms} \approx 3 \cdot 10^{-7} \mathsf{mbar}$$

This is in good agreement with the ion gauge measuring the pressure in the main chamber.

Validation of the capillary equation

The calculated molar flow rates using the default expected design parameters of the capillary is summarised in table 2.2.

[1] Preferably the reactor volume and not the main chamber.

Table 2.2: Calculated flow rates through the capillary at outlet O2 on the μ-reactor at room temperature. With a reactor volume of 240nL this yields 12s for the entire gas volume to be exchanged.

Gas	η [Pa· s]	$\dot{n}_{\text{calc}}$ [nmol/s]
CO	1.74e-5	0.909
O_2	2.07e-5	0.798
CO_2	1.50e-5	0.987
Ar	2.27e-5	0.720
H_2	0.88e-5	2.20

To validate experimentally these numbers the molar flow rate through the capillary in the μ-reactors are measured using a calibration measurement involving the Baratron attached on the backside. The pressure rate is measured when the μ-reactor molar flow rate $\dot{n}$ is collected in an unknown, evacuated volume V_0 (the pressure rate is $\dot{p}_1$) and with a known evacuated volume V_{ref} (pressure rate $\dot{p}_2$) added.

Using the ideal gas law, we get

$$\dot{p}_1 V_0 = \dot{n} R T \tag{2.12}$$

$$\dot{p}_2 (V_0 + V_{ref}) = \dot{n} R T \tag{2.13}$$

$$\tag{2.14}$$

By eliminating the unknown volume V_0, we obtain the experimental molar flow rate

$$\dot{n}_{exp} = \frac{V_{ref}}{RT} \cdot \frac{\dot{p}_1 \dot{p}_2}{\dot{p}_1 - \dot{p}_2} \tag{2.15}$$

The reference volume V_{ref} is 26 mL. Using the fitted paramaters $\dot{p}_1 = 0.00081$ mbar/s and $\dot{p}_2 = 0.00046$ mbar/s seen in Figure 2.12 the unknown volume V_0 can be calculated to ≈ 34 mL.

The measured flux of five different gases (H2, CO, O2, Ar, and CO2) can be compared to the calculated flux, as shown in Table 2.3. The ratio of the calculated flux to the measured flux through the capillary is approximately 1.3 for all gases. This provides high confidence in the capillary equation, and the difference between the calculated and measured fluxes is likely due to the geometric assumptions of the fabricated microreactor.

A geometric correction factor can be determined for each of the five gases (H2, CO, O2, Ar, CO2) using the capillary equation. This correction factor is incorporated into the length of the capillary, denoted as the effective capillary length $l_{cap}^{effective}$. Although the geometric difference between the design parameters and the actual fabricated chips is more likely to be found in the uncertainty of the height, the length is easier to manipulate in the equation, so all geometric changes are placed in this term. The estimated

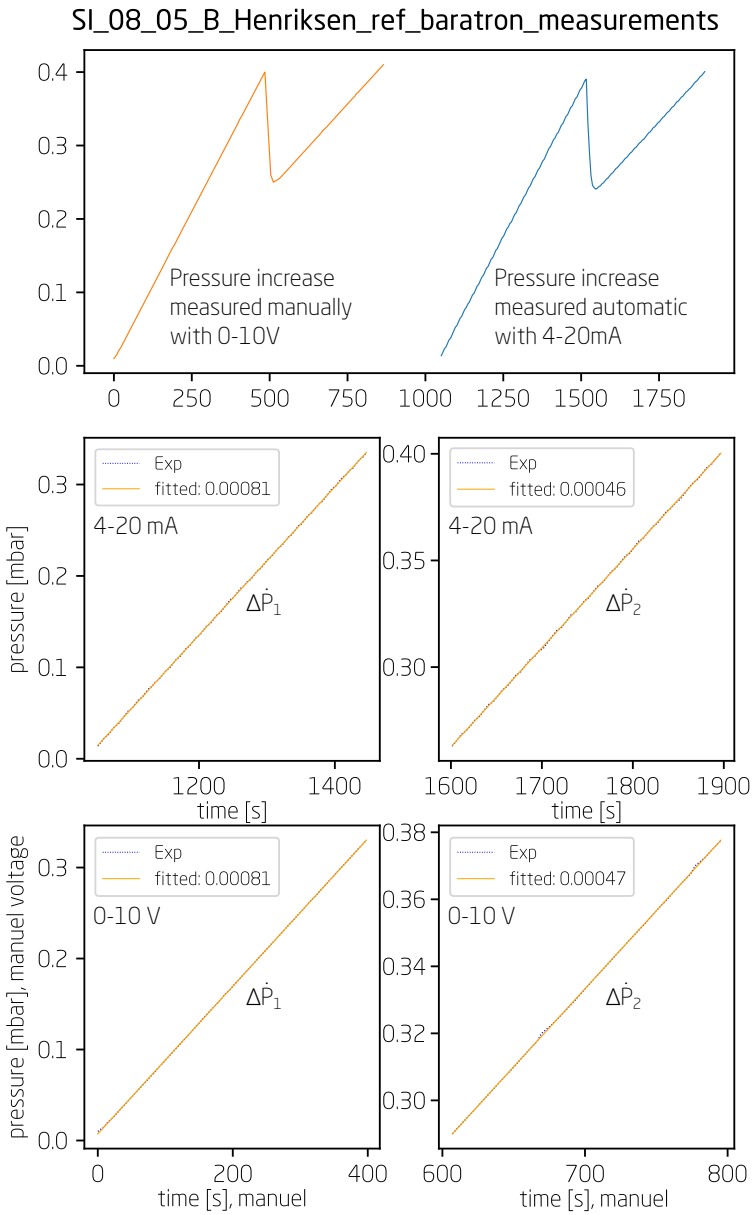

Figure 2.12: Baratron calibration measurements. The old chip from [9] is mounted on the setup and the pressure increase on the backside through the capillary with 1 bar of gas is measured with two methods. The Baratron has a manual 0-10 V output for which I measured manually to keep in count if the automatic programming I have made was measuring correct using 4-20mA output and controlled with a raspberry pi.

Table 2.3: Calculated and measured flow rates through the capillary at outlet O2 on the µ-reactor.

Gas	Calculated flux $\dot{n}$ [mol/s]	Measured $\dot{n}$ [mol/s]	Ratio [a.u.]
CO	9.09e-10	6.97e-10	1.31
O2	7.98e-10	6.21e-10	1.28
CO2	9.87e-10	7.59e-10	1.30
Ar	7.20e-10	5.65e-10	1.27
H2	2.20e-09	1.72e-09	1.28

Table 2.4: Default capillary length compared to the effective capillary length calculated from flow rates through the capillary at outlet O2 on the µ-reactor at room temperature given in table 2.3 With a reactor volume of 240nL this yields 12s for the entire gas volume to be exchanged. This yields a GHSV n the order of 300.

$l_{cap}^{default}$ [mm]	$l_{cap}^{effective}$ [mm]	Ratio $\frac{l_{cap}^{default}}{l_{cap}^{effective}}$ [a.u.]
1.50	1.94	0.771
1.50	1.91	0.784
1.50	1.94	0.774
1.50	1.90	0.790
1.50	1.91	0.784

effective capillary lengths for each gas are calculated and displayed in Table 2.3. The default capillary length (based on the designed parameters) is approximately 80

By updating the capillary length to an average of the effective capillary lengths of each gas, which is 1.92 mm, the calculated flux from the updated capillary lengths and the measured flux are remarkably consistent, with deviations of no more than 3%. This can be seen in Figure 2.13, where the red lines represent the difference between the calculated and measured flux.

2.2.3 The Quadrupole Mass Spectrometer

The quadrupole mass spectrometer (QMS) is the primary technique employed in this setup to analyze all products exiting the µ-reactor and entering the main chamber through the capillary. The QMS functions as a mass filter that allows only a single mass-to-charge (m/z) ratio to be detected [38]. This is achieved by ionizing the molecules using a hot filament (tungsten is used in this work) and then guiding them between four parallel rods, which are electrically connected in pairs, as illustrated in Figure 2.14b.

The pair of rods connected to a positive DC potential stabilizes the trajectory of molecules, while the RF potential destabilizes the trajectory of molecules with a low m/z ratio [38]. Conversely, the pair of rods connected to a negative DC potential constantly attracts the molecules, and the RF potential

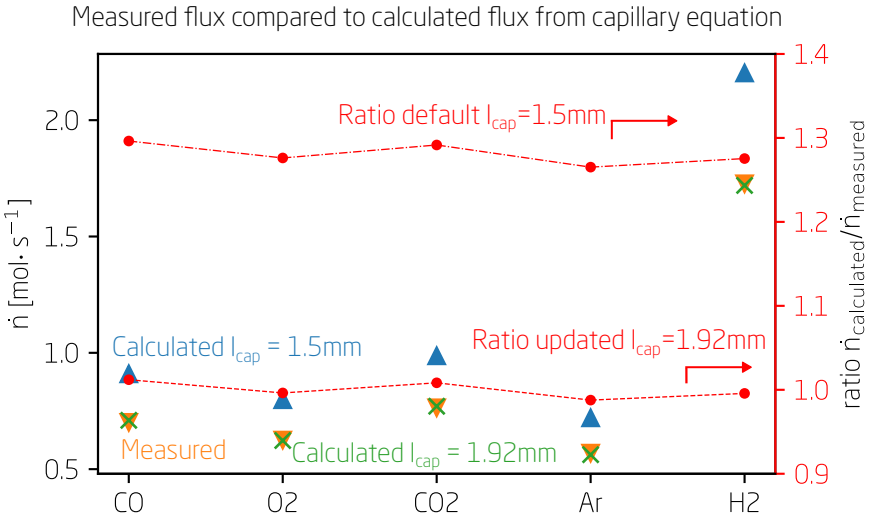

Figure 2.13: Graphical represntation of table 2.3. The measured flux through the capillary is orange downwards triangles. The Calculated flux throught the capillary at the default capillary length of 1.5mm is represented by blue upwards triangles and the calculated flux from the updated capillary length effectively at 1.92 mm is the green crosses. Left y axis is the flux in mol/s and right y-axis is the ratio between calculated and measured flux.

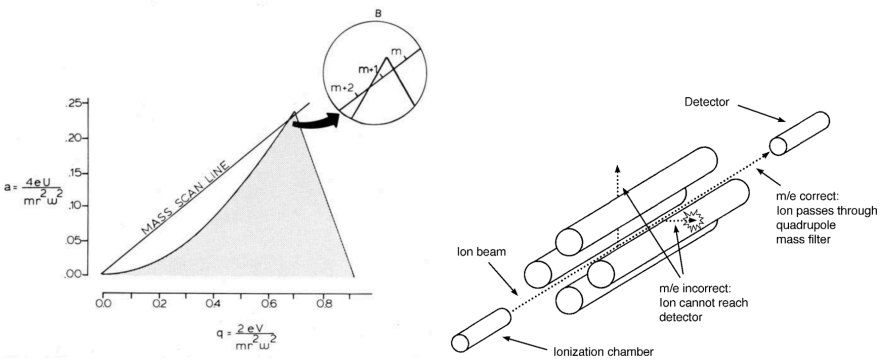

(a) Mass scan line. Adapted from [38]. (b) QMS four rods. Adapted from [39].

Figure 2.14: The grey area on the left figure represents a stable trajectory, and the mass scan line shows the different masses that will be detected. Only masses on the line that falls within the grey area will have a stable trajectory and be detected. The right figure display the four rods in a QMS generating the electrical field.

stabilizes the trajectory of molecules with a low m/z ratio but diverts heavier molecules into an unstable trajectory. By adjusting the DC potential and the frequency or magnitude of the RF potential, the QMS can sweep across different masses and distinguish masses separated by as little as $m/z = 1$ [38].

The most common method of operating the QMS involves maintaining a constant ratio between the DC and AC potentials, as demonstrated in Figure 2.14a, adapted from [38]. The two parameters governing the trajectory of molecules through an ideal simple quadrupole with a hyperbolic cross-section are a and q [38]. The y-axis parameter a is equal to $4eU/(mr^2\omega^2)$, while the x-axis parameter q is equal to $2eV/(mr^2\omega^2)$, where U and V represent the DC and RF potentials, respectively, ω denotes the frequency of the applied RF potential, r is the distance from the center of the z-axis to any of the four rods, and m is the mass of the ions [38]. By adjusting the ratio between the DC potential, U, and the RF potential, V, resolutions of 1 part in 1500 can be achieved [38]. Only masses on the mass scan line within the grey area will have a stable trajectory through the QMS and be detected.

The detector used in this setup is a Secondary Electron Multiplier (SEM), which consists of multiple charged metal plates that induce electron emission [38].

Figure 2.15 displays a typical mass spectrum of methane (CH_4) obtained from the online database webbook.nist.gov. The cracking pattern reveals that the intensity of mass m/z = 15 is almost as high as the mass of methane

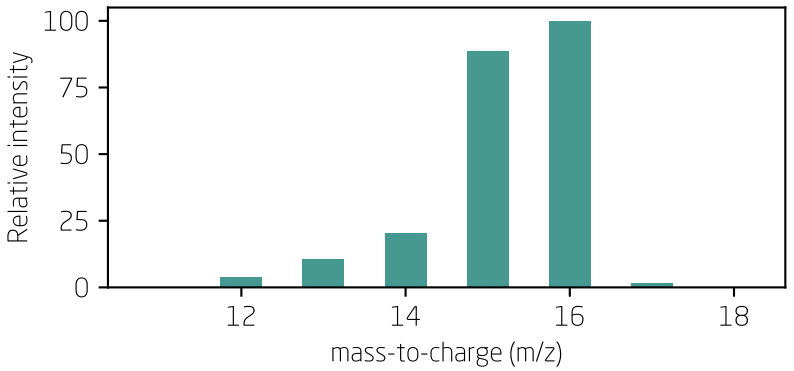

Figure 2.15: Mass spectrum of methane CH_4 with data from [40].

m/z = 16. This is because the less tightly bound hydrogen is lost, along with some mass, during the ionisation of the molecule [38]. Mass 14, 13, and 12 are less likely to be measured since the second and third hydrogen atoms are more strongly bound. By understanding the cracking pattern of the molecule being measured, the different molecules can be identified. For instance, in the case of methane, the mass of oxygen (m/z = 16) is the same as methane's, so methane can be measured at the second-largest intensity, m/z = 15, to avoid confusion regarding the measured mass. However, this approach is not suitable for all molecules. An example is N_2 or CO, both having their primary mass signal at m/z = 28 and almost no cracking patteren at $m/z = 14$ or $m/z =$ [12, 16] respectively [38].

2.3 Measuring activity in the µ-reactor-setup

This section will describe how to quantify the raw signals in the mass spectrum to number of molecules per second entering the mass spectrometer to quantify the products from the catalytic reaction of interest. The work presented in this section was inspired by the previous PhD student, Søren Scott [41], with whom I shared a passion for µ-reactor technology. He used QMS mass spectrum calibration with the sniffer EC-MS chip at DTU and we explored the possibility of applying the concepts of absolute quantification of QMS mass spectrum signals using electrochemistry to the heterogeneous thermal catalysis µ-reactor setup. There will be four concepts to be familiarised with.

Internal calibration is a calibration where the exact amount of molecules entering the mass spec is known or measured. This can be done from measuring the current of an electrochemical reaction with 100% Faradaic efficiency or with a MKS200d Baratron integrating the pressure increase in a known volume V_0 over time.

External calibration is the term used when the dimensions of the capillary is

known and used to calculate the flux of molecules entering the QMS.

Chip calibration relates to calibrating the dimensions of the capillary on the µ-reactor. This is needed as the fabrication varies and with that the dimensions of the capillary as explained in 2.2.2.

Predictive calibration is used when the molecule of interest is not available to be measured directly by internal or external calibration. This is done by calculating a relative sensitivity factor, denoted f, based of the physical property of the molecules ionization cross-section and relate this relative sensitivity factor to as many experimentally measured sensitivity factors from known internal and external calibrated molecules.

Absolute Quantification - Turn-Over-Frequency (TOF)

The ultimate goal in (thermal) heterogeneous catalysis is to determine the Turn-Over-Frequency (TOF), a direct measure of the catalyst's intrinsic ability to convert reactants into desired products. Quantifying mass spectrometer signals involves relating the signal (measured in Ampere) to the molecular flux (measured in molecules/s) entering the main chamber, as detected by the QMS.

The flux of known gases through a capillary in the µ-reactor was experimentally determined to be around 1 nmol/s or approximately 10^{15} molecules/s in a previous study [9]. However, due to fabrication uncertainties, capillary dimensions may vary, leading to different gas hourly space velocities for each reactor (see section 2.2.2).

To address this issue, an inert carrier gas, such as helium or argon, is used. The mass spectrometer signal for different analytes can then be normalized to the inert gas. This also accounts for the temperature-dependent flux decrease through the capillary, which could lead to rising signals in catalytic products even as absolute signals in the QMS decrease.

Although this method enables easy comparison of catalyst performance measured in different µ-reactors, it prevents comparisons with literature values, as absolute numbers are lost during normalization, and no real TOF can be calculated.

As a result, an alternative method was developed that employed electrochemistry to accurately account for the number of molecules, providing an exact flux through the capillary of an EC-MS chip [41, 42].

Relating the mass spectrometer signal to a flux of molecules is an ideal use case for capillaries from the microreactor platform, such as the thermal µ-reactor, the EC-MS chip, or the optical microreactor at SurfCat. This is because all the gas entering the reaction volume exits the µ-reactor through the capillary and is detected by the QMS.

The sensitivity of different molecules is assumed to be linearly related to the signal in the QMS, providing a sensitivity factor to correlate the signal with

a flux of molecules. This can be written as

$$S_{\mathsf{M}} = \mathsf{F}^{i}_{\mathsf{M}} \dot{n}^{i} \tag{2.16}$$

where S_{M} represents the QMS signal for a given mass M, $\mathsf{F}^{i}_{\mathsf{M}}$ denotes the sensitivity factor of a specific molecule i measured in the QMS at the mass-to-charge ratio M, and $\dot{n}^{i}$ signifies the molecular flux of that molecule exiting the capillary in the µ-reactor and entering the main chamber where the QMS is installed.

Electrochemistry can be utilized to precisely count the molecules that exit the EC-MS chip reactor, pass through the capillary, and are detected by the QMS, which records a signal proportional to the number of molecules. A comprehensive explanation of electrochemical calibration and subsequent quantification can be found in Søren Scott's thesis [41]. This electrochemical calibration is referred to as an *internal calibration*. By employing this *internal calibration*, the capillary of the EC-MS sniffer chip can be calibrated, resulting in what is termed a *chip calibration*.

In the work presented in this thesis, we mounted the *chip calibrated* EC-MS chip onto the µ-reactor setup to calibrate the QMS connected to the microreactorNG setup. This was achieved by directly measuring air through the EC-MS chip, as illustrated in figures 2.16 and 2.17, which display a mass scan and a mass-time measurement, respectively.

The flux through the capillary of the *chip calibrated* EC-MS chip was measured as follows

$$\begin{aligned} \dot{n}^{O_2} &= 1.17\,\mathsf{nmol/s} \\ \dot{n}^{air} &= 5.6\,\mathsf{nmol/s}. \end{aligned} \tag{2.17}$$

However, this step only provides sensitivity factors for molecules predominantly found in air, such as nitrogen, oxygen, and argon in the mass spectrometer. Using the flux $\dot{n}$ for oxygen in Eq. (2.17), we can estimate the sensitivity factor for the mass spectrometer on the microreactorNG setup for oxygen to be

$$\mathsf{F}^{O_2}_{32} = 12.5\,\mathsf{C/mol}. \tag{2.18}$$

This can also be observed in Figure 2.18, which displays a relationship between the relative sensitivity factor f derived from theoretical values of the molecules ionisation cross section at 70 eV on the x-axis and the measured sensitivity factor F for the setup-specific QMS. In Figure 2.19, the calibrated signals from air are shown.

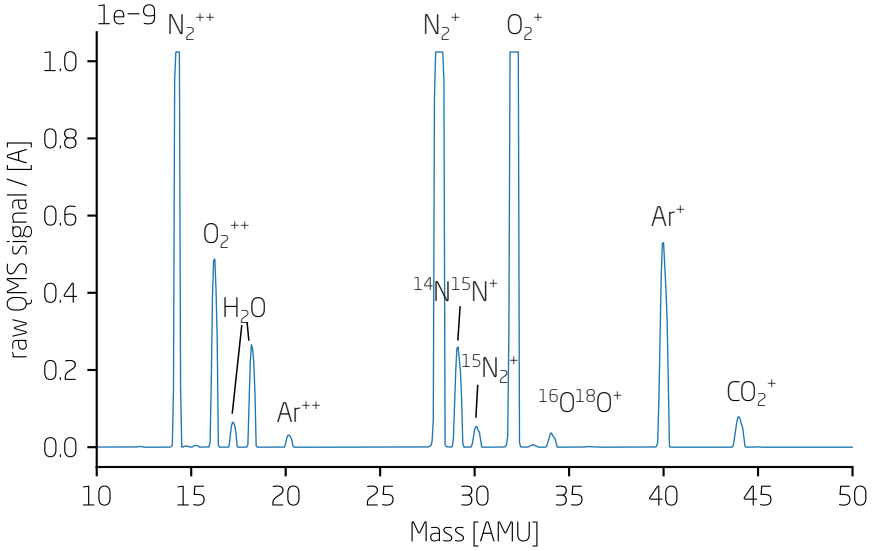

Figure 2.16: The mass spectrum of air measured in the QMS 400A, which is attached to the microreactorNG setup, was obtained through a calibrated sniffer chip. All peaks are labeled in the spectrum. Nitrogen and oxygen show the same magnitude because the cut-off signal was set to $1e^{-9}$ A to increase the sensitivity, enabling the measurement of masses with minute amount in air within the QMS.

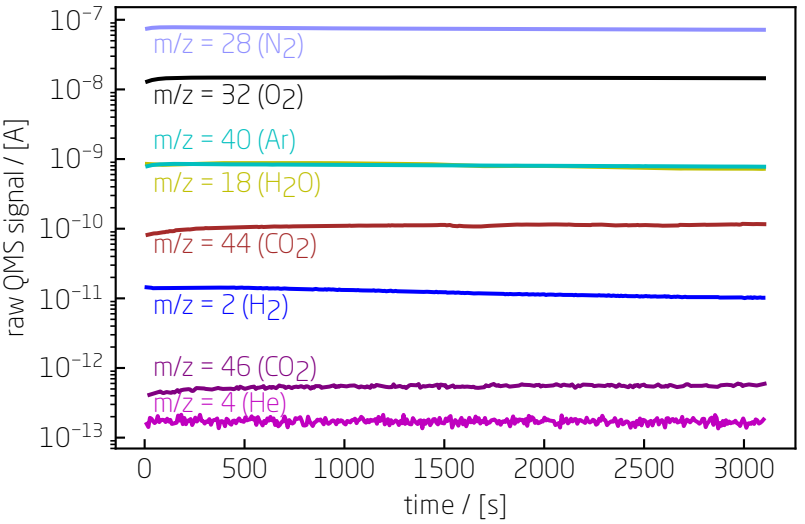

Figure 2.17: The QMS signal from air was measured through a calibrated sniffer chip, providing valuable data for calibration.

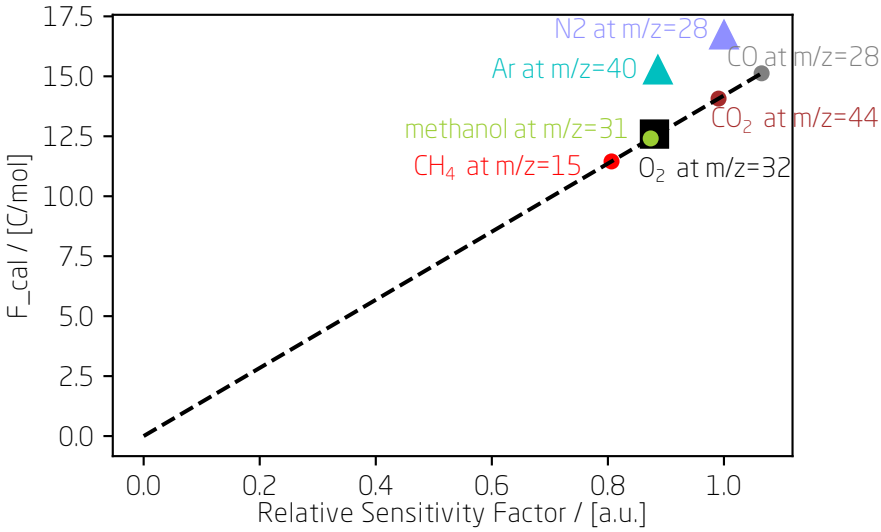

Figure 2.18: Transmission curve from calibrating QMS from air through the sniffer chip. Oxygen is the trusted calibration and N_2, and Ar is given as point calibration for consolidation of the transmission factor $M^{-1/2}$

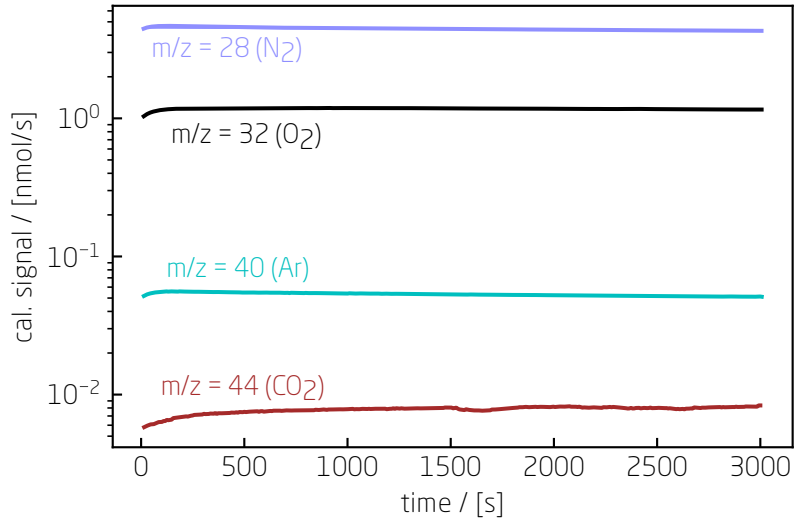

Figure 2.19: QMS calibrated signals using calculated sensitivity factors F for each gas.[42]

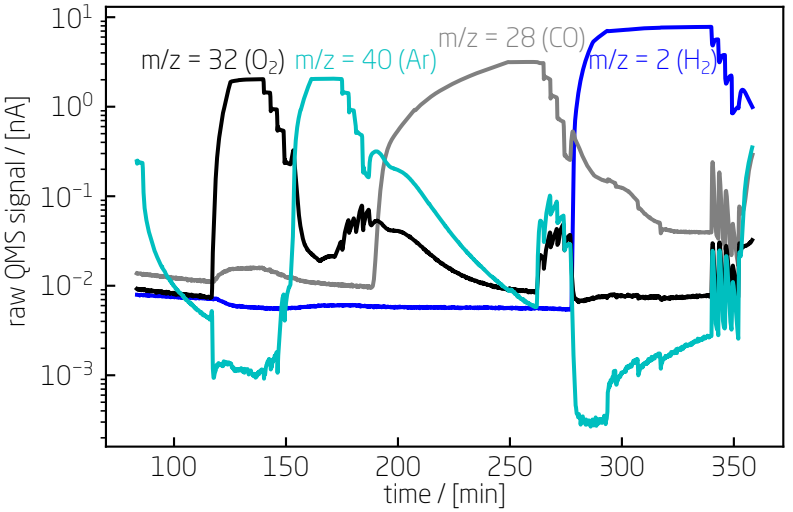

Figure 2.20: Raw QMS signals for calibration of µ-reactor MR 12 using sensitivity factor F for oxygen calculated from previous known oxygen flux through sniffer chip from air. CO, O_2, Ar and H_2 is measured each at 1 bar of 6.0 pure gas for point calibration.

With the newly experimentally found sensitivity factor for oxygen, the sniffer chip can be detached from the microreactorNG setup, allowing any µ-reactor to be mounted, calibrated, and measured as needed.

The procedure involves filling up the µ-reactor with 1 bar of oxygen to *chip calibrate* the capillary of the µ-reactor. The reactor is then evacuated and subsequently filled with 1 bar of Ar, CO, and H_2. These gases will be used to perform *external calibration* of the Ar, CO, and H_2 molecules, as shown in Figure 2.20.

Using the sensitivity factor for oxygen given in Eq. 2.18, a *chip calibration* can be performed for the specific µ-reactor, estimating the effective length of the capillary l_{eff}. This is possible because we know the $F^{O_2}M32$ for the setup and can measure the raw QMS signal $SM32$, enabling the calculation of the oxygen flux through the capillary.

$$\dot{n}^{O_2} = \frac{\mathsf{S}_{32}}{\mathsf{F}_{32}^{O_2}} = \frac{2.5nA}{12.5C/mol} = 0.2\text{nmol/s} \tag{2.19}$$

This value can then be compared with the calculated flux through an ideal capillary using the expression in Eq. 2.7. The resulting scaling factor can be applied to the capillary length in the formula for subsequent flux calculations of other molecules through that µ-reactor. This µ-reactor is now *chip*

calibrated.

By setting the newly estimated effective length equal to the length of the capillary in the mathematical expression for flux through the capillary (given by Eq. 2.7), it is possible to do an *external calibration* of the gases (Ar, CO, H_2) by calculating the flux of each molecule and correlated that to the signal in the QMS.

The latest installed Baratron from MKS 220d can be used to directly measure the gas flux through the µ-reactor, enabling a direct *internal calibration* of gasses in the setup and use for *chip calibration* of the µ-reactor or the photo-microreactor. This makes the use of a *chip calibrated* EC-MS chip obsolete for calibrating the QMS and subsequently *chip calibrating* the µ-reactor from the QMS. This enable faster calibration and more reliable calibration of the sensitivity factors for in-house gasses.

Predictive calibration is well described in [41] and the main equation is:

$$f_M^i = \frac{S_M}{\dot{n}^i} = k\sigma_i \frac{I_M^i}{\sum_{M'} I_{M'}^i} T(M). \tag{2.20}$$

Where k is a proportionality factor, which is set in ECMS python package so $f_{M28}^{N_2}$ = 1 for nitrogen measured at mass 28, σ_i is the ionization cross section, I_M^i represent the intensity in the QMS of the molecule i, $T(M)$ is a combined function called the transmission function which combine the probabilities of a molecule is ionised at the same time the quadropole mass spectrometer filters out that mass to charge ratio and that the ionised molecule hits the secondary electron multiplier. This transmission function is fitted every time to the given data set but is mostly given by

$$T(M) = M^{-1/2} \tag{2.21}$$

This can be seen in action in Figure 2.21 where O_2, CO, Ar, and H_2 has been *external calibrated* and their corresponding calculated relative sensitivity factor f is used to predict the sensitivity factor F for CO_2 and methanol (CH_3OH).

Throughout this thesis the different methods for calibrating and interpreting the raw mass spec signals has been used.

Historical normalization

Historically, normalizing signals to an inert gas within the system (Ar or He) offered two advantages. First, temperature effects on flow rates were removed, simplifying catalysis visualization (see section 2.2.2). Second, differences in capillary dimensions due to manufacturing tolerances were normalized, enabling inter-µ-reactor catalytic activity comparison. However, the inability to determine the exact number of molecules limited the calculation of TOF and comparisons to other research publications.

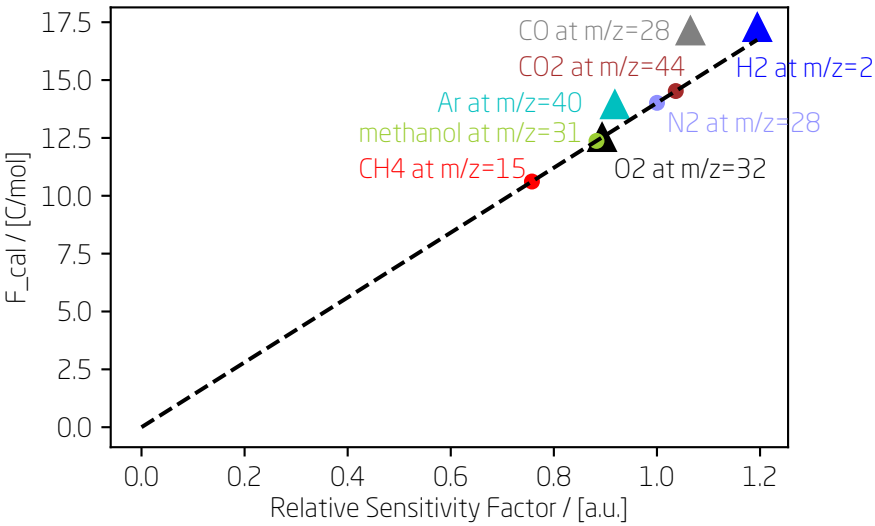

Figure 2.21: Calculated sensitivity factors from relative sensitivity factors using measured sensitivity factors F for four gasses [H_2, O_2, Ar, CO] seen in figure 2.20.

Quantitative calibration of QMS using an EC-MS sniffer chip

Calibrating the QMS with a sniffer chip allows direct molecule counting, but the reliability of direct calibration from the oxygen signal from air through the sniffer chip and estimation of capillary length for other µ-reactors is limited.

Improved chip calibration of the µ-reactors with a Baratron

Using a Baratron for direct flux calculation of different gases allows for directly measuring the QMS sensitivity factor, offering significant advantages over the sniffer chip's indirect method. However, variations in capillary dimensions between chips alter flux and GHSV, complicating direct comparison of two activity plots.

2.4 Related UHV techniques

The thesis utilized two main techniques for characterizing the samples: X-ray Photoelectron Spectroscopy (XPS) and Ion Scattering Spectroscopy (ISS). Additionally, to visually inspect any changes in the morphology of the particles, migration, or sintering during the reaction, selected µ-reactors were examined using Secondary Electron Microscopy (SEM) both before and after the reaction.

X-ray Photoelectron Spectroscopy (XPS)

X-ray Photoelectron Spectroscopy (XPS) is among the most widely used techniques in surface science and catalysis [10]. XPS takes advantage of the photoelectric effect, where electromagnetic waves interact with a solid and kick out electrons to be detected. The kinetic energy of the detected electron is given by:

$$E_k = E_\lambda - E_b - \phi, \tag{2.22}$$

where E_k is the kinetic energy of the detected electron, E_λ is the energy of the incident photon (given by $h\nu$, where h is Planck's constant and ν is the frequency of the photon), E_b is the binding energy of the detected electron, and ϕ is the work function of the analyzer [12]. This relationship enables the identification of each element, and XPS can determine not only the elements present in the solid but also their chemical composition, making it a highly valuable characterization method.

In XPS, the X-ray source is typically an Al or Mg anode that emits X-rays with energies of 1486.3 eV and 1253.6 eV, respectively. When the anode is bombarded with electrons, atoms might become excited and later relax, emitting a photon.

The excited electrons originate from the 1s shell, and the relaxed electron comes from either 2p3 or 2p1. These transitions are denoted $K_{\alpha 1}$ and $K_{\alpha 2}$. The two peaks are separated in energy due to spin-orbit coupling. Additionally, the two peaks are not delta functions of energy but have a broadening of approximately 0.7 eV for Mg anodes and 1 eV for Al anodes at full width half maximum (FWHM) [10]. Other aspects to consider include ghost peaks resulting from anode impurities and satellite peaks caused by the possibility of ions in the anode being left in an excited state. These satellite peaks can be limited by using a monochromator or synchrotron facilities.

The intensity of the incoming electron is given by

$$I = I_0 \text{exp}(-\frac{x}{\lambda}), \tag{2.23}$$

where λ is the mean free path of the electron and x is sampling depth. The mean free path of an electron in a solid follows the universal curve which can be seen in figure 2.22. This curve indicates that, for kinetic energies between 1000 eV and 2000 eV, the mean free path of an electron in a solid is 1-3 nm. Consequently, electrons detected in XPS using either an Al or Mg anode originate from the first five atomic layers, making the technique highly surface-sensitive.

Ion Scattering Spectroscopy, ISS

Ion Scattering Spectroscopy (ISS) is a technique that utilizes binary elastic scattering of ions on a surface, often using He^+ ions. Heavier ions such as

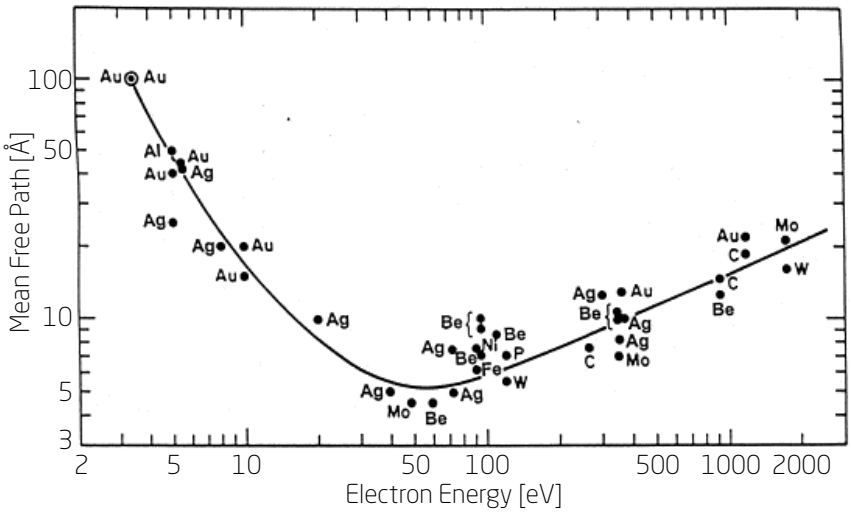

Figure 2.22: Universal curve. The figure depicts the variation in the mean free path of electrons across different materials for varying kinetic energies. Adapted from [43, 44].

Ne^+ can also be employed, potentially increasing sensitivity when scattering on heavier elements, as shown in Figure 2.23. However, using heavier probing ions like Ar^+ and Kr^+ increases the risk of sputtering, which occurs when the ion impacts the surface with enough energy to remove surface atoms. ISS can then reveal information about the elemental composition and atomic-scale structure deeper than the top surface layer in a destructive way.

ISS holds a significant advantage over other surface analysis techniques due to its primary focus on probing the surface layer. The technique is highly surface-sensitive with a depth resolution of about 1-2 atomic layers. For instance, when studying a 50-50 alloy, ISS makes it relatively easy to determine whether one component is segregating to the surface instead of the other. However, the mass resolution of ISS is typically low, and distinguishing between neighboring elements, such as nickel and copper, may not be possible [10]. Assuming only binary elastic collisions, classical mechanics can be used to derive the relationship between the incoming ion mass (M_i) and energy (E_i), the surface atom mass (M_s), and the reflected ion energy (E_r), as energy and momentum are conserved in two-body elastic collisions.

The detected energy is related to the surface atom mass through Equation (2.24):

$$E_r = E_i \left(\frac{\mathrm{Mi}\cos\theta \pm \sqrt{\mathrm{Ms}^2 - \mathrm{Mi}^2 \sin^2\theta}}{\mathrm{Mi} + \mathrm{Ms}} \right)^2 . \tag{2.24}$$

In this equation, θ is the angle between the initial velocity of the first particle and the collision direction, and the $\pm$ sign depends on the direction of the first particle's velocity after the collision. The scattering angle θ is instrument-specific and depends on the geometry of the instrument. As M_i and E_i are user-controlled, M_s can be determined. However, the binary collision model is not entirely accurate, and some inelastic processes might occur during the collision, resulting in a peak shift towards lower energies compared to the values calculated from the equation above.

Figure 2.23 provides a graphical representation of Equation 2.24 with θ = 146.7° and incoming energy E_i = 1000 eV. The lines represent different incoming probing ions M_i = He+, Ne+, Ar+, Kr+, and colored bars display the return energy detected from different surface atom masses probed using He+.

ISS's exceptional surface sensitivity is partly due to the high neutralization probability [10]. Most atoms passing through the first atomic layer are neutralized, so even if they are scattered back to the detector from a sub-surface they do not give a signal in the detector.

The remarkable surface sensitivity of ISS is partially due to the high neutralization probability [10]. Most atoms traversing the first atomic layer become neutralized, so if they are scattered back to the detector from a sub-surface layer, they remain undetected.

Nonetheless, sub-surface contributions can still occur when ions are neutralized, pass through the surface, scatter off a subsurface layer, and then become re-ionized as they exit the surface.

Scanning Electron Microscopy, SEM

Scanning electron microscopy (SEM) is an electron microscopy technique that employs a focused electron beam to systematically scan a sample's surface. The interaction between the electron beam and the sample's surface generates secondary electrons, which are subsequently detected to create a high-resolution image of the surface. SEM serves as a powerful tool for characterizing surface morphology, topography, and chemical composition.

By imaging material surfaces before and after a reaction, SEM can reveal whether particles have migrated, sintered, or undergone other transformations during the reaction process. The technique provides valuable insights into particle size, shape, distribution, and aggregation on a surface, enabling us to study the effects of these factors on catalytic activity and selectivity. Moreover, SEM can be combined with other techniques, such as energy-dispersive X-ray spectroscopy (EDX), to obtain additional information on the elemental composition of the sample.

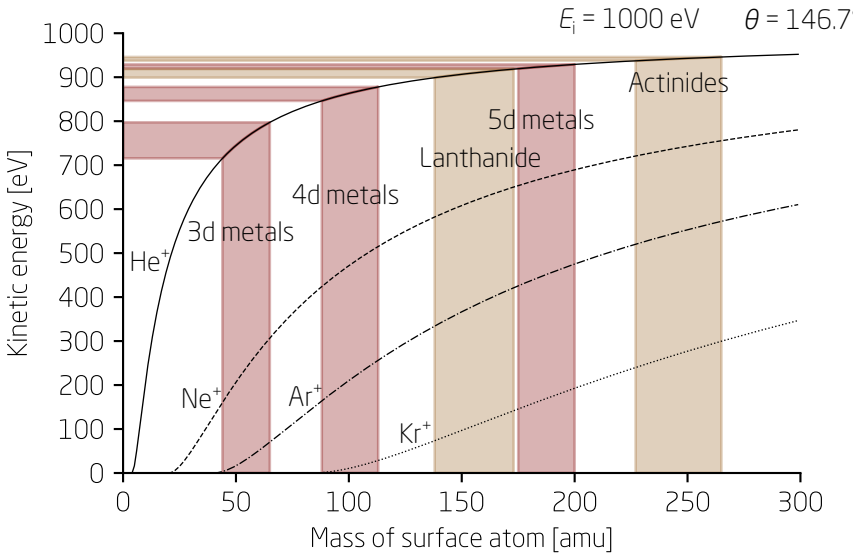

Figure 2.23: A graphical representation of equation 2.24 with θ = 146.7 and incoming energy E_i = 1000eV. The lines represent different incoming probing ions M_i = He+, Ne+, Ar+, Kr+. Coloured bars is showing the return energy detected from different surface atom masses probe using He+, which is the primary usage in this work.

Chapter 3

Improving stability of Au catalysis

This section detail the research efforts and ongoing investigation into Au/Ti alloys aimed at enhancing the stability of Au nanoparticles for CO oxidation.

The work would not have been possible if it was not for the collaboration in science. XPS and ISS spectra obtained from the thetaprobe equipment is done by me where as XPS and ISS spectra obtained by the omicron equipment is done so by the the colleagues operating the cluster source. XPS data analysis is been done using CasaXPS software and handbook look ups and ISS spectra is analysed with python scripts. SEM images of small entities are mainly acquired by colleagues from NanoLab and data analysis is done using ImageJ software. ETEM images are acquired by colleagues from VISION.

The main research question: *How does alloying Au with Ti prior to deposition on a substrate affect the stability and catalytic activity of the resulting catalyst for low temperature CO oxidation?*

The challenge of Au as a catalyst can potentially be addressed by stabilizing Au with a second metal, such as Ti, before deposition on a support substrate. This research investigates the catalytic activity of mass-selected Au and AuTi nanoparticles on various substrates using the CO-oxidation as a model reaction, employed to minimize the formation of undesired by-products.

Au catalysis

Au is a well-known material for illustrating size-effects in catalysis [47]. Despite being chemical inert, Au readily forms alloys and inter-metallic compound with other metals [47]. Au was reported to facilitate the combination of O_2 and H_2 as early as 1906 [48], and catalyze the oxidation of CO to CO_2 since 1925 [49]. However, it was not considered a catalyst until Haruta and co-workers found that metal oxide supported Au nanoparticles could effectively catalyze CO oxidation, even at -70°C [14, 50, 51].

Experimental results of the CO oxidation activity of Au nanoparticles on different supports as a function of particle size show that Au particles are only active below about 5 nm in diameter, and become more active as size decreases [52]. The size effect of the small Au nanoparticles can be seen in Figure 3.1 with an optimum around 3 nm. This size effect is more pronounced than the dependence of activity on the support material, and explanations ranging from the perimeter length of Au-TiO_2, uncoordinated sites,

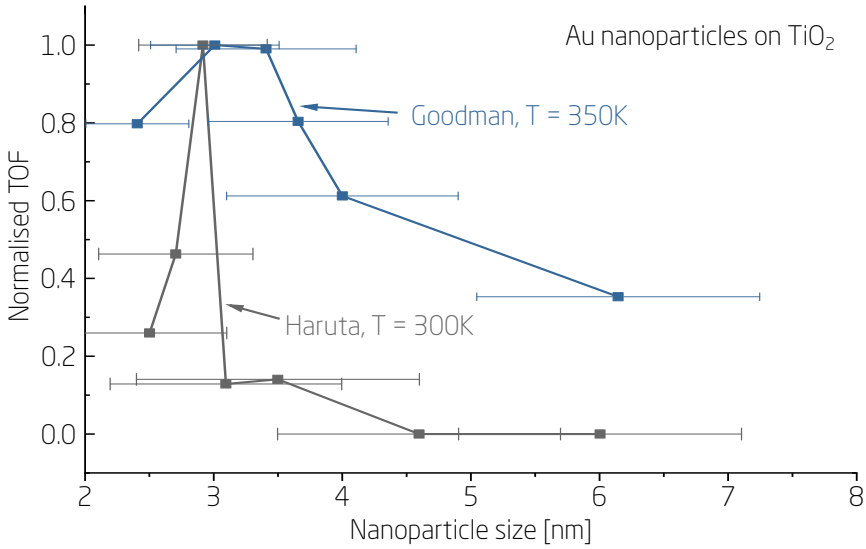

Figure 3.1: Normalized TOF vs. particle diameter for Au nanoparticles on TiO_2. Data is from literature [45, 46].

and quantum size effects, have been proposed for the source of the activity of Au nanoparticles and its support dependence [51, 52, 53, 54].

A major issue with using Au particles as a catalyst is their rapid sintering. Au atoms can migrate and form 3D islands on a TiO_2 surface, even at low temperatures [55, 56]. On TiO_2, Au clusters sinter via Ostwald ripening between 300 K and 410 K, with sintering accelerated in the presence of a CO and O_2 mixture [57]. Fewer studies exist on the behavior of Au on SiO_2, likely due to the lack of catalytic activity. However, research on Au growth on thin SiO_2 has shown that Au clusters preferentially occupy various defects on the SiO_2 surface [58]. Adding TiO_2 to a SiO_2 surface reportedly stabilizes Au clusters and dramatically reduces their sintering rate [59].

Recently, our group, in collaboration with others, introduced a new method based on alloying Au with Ti [60]. AuTi nanoparticles were deposited onto a SiO_2 support using a cluster source, demonstrating reduced sintering compared to pure Au nanoparticles.

Inspired by this enhanced stability, we test the CO oxidation activity and stability of AuTi nanoparticles in the μ-reactor by depositing mass-selected AuTi nanoparticles on pristine SiO_2 μ-reactors and TiO_2 thin film coated μ-reactors.

The particle size was adjusted to explore the previously reported size effect and to identify the optimal AuTi nanoparticle size, while considering the structural differences compared to Au nanoparticles [61]. Moreover, we

tested Au nanoparticles on both supports to establish a comparative reference for the AuTi particles.

While Au can catalyze a variety of reactions, CO oxidation is a commonly studied reaction in surface science [10].

However, this study seeks to demonstrate that unstable particles can attain self-anchoring by incorporating a stabilizing element through alloying.

CO oxidation as a model reaction

Researchers have studied Carbon monoxide (CO) oxidation since the 1920s, when platinum (Pt) was found to exhibit excellent catalytic properties for this reaction [62].

CO oxidation is a critical chemical process that converts the toxic CO molecule into carbon dioxide (CO_2), as represented by the overall reaction in

$$CO + \frac{1}{2}O_2 \rightarrow CO_2. \tag{3.1}$$

This reaction is relatively straightforward, consisting of four reaction steps, with * representing an adsorption site on the surface of the catalyst:

$$CO + ^* \rightleftharpoons CO^* \tag{3.2}$$
$$O_2 + ^* \rightleftharpoons O_2^* \tag{3.3}$$
$$O_2^* + ^* \rightleftharpoons 2O^* \tag{3.4}$$
$$O^* + CO^* \rightleftharpoons CO_2 + 2^* \tag{3.5}$$

The two primary applications of catalysts based on Au-nanoparticles for CO oxidation reactions are: (i) Oxidation of CO in catalytic exhausts: Cold engine starts account for approximately 80% of pollution caused by vehicles and contribute significantly to air pollution[62]. (ii) Hydrogen purification: CO negatively impacts the Pt electrodes in fuel cells. Au nanoparticles have the potential to minimize CO-poisoning of the Pt-catalyst electrodes at low fuel cell temperatures since Au nanoparticles supported on transition metal oxides act as active catalysts for oxidation reactions at low temperatures [15].

Commercial automotive catalysts predominantly use platinum group metals, such as platinum (Pt), palladium (Pd), and rhodium (Rh) [63]. One challenge associated with this group of metals is their inactivity below 200°C, leading to most pollutants being released within the first five minutes of engine operation [64]. In search of an alternative, Au nanoparticles have garnered interest for their capacity to catalyze CO oxidation [65].

The use of Au single atoms as catalysts exhibits remarkable preferential CO oxidation, also known as CO-PROX, and appears to be a promising strategy for removing excess amounts of CO from H_2 gas streams before they are used in fuel cells [66].

The AuTi bimetallic nanoparticles

The AuTi nanoparticles was deposited by the cluster source team at SurfCat on both pristine μ-reactors and μ-reactors with 100 nm TiO_2 thin film sputtered on the SiO_2 giving two different substrate supports to investigate. AuTi and Au nanoparticles were deposited using a 50/50 at% Au/Ti alloy target and a pure Au target, respectively.

The AuTi target's 50/50 Au/Ti at% composition does not guarantee the same composition in particles. XPS was used to check the ratio on 2.5 nm AuTi on SiO_2 samples, revealing an average Au/Ti atomic composition of 30/70 ± 1.8%. The XPS spectra is subtracted a Shirley background to model the inelastic scattering of electrons leaving the sample and the area is fitted with a Gaussian function. Scofield relative sensitivity factors (RSF) is used in CasaXPS for Au and Ti to determined the ratio.

A representative XPS spectrum is shown in Figure 3.2 with detailed scans of the Au 4f and Ti 2p regions used for quantification. The position of the Ti 2p3/2 peak at 458.5 eV in the Ti 2p peaks suggests that Ti is in an oxidized state. Ti 2p3/2 peak is shifted compared to metallic Ti at 454 eV. Simultaneously, the Au 4f7/2 peak located at 84 eV is indicative of metallic Au [67].

Niklas Secher, conducted STEM characterizations of the mass-selected AuTi nanoparticles after deposition using the cluster source. Figure 3.3a displays a STEM image of a 4.5 nm AuTi nanoparticles. The TEM instrument was set to dark field and hence heavier atoms with more mass appear brighter. The particles have a bright clear core structure surrounded by a less bright shell structure.

Furthermore, an EDS linescan across a 5.5 nm AuTi nanoparticle was performed during the STEM characterisation session. This linescan is displayed in Figure 3.3c, presenting the distribution of Au and Ti across the particle. From Figure 3.3a and c, it becomes evident that the AuTi alloy segregates into a region containing Au and another containing Ti. The EDS linescan implies that a Au particle is embedded within a Ti nest. This observation aligns with Tang et al. [68], who discovered that Au nanoparticles on TiO_2 surfaces tended to form a similar nested structure around the Au nanoparticles, likely due to the strong metal-support interaction (SMSI) between Au and Ti.

The size distribution of the Au core for AuTi nanoparticles with sizes of 2.5 nm, 3.5 nm, 4.5 nm, and 5.5 nm is depicted in Figure 3.3b. Multiple STEM images of the different sized nanoparticles is analysed using the ImageJ software to identify the particles and measure the diameter to create the histogram. This is done by applying the a "Threshold" to create a mask with the nanoparticles in question and "Analyse Particles" to measure the area of the particles.

For calculating the turn-over-frequency, the size distribution of the Au-core

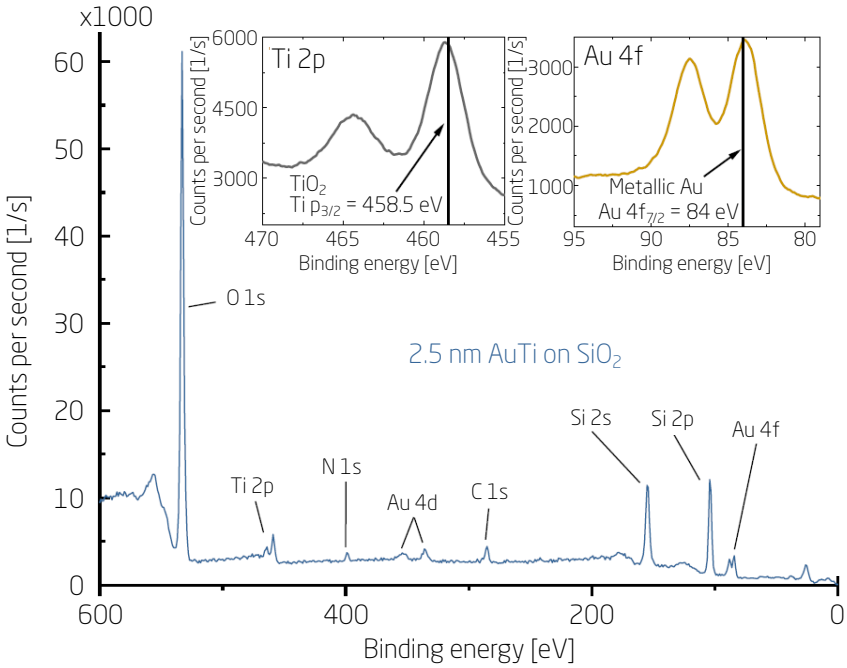

Figure 3.2: Region of survey XPS spectrum of 2.5 nm AuTi on SiO_2. O, Ti, N, Au, C, Si peaks are labeled. Detailed scans of Au 4f peaks and the Ti 2p is inset. The spectrum was calibrated to adventitious carbon at 284.8 eV. XPS spectra obtained with omicron.

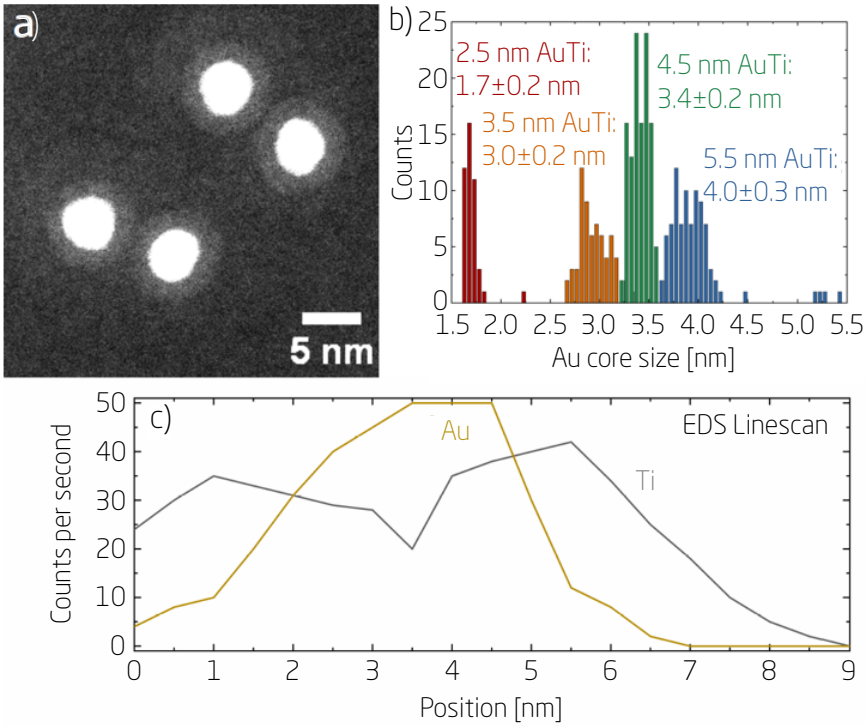

Figure 3.3: a) STEM image of the 4.5 nm AuTi nanoparticles. The brightness was enhanced to show the dark shell. b) Au core size distributions for the 2.5, 3.5, 4.5 and 5.5 nm AuTi particles. c) EDS linescan across a 5.5 nm AuTi nanoparticle showing the Au and Ti profiles. Adapted and updated from [30].

within the AuTi nanoparticles is used to estimate the number of active sites. This is because Ti is expected to be catalytic inert towards CO oxidation.

A comparison of intrinsic catalytic activity should ideally be made between the Au-core of the AuTi nanoparticles and pure Au nanoparticles.

In industrial and commercial contexts, intrinsic activity becomes less significant, where the focus shifts towards comparing activity per mass, as it closely relates to cost, an essential consideration for commercial applications.

Figure 3.4 displays a TiO_2 thin film sputtered µ-reactor with 3.5 nm AuTi nanoparticles after deposition, but before anodic bonding and testing. Heavier elements will appear brighter in the SEM image and the Au-core will light up compared to the TiO_2 substrate. The dark almost black parts of the image is attributed to an in-homogenoues thin film deposition of the TiO_2 sub-

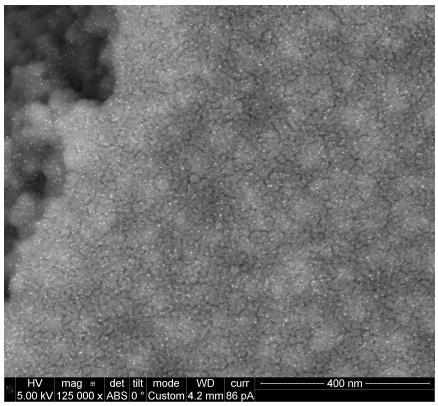

(a) SEM image of 3.5 nm AuTi on TiO_2. Scalebar is 400 nm.

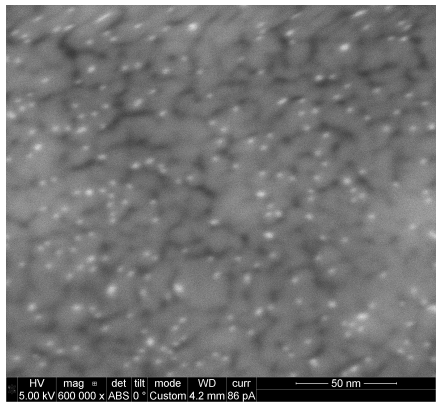

(b) SEM image of 3.5 nm AuTi on TiO_2. Scalebar is 50 nm.

Figure 3.4: SEM images of 3.5 nm AuTi nanoparticles on TiO_2 on a µ-reactor prior to anodic bonding.

strate. From both 125k (a) and 600k (b) magnifications, it is evident that the deposited nanoparticles are homogeneously distributed and well-dispersed over the samples, with particle sizes ranging from 3 to 5 nm.

In Figure 3.5, AuTi nanoparticles on TiO_2 are shown on a µ-reactor after activity testing. The AuTi nanoparticles were catalytic active towards CO oxidation. The nanoparticles have undergone sintering, resulting in a minimum observed particle size of 10 nm and the majority measuring approximately 50 nm in diameter. The AuTi alloy is either catalytic active at larger dimensions than what is observed for pure Au nanoparticles or smaller nanoparticles are not well dispersed hiding on the sample difficult to find.

Measurement procedure
The CO oxidation measurement procedure includes the following steps:

1. Argon flow is passed through the µ-reactor and its connected tubes, followed by pumping down the system. This step is repeated twice to ensure thorough removal of any residual gas from previous experiments.

2. A flow rate ratio of 2:1:1 mL/min O_2:Ar:CO is applied for 20 minutes before switching to a 1:1:1 mL/min flow rate ratio of O_2:Ar:CO. This step prevents the Ar/CO mixture in the inlet I2 from filling up at a faster rate than O_2, thus delaying the steady-state gas mixture. As depicted in Figure 2.8, CO and Ar share the same gas line (I1), while O_2 has a separate line (I2). The doubled flow rate of O_2 ensures equal gas flow in both lines, preventing Ar and CO from filling up into the I2 gas line until 1 bar of pressure is reached in the system. The 1:1:1 flow of

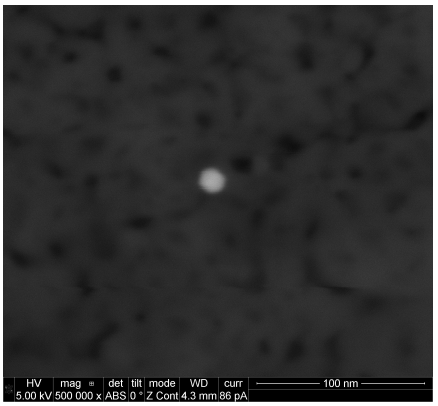

(a) SEM image of 4.5 nm AuTi on TiO_2 after activity testing.

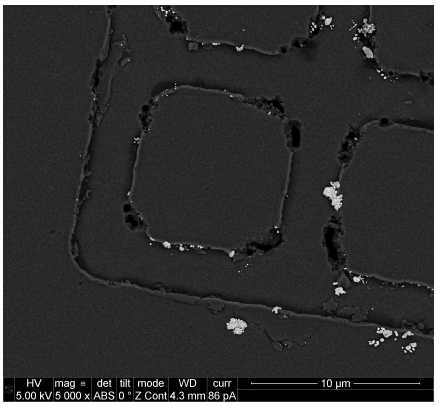

(b) SEM image of 4.5 nm AuTi on TiO_2 after activity testing.

Figure 3.5: SEM images of 4.5 nm AuTi nanoparticles on TiO_2 on a µ-reactor after activity testing. The nanoparticles has sintered and the smallest particles found are 10 nm with the majority having a size of 50 nm in diameter.

O2:Ar:CO is then passed through the reactor for another 20 minutes to establish stable flow.

3. The temperature is increased to either 525 K at a rate of 4 K/s, with the thermocouple controlling the temperature, or to 625 K at a rate of 10 K/s, with the RTD controlling the temperature. The reasons for the two different methods are explained in 2.2.1 and further discussed in 4.3.

4. The temperature is maintained constant for a duration between 20 minutes and 1 hour.

5. The temperature is decreased back to room temperature using the same ramp rate as during the initial increase.

In Figure 3.6, a plot of a standard experiment is shown without the calibration. As can be seen, a mass scan is performed every hour to potentially discover and monitor unexpected masses.

In Figure E.1 in the appendix a standard Arrhenius plot for an active AuTi nanoparticle is shown and the interval for which is used to calculate the apparent activation energy Ea is emphasised.

Stability of AuTi

To investigate the performance of a µ-reactor over time, four sequential CO oxidation experiments were carried out on the same AuTi on SiO_2 µ-reactor with 2.5 nm nanoparticles, months apart. The temperature was controlled

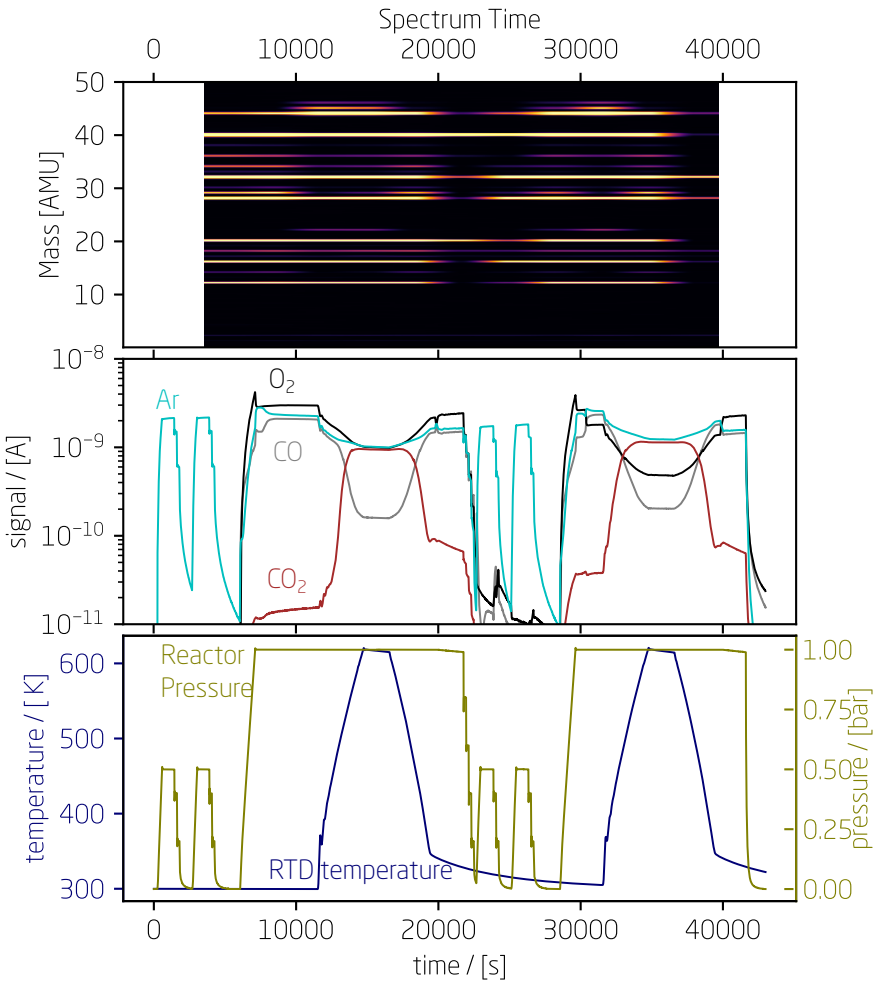

Figure 3.6: The standard plot of an experiment. Top panel display the hourly produced mass scan to monitor minute amounts of not expected molecules. The bottom panel display the temperature and pressure profile during the experiment. The middle panel display the masses monitored continuously through mass time.

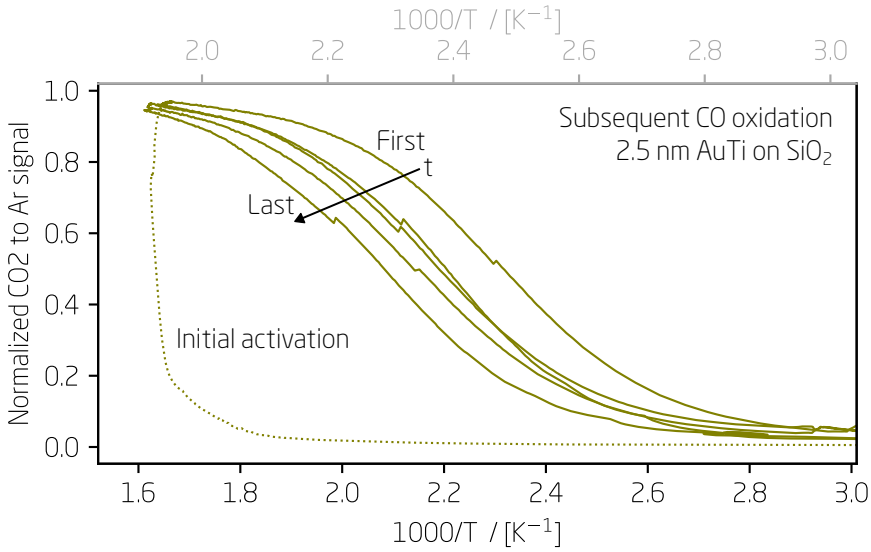

Figure 3.7: Consecutive CO oxidation experiments performed on the same µ-reactor containing AuTi nanoparticles of 2.5 nm on SiO_2. The first and last experiment is almost 2 months apart. The CO_2 signal is normalised to the Ar signal. The activity decreases over time but otherwise is during experiment very stable. Top axis is the temperature measured by the thermocouple and bottom axis is the temperature measured by the RTD.

using the thermocouple and ramped up to 525 K (shown in grey on the top panel), which corresponds to approximately 625 K as measured by the RTD (shown in black on the bottom panel). The CO oxidation was maintained constant for 1 hour before being ramped down. Figure 3.7 presents the calibrated CO_2 signal normalized to the Ar signal, plotted against the inverse temperature in [1000/K]. The ”First” refers to the experiment conducted immediately after initial activation, while the ”Last” represents a measurement taken almost two months later. The black arrow and ’t’ indicate the progression of experiments over time. The data reveals that the onset temperature decreases over time, but the reaction still reaches full conversion, with all CO being depleted from the gas stream even after extended storage.

It is important to highlight the activation step occurring around 650 K (as measured by the RTD), indicated by the dotted line in Figure 3.7. All catalytically active µ-reactors have exhibited this activation step, and the reactors appear completely inactive until this point.

The consistently high CO oxidation activity of stable AuTi nanoparticles is in line with the ETEM studies conducted by Stefan Kei Akazawa. The ETEM profile is shown in Figure 3.8. The top panel of the Figure display the thermodynamic parameters partial pressure and temperature defined by me and

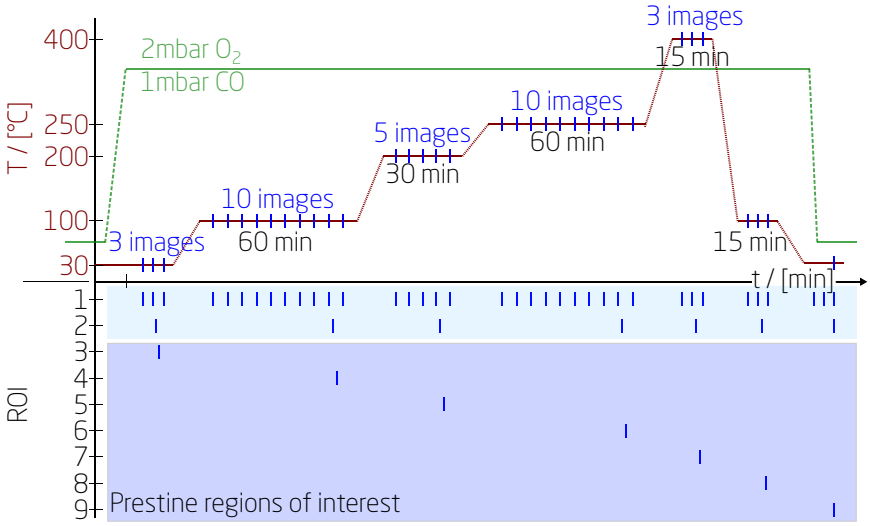

Figure 3.8: Experimental profile of ETEM measurements performed by PhD student Stefan (VISION). Blues lines indicates images taken at that Region of Interest (ROI). Few areas are continuously monitored to investigate sintering effects and multiple prestine areas are investigated and images once to monitor and account for beam influence and beam damage. Temperature from 30 - 400°C and pressure profile is plotted in the top part of the figure.

the bottom panel display the strategy for taking images accounting for possible beam effects defined by Stefan Kei Akazawa. These ETEM studies are performed at 2 mbar O_2 and 1 mbar of CO, with temperature plateaus initially at 30°C, followed by 100°C, 200°C, 250°C, and 400°C. The partial pressure is chosen to mimic the oxygen rich reaction condition the activity test is performed at. The activation of the nanoparticles is anticipated to occur at 250°C, so this step is maintained for an hour. The 15-minute step at 400°C is chosen to observe potential sintering effects on the stable AuTi nanoparticles at these elevated temperatures. A pristine region of interest (ROI) is imaged at each new temperature step to monitor beam effects on the sample.

The AuTi nanoparticles during ETEM can be seen in Figure 3.9. Three identically located AuTi nanoparticles are highlighted with red circles for each temperature step. As observed from monitoring one region, the AuTi nanoparticles remain highly stable even at elevated temperatures of 400°C throughout the entire measurement.

In Figure 3.10, the ETEM of Au nanoparticles is displayed. As expected, these Au nanoparticles exhibit less stability and begin to move around the sample as the temperature increases.

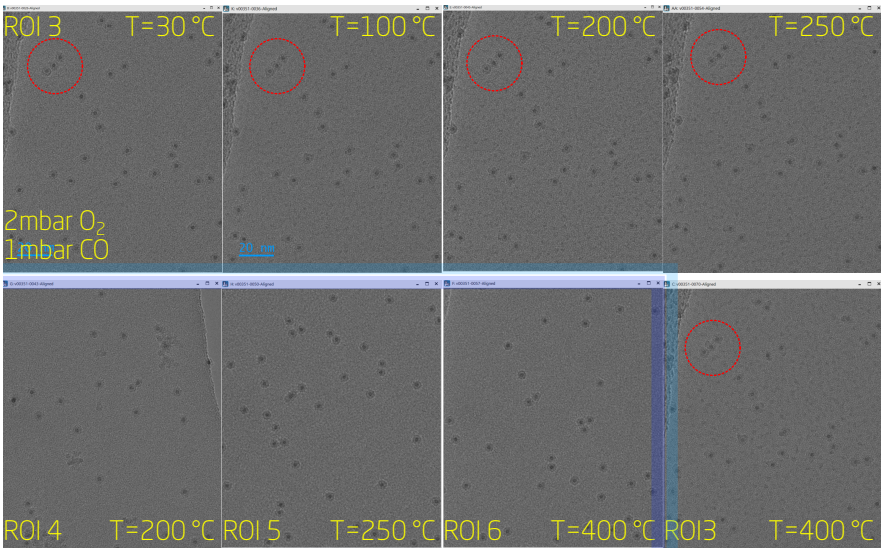

Figure 3.9: The figure illustrates the structural effects on AuTi nanoparticles during a multi-hour experiment conducted at elevated temperatures and pressures above vacuum (3 mbar). Region 3 of Interest (ROI3) is monitored and tracked at every temperature step, ranging from 30°C (top left) to 400°C (bottom outer right). ROI4 (bottom most outer left), ROI5 (bottom inner left), and ROI6 (inner right) are pristine areas used to observe the beam's influence and potential beam damage. Three identically located AuTi nanoparticles are highlighted with red circles. As seen from the monitoring of ROI3, the AuTi nanoparticles remain highly stable even at elevated temperatures throughout the entire measurement.

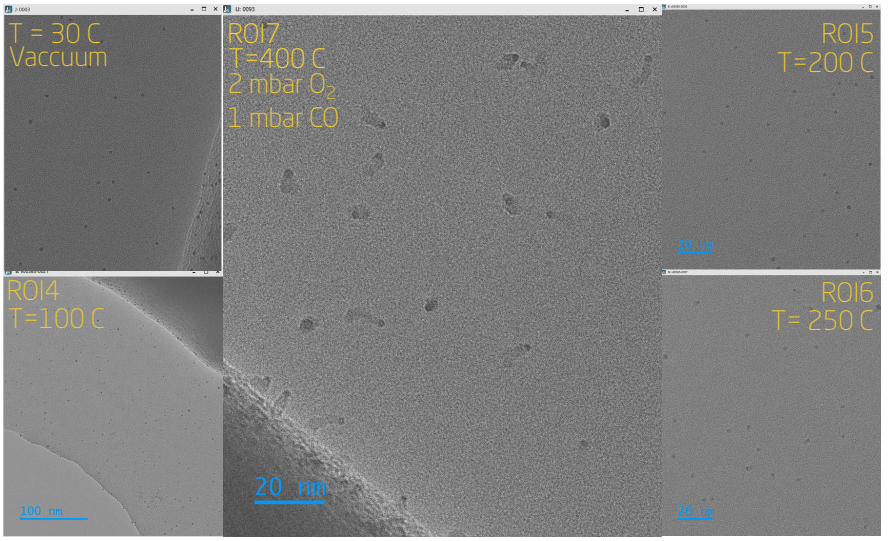

Figure 3.10: The figure illustrates the structural effects on Au nanoparticles during a multi-hour experiment conducted at elevated temperatures and pressures above vacuum (3 mbar). Five pristine regions of interest at various temperatures are displayed. As seen in the highlighted central TEM image, the Au nanoparticles exhibit instability at elevated temperatures, in contrast to the AuTi nanoparticles.

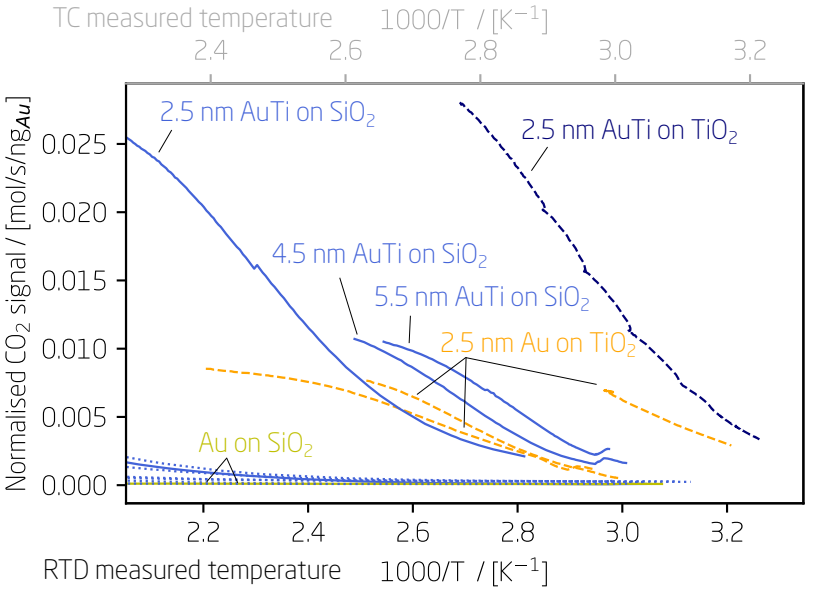

Figure 3.11: The mass activity of the tested µ-reactors is plotted against the inverse temperature. The top grey-colored axis represents the temperature measured by the thermocouple, while the bottom x-axis corresponds to the temperature measured by the RTD. The calibrated CO_2 signal is normalized according to the mass of the Au-core in each sample. The light blue solid line indicates AuTi on SiO_2, and the dark blue dashed line represents AuTi on TiO_2. The yellow solid line corresponds to Au on SiO_2, and the orange dashed line signifies Au on TiO_2. The particle size is denoted next to each line.

Activity Results

Ideally, turnover frequency (TOF) should be employed to measure catalytic activity, but estimating the exact number of sites would be speculative at best due to the uncertain structure of AuTi bimetallic nanoparticles. Consequently, mass activities, which have economic relevance, are utilized.

Figure 3.11 illustrates the normalized CO_2 signal against the inverse temperature for various tested µ-reactors. The top grey-colored axis represents the temperature measured by the thermocouple, while the bottom x-axis corresponds to the temperature measured by the RTD. Dashed lines represent TiO_2, and solid lines indicate SiO_2. Blue hues are associated with AuTi nanoparticles, and yellowish colors represent Au nanoparticles. The CO_2 signal for Au nanoparticles is normalized by the total Au mass calculated from the cluster source deposition and particle mass. The CO_2 signal for AuTi nanoparticles is normalized by the estimated Au core size from the distribution observed in Figure 3.3. The particles are then assumed to be spherical with a bulk Au density of 19.3 g/cm^3.

Only one reactor of each type displayed CO oxidation activity, except for 2.5 nm Au on TiO_2, where three reactors tested are active and two showed similar mass activities, while the third displays mass activity at lower temperatures. Figure 3.11 reveals that the samples containing 3.5 nm AuTi, multiple 4.5 nm AuTi, and both 2.5 nm Au and 3.5 nm Au on SiO_2 are not active for CO oxidation, which was expected for the 2.5 and 3.5 nm Au on SiO_2 samples. Furthermore, 2.5 nm AuTi on TiO_2 is the most active with a much lower onset temperature than the other AuTi μ-reactor. At 360 K ($\approx$ 2.8 [1000/K] measured by the RTD), 5.5 nm, 4.5 nm, 2.5 nm AuTi on SiO_2, and 2.5 nm Au on TiO_2 exhibit comparable CO oxidation mass activities. Among them, 2.5 nm AuTi on SiO_2 has the highest mass activity, followed by the 5.5 nm AuTi on SiO_2 and 4.5 nm AuTi and 2.5 nm Au on TiO_2, which have similar activities considering the temperature uncertainty.

Considering that Au is recognized for its activity on TiO_2 supports, the observed activity of 2.5 nm AuTi on TiO_2 is not unexpected. However, it is surprising to see that it exhibits considerably higher CO oxidation mass activity than two of the 2.5 nm Au on TiO_2 samples, given that the active sites in both samples are Au. The lack of activity in the 3.5 nm AuTi on SiO_2 sample is probably attributable to reproducibility issues, as both smaller and larger particles demonstrate activity.

In Table 3.1, the apparent activation energy is calculated for various active samples. The apparent activation energy appears to be similar for both 2.5 nm AuTi on TiO_2 and SiO_2, with the 2.5 nm AuTi nanoparticle on SiO_2 exhibiting the lowest value. The 2.5 nm Au on TiO_2 displays a comparable activation energy.

It is important to note that three of the μ-reactors (2.5 nm Au on TiO_2, 4.5 nm, and 5.5 nm AuTi on SiO_2) experienced a loss of connection to the RTD. Consequently, the activation energy calculations were based on thermocouple (TC) measurements, which are expected to be inaccurate. This issue appears to have led to the calculated apparent activation energy for the 2.5 nm Au on TiO_2 being roughly twice its actual value. If this is also the case for the 4.5 and 5.5 nm AuTi on SiO_2 samples, their apparent activation energies could be 2-3 times larger than those of their 2.5 nm counterparts. These apparent activation energies are comparable to those reported in the literature, where Haruta and colleagues found apparent activation energies (E_a) ranging from 20 kJ/mol to 60 kJ/mol for Au nanoparticles of sizes 2-3 nm and 4-5 nm, respectively [45].

This type of thermal catalytic data analysis has been programmed in python and added to the open source package IXDAT as a 'reactor' class enabling calibration of specific reactors, plotting the (un)calibrated signals in multiple panels and plotting Arrhenius like plots with the possibility to calculate the apparent activation energy from a specific temperature or time span [69].

Figure 3.12a, 3.12b, and 3.12c display SEM images of the same location

Table 3.1: Apparent activation energy values sorted by size and color-coded by catalyst and support

Size (nm)	Catalyst	Support	Apparent E_a (kJ/mol)
2.5	AuTi	TiO_2	39
2.5	Au	TiO_2	63 (TC)
2.5	Au	TiO_2	36
2.5	Au	TiO_2	31
2.5	AuTi	SiO_2	32
4.5	AuTi	SiO_2	122 (TC)
5.5	AuTi	SiO_2	173 (TC)

before and after the reaction on a µ-reactor with AuTi on TiO_2.

The µ-reactors are equipped with five distinct grids etched into the reactor volume, with each grid organized into 5 columns and 5 rows.

The strategy to pinpoint an identical location within a grid, is to take a SEM image of the chosen grid. Focus on a distinct, easily observable feature, and magnify in for a closer look while still easily observing this feature in the new image. The edges of the pillars in the grid are commonly used as features because they are typically distinct from each other. This magnifications process continues to zoom in further, each time selecting a new, clear feature as the focal point. After six iterations of the process the SEM image is magnified enough, allowing for visual inspection of nanoparticles in identical location.

The nanoparticles appear to have sintered into larger particles as seen in 3.12b and 3.12c.

No nanoparticles seems to be the same after testing as to prior testing and the SEM images from identical locations show no significant stability in the morphology or positioning of the nanoparticles.

This phenomenon could be the underlying cause of some of the reproducibility issues, which is discussed in greater detail in section 4.2.

Summary
The high mass activity of 2.5 nm AuTi nanoparticles exhibits an earlier onset compared to pure 2.5 nm Au on TiO_2, which complicates the direct comparison between AuTi and Au nanoparticles. This emphasizes the necessity of optimizing AuTi catalysts by fine-tuning the optimal size of AuTi nanoparticles. The size-dependent results indicate that, in two instances, both the 4.5 nm and 5.5 nm AuTi on SiO_2 demonstrate greater activity than 2.5 nm Au on TiO_2. To eliminate the influence of particle size and structural effects in the comparison, more Au particle sizes should be tested, given the reported size effects. Among the AuTi on SiO_2 particles examined, the 5.5 nm AuTi particles with an estimated 4 nm Au core exhibit the highest activity. This

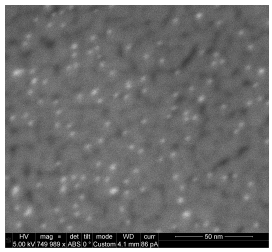

(a) MR63 identical location before

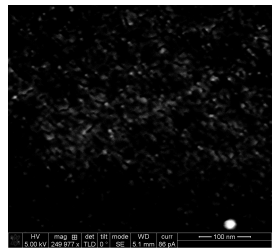

(b) MR63 identical location after 1

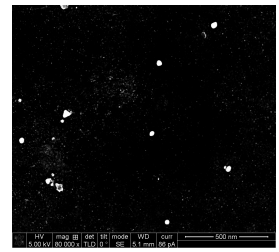

(c) MR63 identical location after 2

Figure 3.12: SEM images of 4.5 nm AuTi nanoparticles on TiO_2 on a µ-reactor after activity testing. The nanoparticles has sintered and the smallest particles found are 10 nm with the majority having a size of 50 nm in diameter.

size is 0.5-1.5 nm larger than the sharp optimum reported in the literature. The size-dependent activity effect may depend on the metal-support interface structure, and the optimal particle size for AuTi nanoparticles could differ from that of pure Au nanoparticles. The ongoing testing of additional AuTi particle sizes on TiO_2 support aims to identify the ideal size for AuTi particles. However, due to reproducibility issues, these results have not yet been experimentally repeated.

The inconsistent CO oxidation activities observed for similarly prepared reactors imply that particles may not be entirely identical, even for samples with the same particle size, despite maintaining consistent particle compositions and deposition conditions. This challenge is discussed in more depth in section 4.2.

Furthermore, there was no observed link between the CO oxidation activity and the quantity of Au present on the surface of the particles in their deposited state. When examining the inactive samples, it appears that the strong interaction between the metal and support causes Au to become concealed by Ti. Changes in the TiO_2 shell at elevated temperatures during anodic bonding could potentiallty lead to a passivating TiO_2 shell enveloping the Au metal.

This study sought to determine whether AuTi nanoparticles could serve as a more stable alternative to Au nanoparticles. So far, activity measurements suggest that AuTi particles on both SiO_2 and TiO_2 supports can match or even exceed Au in CO oxidation mass activity. AuTi nanoparticles on a SiO_2 support have been reported to display enhanced stability against sintering under an electron beam. However, this was under much lower temperatures and pressures than what the particles undergo during CO oxidation testing [60]. Consequently, the stability of these particles must be inves-

tigated within the μ-reactor system and compared to the stability of Au on TiO2.

Chapter 4

Difficulties using the μ-reactor-platform

It is important to maintaining the equipment and employing accurate diagnostic tools. This is especially true when experimental methods probe smaller scales, where the risk of contaminants and false positives increases. These considerations are no less significant using the μ-reactor platform.

This chapter delves into three cases that underscore the importance of addressing contaminants, false positives, and accurate temperature measurements in the μ-reactor. These cases involve catalytic CO oxidation in active pristine reactors, non-reproducible results, and thermal measurement and control challenges. Each case serves as a reminder of the potential pitfalls that researchers may face in their pursuit of groundbreaking discoveries.

In the first case, we examine catalytic CO oxidation in active pristine reactors, which demonstrates the significance of ensuring that the reactor environment remains free from contaminants. The second case explores non-reproducible results, highlighting the need for robust and consistent experimental procedures. Finally, the third case focuses on thermal control, emphasizing the importance of accurate temperature measurements in thermal catalysis studies. By examining the challenges and solutions presented in these three cases, this chapter aims to emphasize the importance of maintaining equipment, employing accurate diagnostic tools, and adopting a meticulous approach to research. Ultimately, the pursuit of scientific understanding demands rigor and precision, which are key to unlocking the full potential of the μ-reactor platform and its numerous applications.

4.1 Catalytic active pristine μ-reactors

In this section, we will explore the reasons behind the unexpected catalytic activity observed in certain pristine μ-reactors. Our conclusion is drawn from the evidence presented in figure 4.1. The data reveals that the AuTi nanoparticles demonstrate CO oxidation activity at lower temperatures than the contaminated pristine μ-reactors. Therefore, conducting CO oxidation activity measurements on Au-based catalysts within the μ-reactor at temperatures lower than those affected by contamination can produce reliable data that reflects the true catalytic activity of Au. This work has been conducted in close collaboration with Olivia Fjord Sloth, a former master's student and now a fellow PhD colleague at SurfCat.

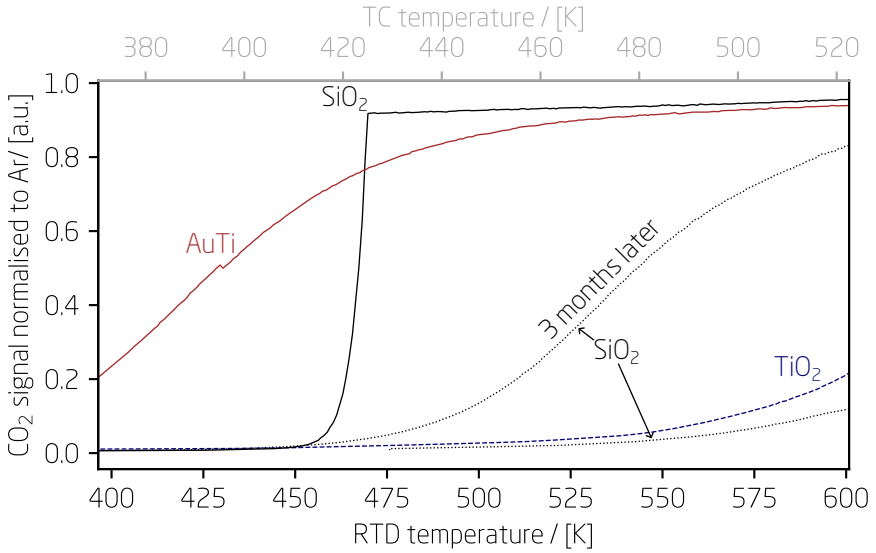

Figure 4.1: The CO_2 QMS signals normalised to Ar is plotted as a function of RTD-measured temperature on the bottom x-axis and TC-measured temperature in vacuum on the top x-axis. The red line labeled ”AuTi” represents a µ-reactor containing 2.5 nm AuTi catalyst with 5% coverage on a SiO_2 substrate. The black solid line labeled ”SiO_2” is a pristine reactor received from the cleanroom fabrication. The black dashed line labeled ”SiO_2” represents a pristine µ-reactor without catalyst, measured twice with a 3-month interval, showing unexpected differences in CO oxidation activity. Finally, the blue line labeled ”TiO_2” corresponds to a pristine µ-reactor with a 50 nm TiO_2 thin film.

Sudden CO oxidation activity from pristine µ-reactors

In our study of bi-metallic AuTi alloy, we observed unexpected activity in pristine µ-reactor. These µ-reactors are bonded directly as received from the fabrication process in the cleanroom, meaning that the reactor area is clean and free of any deposited nanoparticles or other substrates besides SiO_2 that may have been sputtered. Consequently, these reactors are expected to be inert and inactive towards any chemical reactions and show no catalytic activity. An empty µ-reactor, also known as a blank µ-reactor, is a µ-reactor that does not have any catalytic nanoparticles deposited on it, and thus it is expected to show no catalytic activity. However, unlike a pristine µ-reactor which is bonded with a clean SiO_2 substrate, an empty µ-reactor can have an inert substrate other than SiO_2, such as TiO_2.

At the outset of this project, we tested two µ-reactors: a pristine MR0001 on SiO_2 and another MR0002 on TiO_2 with a 100 nm thick TiO_2 layer sputter deposited on the reactor area. These were used as reference points for background noise in the catalytic reaction from the setup. The results showed that both µ-reactors exhibited very low activity towards CO oxidation at elevated temperatures, as shown by the black and grey lines in figure 4.1.

However, after several months of CO oxidation measurements on different µ-reactors, we retested the pristine µ-reactor MR0001 on SiO_2 and observed a much higher activity towards CO oxidation, as shown by the second grey line in figure 4.1.

It is highly unlikely that the µ-reactor was unintentionally switched with another reactor that had nanoparticles deposited on it. This is because considerable attention is given to carefully separating and organizing the µ-reactors after each use.

Root causes and contamination

To investigate the root cause of this unexpected activity, we considered the possibility of Ni contamination from carbonyls present in the CO gas feed. Ni contamination from carbonyls could increase the catalytic activity of CO oxidation reaction. The CO gas feed line is made of steel tubing and, to limit and avoid carbonyls in the gas feed, the pressure in the CO gas line is as low as possible but still above reaction pressures (P < 1.5 bar). However, if carbonyls are present in the gas feed, this would lead to deposition of nickel from carbonyls decomposing during the CO oxidation reaction at temperatures above 180°C (or at room temperature if the gas stream is saturated with $Ni(CO)_4$ and the pressure drops like on the other side of the MFC). Nickel is a known catalyst for CO oxidation and could explain the observed activity over time as more and more nickel would be deposited [70, 71].

To further limit the possibility of carbonyls and eliminate any potential source of nickel contamination that could be responsible for the increased activity, we installed a Cu-based carbonyl filter just before the mass flow controller on the CO line (Flow 6 on the microreactorNG setup), as shown in figure

2.8.

We then tested a new pristine μ-reactor MR0004 on SiO_2, which showed significantly higher activity, even reaching full conversion and depleting all the CO from the gas feed. We also tested another μ-reactor from an old batch from 2018, which showed the same activity. The shape of the measured CO2 signal was significantly different from previous pristine μ-reactors and Au deposited catalysts, as shown in figure 4.1.

The subsequent investigation aimed to identify the source of contamination causing the unexpected results. The stainless steel tubing leading out of the carbonyl filter and into the mass flow controller was not changed when the carbonyl filter was installed. To rule out the possibility of pre-carbonyl filter nickel deposited contaminating in this tubing the tubing was removed. A new pristine μ-reactor MR0006 was tested, which also showed high CO oxidation activity depleting the entire CO gas stream. For this to happen either the feared alleged Ni-contamination has spread like malicious fire ants in your summer house to the entire system or the contamination is less likely to come from the setup. In this case the next obvious place to investigate is the μ-reactor it self as the source of contamination. Either during a fabrication step or in the handling of the μ-reactor from the cleanroom and into the different equipment's at SurfCat.

One of the active pristine μ-reactor MR0004 was opened and examined with XPS and ISS at four different locations within the reactor area using the Thetaprobe equipment at SurfCat. Despite its high activity towards CO oxidation, XPS analysis revealed no evidence of platinum or other contaminants that could account for the observed activity, as shown in figure 4.3. Similarly, the ISS data, shown in figure 4.2, obtained with an energy of 1000 eV, only detected signals from silicon and oxygen, with no evidence of platinum as highlighted in the zoomed in inset of the figure.

If the contamination causing the high CO oxidation activity was located on the μ-reactor itself, it was hypothesized that depositing a layer of TiO_2 on the reactor area could suppress the activity. To test this idea, a μ-reactor MR0003 had 100 nm TiO_2 sputter deposited on the reactor area. The results showed that this μ-reactor had equivalent low CO oxidation activity as previously measured on empty μ-reactors with uniform TiO_2 sputtered on the reactor area, suggesting that the unexpected activity originates from the μ-reactor itself and that the deposited TiO_2 substrates cover the catalytic active material, suppressing the activity.

To further investigate the source of the contamination, a pristine μ-reactor MR0007 was tested in a different old microreactor-setup that had not been used in this project and had not been exposed to the carbonyl filter. The results confirmed that the high CO oxidation activity was not due to contamination from the setup or the newly installed carbonyl filter, but rather from the μ-reactor itself. This finding was supported by the highly reproducible nature

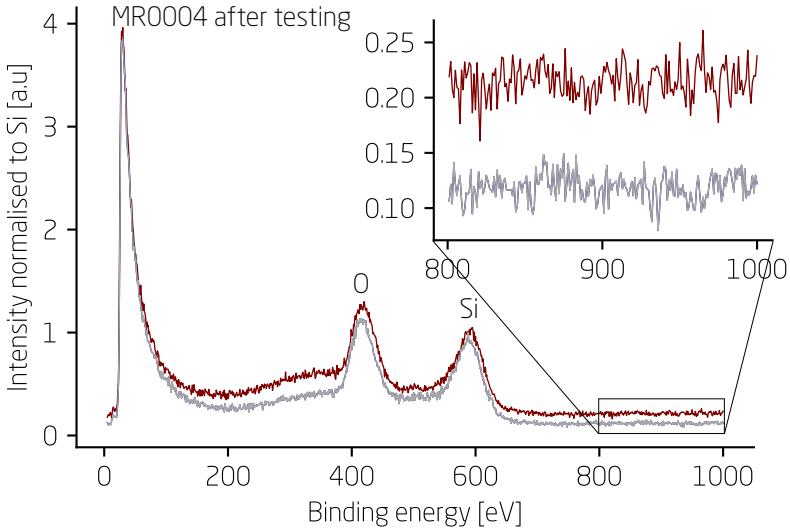

Figure 4.2: Two ISS survey scans were performed on the same µ-reactor (MR0004) at different locations after measurements in the microreactorNG setup. This µ-reactor, without a catalyst on the SiO_2 substrate, exhibited high catalytic performance towards CO oxidation, depleting the CO gas stream entirely. Surprisingly, only Si and O were detected on the surface from these scans. The CO oxidation activity may be attributed to extremely minute amounts of Pt-like metals not detectable by ISS, some sub-surface catalytically active material, or a source other than the µ-reactor. The surveys were conducted with He+ at 1 keV and normalized to the Si peak.

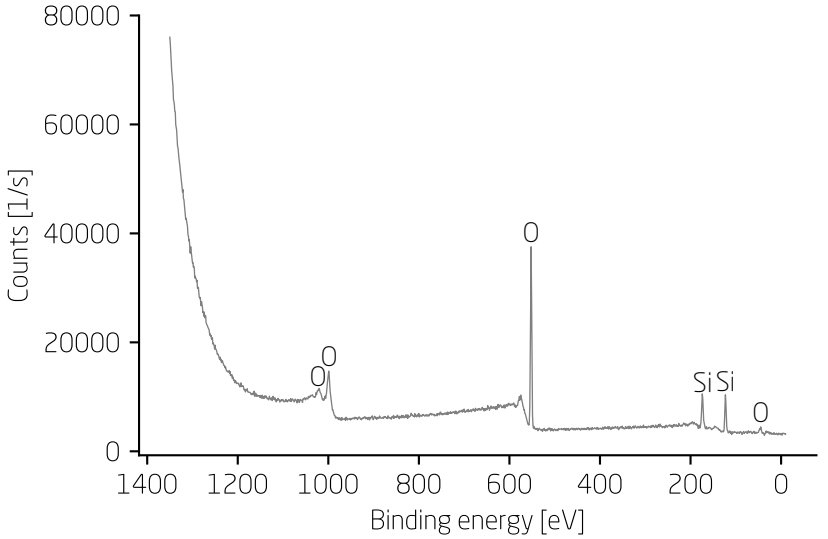

Figure 4.3: XPS survey scan of the pristine µ-reactor MR0004 without any catalyst deposited or new substrate deposited. This µ-reactor has shown high CO oxidation activities and this XPS survay scan shows no indication of any other elements than the expected silicon and oxygen to be found in a pristine µ-reactor.

of the unexpectedly high activity observed in the pristine µ-reactors, with five tested as received showing the same high CO oxidation activity. Only the first µ-reactor MR0001 tested at the beginning of the project showed low activity at elevated temperatures.

To investigate the type of contamination on the surface of the µ-reactors, an ISS depth profile was done using sputtering. The ISS was conducted at an energy of 1000 eV, and the He+ ions were sent with an angle of incident of 127°. Figure 4.4 presents the results, which display ISS data for different sputtering times.

At higher energies, two features can be observed in the ISS depth profile of the µ-reactors: a small peak at approximately 880 eV and a tiny bump at approximately 930 eV, which could correspond to platinum measured at 927.5 eV under the conditions of the measurement. However, the intensity of the platinum peak varies significantly among the different µ-reactors, suggesting a notable difference in the amount of contamination responsible for it. The first peak at 880 eV is consistent with Ba, which is a known contaminant traced back to the cleanroom fabrication and explained in earlier studies [29].

Olivia Fjord Sloth used Inductively Coupled Plasma Mass Spectrometry (ICP-MS) to investigate which elements were present on the surface of the µ-

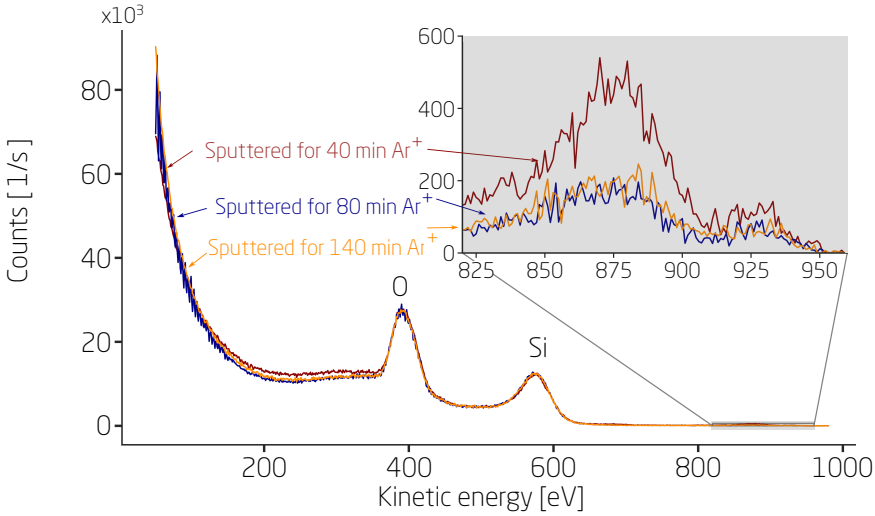

Figure 4.4: ISS data for different sputtering times on an catalytic active empty µ-reactor. Two unexpected features are observed in the ISS depth profile of the µreactors at higher energies: a small peak at approximately 880 eV and a tiny bump at approximately 930 eV, which could correspond to platinum measured at 927.5 eV under the conditions of the measurement.

reactors. The experiment involved placing a droplet of aqua regia (a mixture of HNO_3 and HCL) on the reactor area to dissolve any metals present. The procedure was to put a 20 µL droplet of aqua regia on the reactor area for a minimum of 15 and a maximum of 20 minutes, followed by diluting the solution with 9 mL of 18.2 MΩ·cm ultra pure water. This procedure was repeated on five different samples: the tested empty µ-reactor MR0004 and the empty µ-reactor MR00012 (which had been sputter cleaned with Ar+ for 40 minutes), two pristine µ-reactors received from the cleanroom, a pyrex lid, and a reference sample of pure aqua regia. The results of the ICP-MS measurement can be seen in figure 4.5.

The figure shows the apparent concentration of different elements in the samples. The pure aqua regia was used as a reference sample to determine the base level of each element.

Only elements that exhibited substantially different signals from the reference sample are displayed on the plot. The signals are adjusted using their respective sensitivity factors to convert them into an apparent concentration. However, a true concentration cannot be determined since it would require a standard that was not available at the time. Since only the relative difference to the reference sample was necessary to verify the presence of contaminants, an absolute amount quantification was unnecessary.

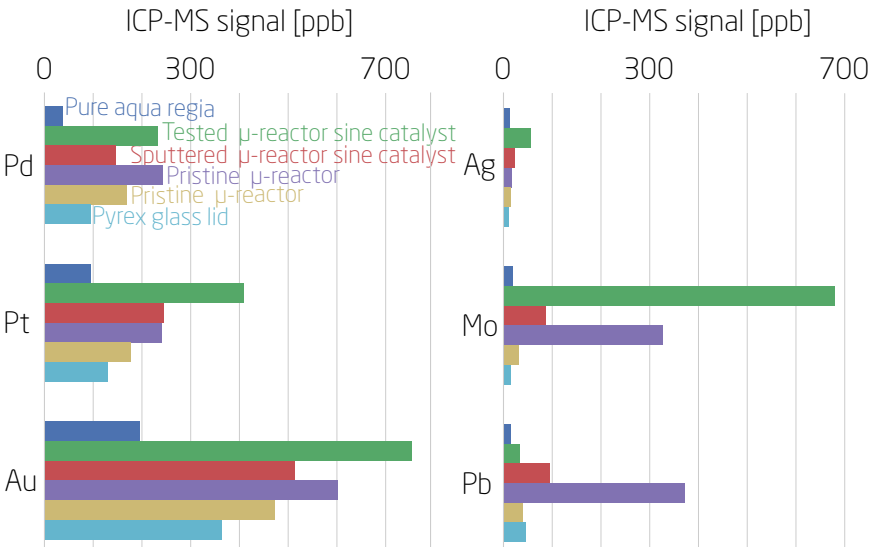

Figure 4.5: The figure shows the apparent concentration that has been converted from the ICP-MS signal. This signal was used for qualitative analysis of various samples in order to detect possible elements that may be contaminating the pristine µ-reactor and causing it to exhibit activity as a catalyst. Figure adapted from [72]

When analyzing the ICP-MS data, it is important to consider the base level represented by the pure aqua regia (shown in dark blue n figure 4.5). The sensitivity of ICP-MS is very high, which means that any contamination from the sputter chamber, the thetaprobe setup or the cluster source may also be detected. To ensure that any observed contamination is not due to these sources, a tested empty µ-reactor (shown in green) was previously analyzed using XPS and ISS, and an empty µ-reactor sputtered for 40 min in the cluster source (shown in red) was also included in the analysis. The two pristine samples (shown in purple and yellow) were obtained directly from the cleanroom, and pyrex glass was tested as well to confirm that there was no contamination from that source.

The ICP-MS data in figure 4.5 shows significant contamination from several elements, with palladium (Pd), platinum (Pt), and gold (Au) being particularly concerning. The molybdenum (Mo) signal may come from the thetaprobe chamber, as the sample holder can contain Mo, while the source of the lead (Pb) signal is unclear.

The presence of Pt contamination is particularly worrying since even very small amounts of Pt can be a highly effective catalyst for CO oxidation. This suggests that contamination from Pt on the µ-reactor surface could significantly affect the results of CO oxidation experiments [72, 73]. In conclu-

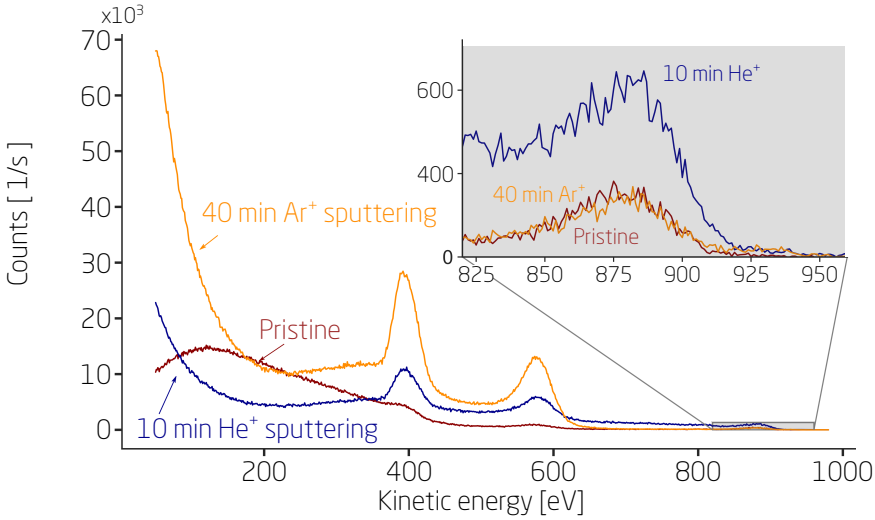

Figure 4.6: ISS depth profile of a pristine µ-reactor. Both He+ and Ar+ sputtering was performed with 1 keV by Karl Krøjer Toudahl.

sion, the ICP-MS analysis further confirms that the contamination is on the µ-reactor itself.

Annihilate activity from contaminants

To address contamination-induced activity in µ-reactors, various solutions were explored. A pristine µ-reactor with 50 nm TiO_2 deposited on the reactor area was tested and showed acceptable low activity only at high temperatures as seen following the orange line in figure 4.7. Attempts to cover the entire µ-reactor with TiO_2 failed due to anodic bonding issues, but a µ-reactor partially covered with TiO_2 was successfully sealed and showed no unexpected activity. This can be seen as the brown line in figure 4.7.

ISS spectra shown in figure 4.6 indicated that sputtering reduced the intensity of a peak around 880 eV related to the presence of Ba, and further reduction could be achieved by sputtering with Ar+ for 40 minutes, suggesting contamination may be reduced through sputtering.

Testing a µ-reactor rinsed with aqua regia showed the same high activity as the directly received µ-reactor shown as the turquoise line in figure 4.7.

It was considered whether the contamination originated from Pt diffusion from the RTD and heaters during the 24-hour annealing process, or from the furnace itself, which is where the µ-reactors are placed. One µ-reactor not annealed was tested, showing high activity for the first CO oxidation but at higher temperatures than other active empty µ-reactors, and significantly lower activity for the second CO oxidation run. There is no clear explanation as to why the second run exhibited lower activity compared to the first.

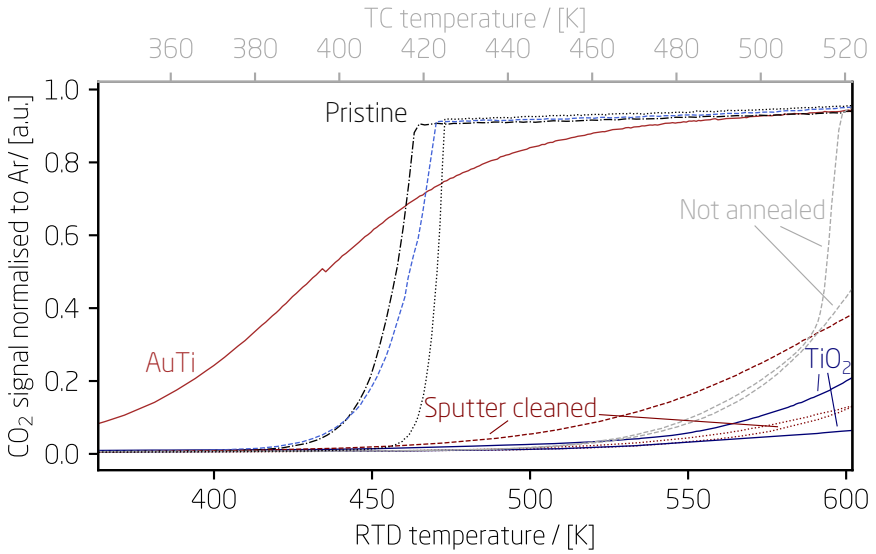

Figure 4.7: The CO_2 QMS signals normalised to Ar is plotted as a function of RTD-measured temperature on the bottom x-axis and TC-measured temperature in vacuum on the top x-axis. The red line labeled ”AuTi” represents a µ-reactor containing 2.5 nm AuTi catalyst with 5% coverage on a SiO_2 substrate. The black lines labeled ”Pristine” is pristine reactor received from the cleanroom fabrication with the dashed dotted line being a µ-reactor annealed in a new furnace. The dashed light blue coloured line is a pristine reactor that has been clean with aqua regia. The dashed and dotted red lines labeled ”Sputter cleaned” is 140 min and 40 min sputter cleaned µ-reactors, respectively. Finally, the dark blue line labeled ”TiO_2” corresponds to a pristine µ-reactor with a 50 nm TiO_2 thin film.

Lastly, changing the furnace used for annealing to a new one that was expected to be contamination-free did not remove the high activity observed in µ-reactors, as shown by the blue curve in figure 4.7.

Summary on "pristine" activity

Pristine and empty µ-reactors were found to be contaminated, possibly with Ba or platinum based on ISS and ICP-MS measurements. The contamination most likely have occurred during fabrication of the µ-reactors possibly due to diffusion during annealing. Aqua regia was unable to remove the contamination from the µ-reactors, despite the fact that it is known to dissolve metallic elements well. This IOs surprising since sputtering had a positive effect on reducing the level of contamination. Sputtering the µ-reactors was effective in reducing their activity, and covering them with a layer of TiO_2 also reduced the catalytic activity of pristine reactors. In figure 4.7, the activity is plotted against the temperature measured by the RTD on the bottom x-axis and the TC measured temperature on the top x-axis. The RTD data for the empty µ-reactor showed that the catalytic active µ-reactors starts being catalytic active above 420 K and reaches full conversion above 460 480 K, which is in the temperature window as expected for platinum group metals. The "onset" temperature for pristine µ-reactors is 50-100 degrees higher at 470 K to 550 K before starting to exhibit catalytic activity towards CO oxidation. Based on the data presented in figure 4.1, it can be observed that the AuTi nanoparticles exhibit CO oxidation activity at much lower temperatures than the contaminated and sputter-cleaned pristine µ-reactors. Therefore, if CO oxidation activity measurements is performed on Au-based catalysts in the µ-reactor at temperatures lower than those affected by contamination, the resulting data can be trusted to accurately reflect the catalytic activity of Au.

4.2 Issues with reproducible measurements of similar prepared µ-reactors

The work described in this section is carried out in collaboration with Olivia Fjord Sloth during her master's study. Several µ-reactors have been prepared for catalytic activity testing with various substrates and nanoparticle sizes. However, in some cases, seemingly similar µ-reactors exhibit significant differences in their catalytic CO oxidation activity. One of the reactors exhibit full conversion activity, converting the entire CO gas stream into CO_2, while the others show no activity at all. In order to establish the validity of experimental results, it is crucial to be able to reproduce the experiments consistently.

Reproducing the active samples has been challenging. For instance, the active 2.5 nm AuTi nanoparticles on SiO_2 µ-reactor has been attempted to be reproduced three times, but with no success as can be seen in figure 4.8. The inset in figure 4.8 presents the Au region of the ISS spectra, measured immediately after deposition for the four reactors, demonstrating no corre-

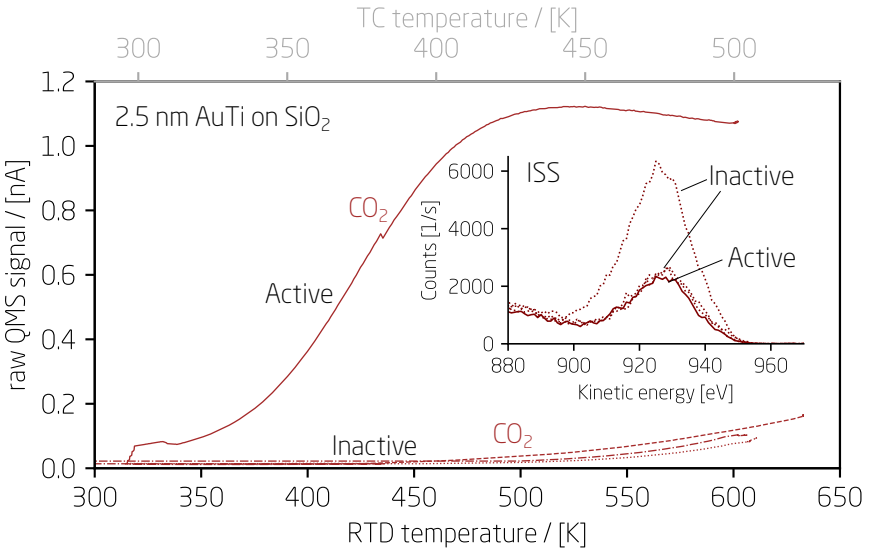

Figure 4.8: The figure shows the QMS signal for CO_2 as a function of temperature, with the TC measured temperature displayed on the top x-axis and the RTD measured temperature on the bottom x-axis. The data is obtained from four different 2.5 nm AuTi nanoparticles on SiO_2 µ-reactors. One µ-reactor is catalytic active and represented by a solid line, and the other three being inactive, represented by dotted lines. The discrepancy between the RTD measured temperature and the TC measured temperature relates to the low pressure in containment volume further described in 4.3. The inset display the zoom in of the ISS scans of the four µ-reactors post deposition but prior activity testing. It can be seen that no correlation to Au peak intensity and catalytic activity is found.

lation between CO oxidation activity and Au ISS intensity. It is unclear why some reactors are active and others are not. Some might argue that the active is the outlier, however, something causes the CO oxidation activity of the active µ-reactor. Given the practically identical deposition conditions and compositions determined from XPS, as shown in Table 4.1, it is surprising that the 2.5 nm nanoparticles exhibit varying Au ISS peak intensities and CO oxidation activities.

To determine what distinguishes active nanoparticles on the µ-reactors from inactive ones, four µ-reactors (two containing active nanoparticles and two containing inactive nanoparticles) with particle sizes of 2.5 nm and 4.5 nm were opened by cutting the Pyrex lid and removing it, exposing the reactor volume for ISS and XPS analysis. XPS and ISS survey scans were performed at three different points on each reactor seen in figure 4.9 and figure 4.10, respectively. The results showed a clear Au signal (Au4f and Au4d

Table 4.1: Deposition conditions for the 2.5 nm AuTi on SiO_2 µ-reactors shown in figure 4.8. Values given by former PhD student Niklas Secher.

	Active	Inactive	Inactive	Inactive
Ar flow [ml/min]	34	33	33	33
He flow [ml/min]	82	82	82	82
Magnetron power [W]	21	21	21	21
Aggregation zone pressure [mbar]	0.13	0.13	0.13	0.13
Substrate bias [V]	48	48	48	48

peaks) for the active reactors but not for the inactive reactors. No correlation was found between the measured catalytic activity and the intensity of the Au peak signal measured with ISS post deposition of AuTi nanoparticles and prior to bonding the µ-reactors as seen in figure 4.11.

The difference in catalytic activity between active and inactive samples seems to occur during the bonding process or during catalytic testing. One hypothesis suggests that TiO_2 creeps up the sides of the Au-core of the nanoparticles and encapsulates the catalytic active metal due to strong metal support interaction [68]. To test this hypothesis, an ISS depth profile was conducted to remove any thin layer of TiO_2 covering the Au-core of the AuTi nanoparticles. Catalytic active and inactive µ-reactors with 2.5 nm and 4.5 nm AuTi nanoparticles are shown in figure 4.12a, b, c, and d, respectively.

For the active 2.5 nm µ-reactor, the Au signal intensity increased with a very low Ar+ sputtering time. However, further sputtering was not performed as the reactor was dropped inside the cluster source deposition chamber. For the active 4.5 nm µ-reactor, the Au signal increased with sputtering time until a maximum Au peak intensity was reached after 20 minutes of sputtering, after which the intensity decayed. For the inactive µ-reactors, the intensities were much lower than the catalytic active µ-reactors. For the inactive 2.5 nm AuTi nanoparticles, the signal increased up to 30 minutes of sputtering, but further sputtering was not performed as the reactor was unfortunately also dropped in the chamber. For the 4.5 nm inactive AuTi nanoparticle, the Au signal increased until 20-40 minutes of sputtering, after which the intensity decreased. However, the large Au peak hypothesised for catalytic inactive reactors as layers were sputtered off was not observed.

One route to increase the reproducibility of similair prepared samples could be reducing the Ti concentration in the nanoparticles which may result in more Au to be exposed for catalysis. This can be achieved by utilizing a metal target with a different alloy composition, such as 80% Au and 20% Ti, or by implementing innovative cluster source designs with a multiple magnetron configuration to fine-tune the composition using two separate targets. A cluster source of this nature has recently been established at SurfCat. A multiple magnetron cluster sources provide the ability to fine tune and control the composition, which could be particularly interesting for the AuTi

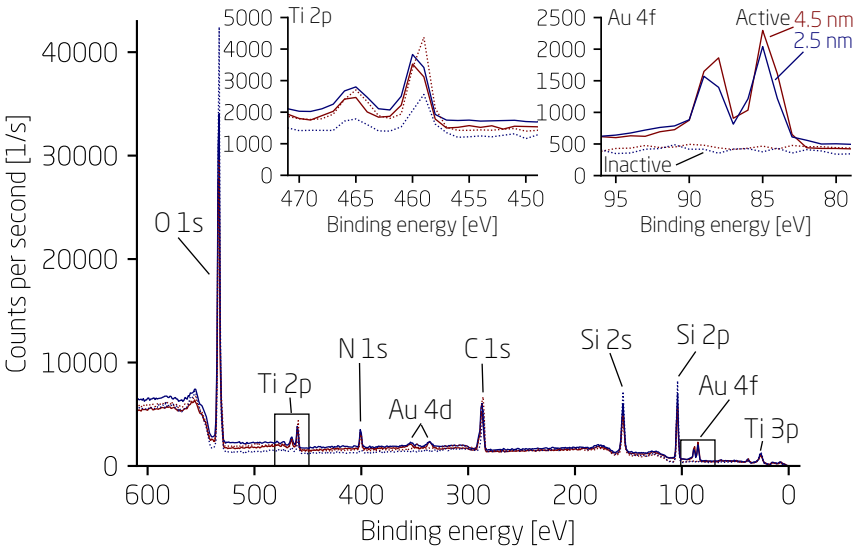

Figure 4.9: XPS scan of four different µ-reactors after catalytic activity testing. The red line represent 4.5 nm AuTi on SiO_2 and the blue line represent 2.5 nm AuTi on SiO_2. The solid lines indicate active catalysts, while the dashed lines indicate inactive catalysts.

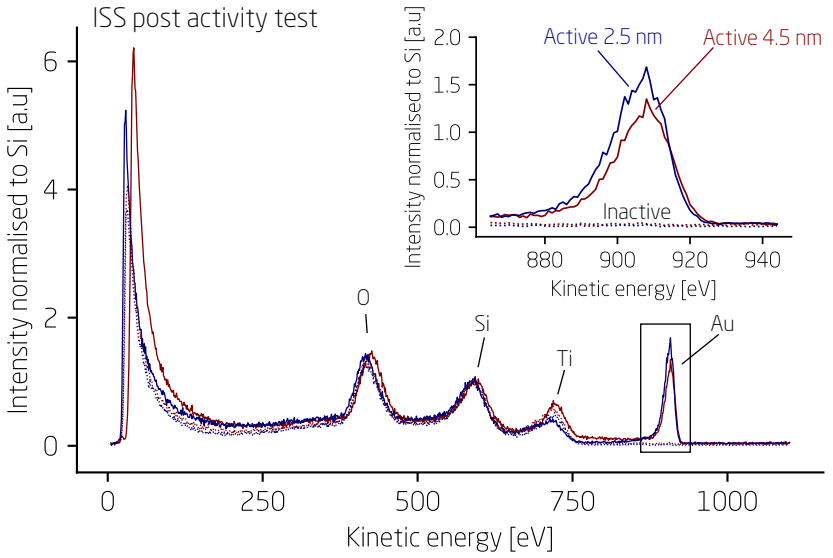

Figure 4.10: ISS scan of four different µ-reactors after catalytic activity testing. The red line represent 4.5 nm AuTi on SiO_2 and the blue line represent 2.5 nm AuTi on SiO_2. The solid lines indicate active catalysts, while the dashed lines indicate inactive catalysts.

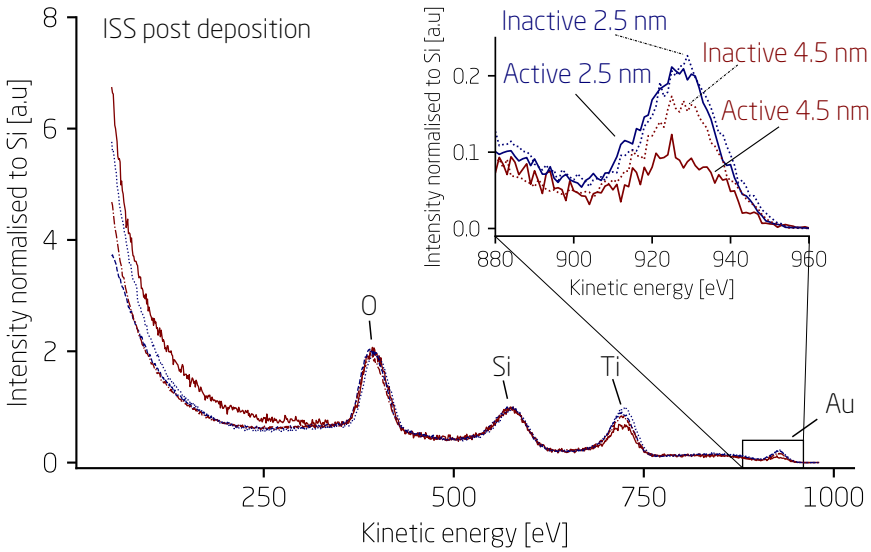

Figure 4.11: ISS scan of four different µ-reactors after deopistion and prior to catalytic activity testing. The red line represent 4.5 nm AuTi on SiO_2 and the blue line represent 2.5 nm AuTi on SiO_2. The solid lines indicate active catalysts, while the dashed lines indicate inactive catalysts.

project but also for other bimetallic system such as CoCu for direct ethanol synthesis.

A significant difference in Au signal has been found between active and inactive reactors post activity testing, which is inconsistent with the Au signal measured post deposition but prior to bonding and testing. One possible explanation is that AuTi nanoparticles sinter strongly, forming large islands that may be overlooked by characterization techniques due to their localized nature. Another explanation can be that the µ-reactors has cracks in the SiO_2 layer from the clean room and the the Au nanoparticles form an eutectikum with the underlying Si disappearing that way [74].

The best explanation where this sintering effect would take place is during the anodic bonding step. Here, parts of the reactor are reaching high temperatures above 350 degrees and even though the catalyst in the reactor area should be protected against high temperature with active cooling this seems still the most plausible place. This type of investigation is cumbersome due to the single use nature of the µ-reactors. When opening the reactor just to discover the nanoparticles are well dispersed and well defined, activity measurement is not possible since the reactor is broken up and the many hours of manufacturing and deposition and characterization are effectively lost. However, a µ-reactor with 5% coverage of 3.5 nm AuTi on a 50 nm TiO_2 substrate was prepared. SEM images of the µ-reactor with

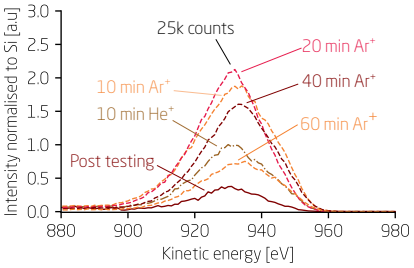

(a) ISS depth profile of 4.5 nm catalytic active AuTi nanoparticles

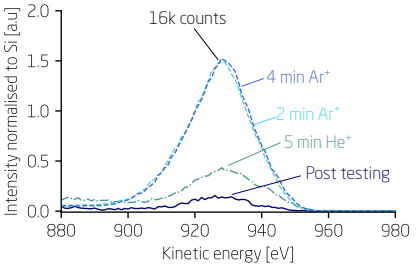

(b) ISS depth profile of 2.5 nm catalytic active AuTi nanoparticles

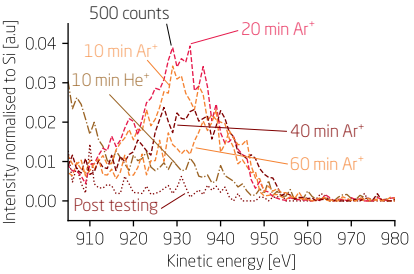

(c) ISS depth profile of 4.5 nm catalytic inactive AuTi nanoparticles

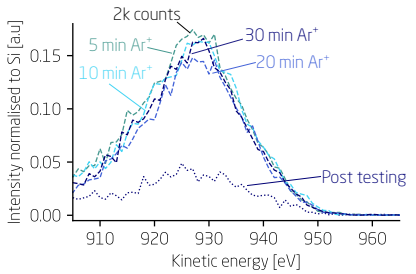

(d) ISS depth profile of 2.5 nm catalytic inactive AuTi nanoparticles

Figure 4.12: ISS depth profile of the Au peak for two active and two inactive µ-reactors with AuTi nanoparticles on SiO_2. a) and c) display the 4.5 nm active and inactive nanoparticles, respectively in the red colours. Meanwhile b) and c) display the 2.5 nm active and inactive nanoparticles, respectively in the blue colours.

well defined and well dispersed AuTi nanoparticles as deposited is seen in figure 4.13 where the nanoparticles are clearly visible.

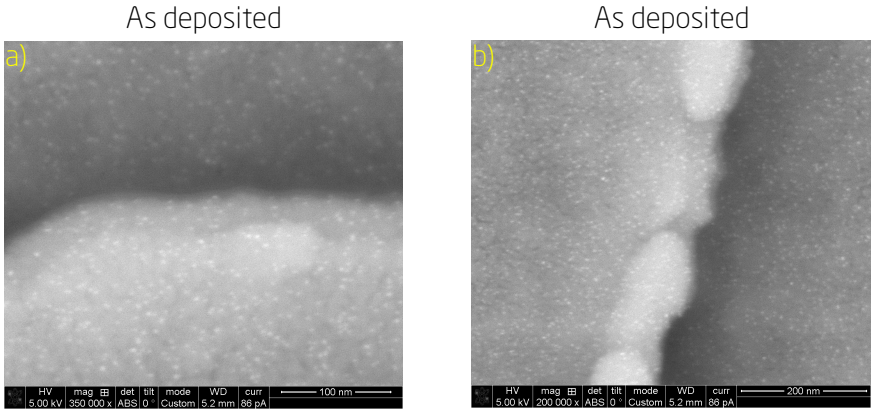

Figure 4.13: SEM images of a µ-reactor with 50 nm TiO_2 substrate and 5% coverage of 3.5 nm AuTi nanoparticles. Fig a and b are images as prepared 3.5 nm nanoparticles.

The anodic bonding step requires high temperature as well as high voltage across the sample. To investigate the impact from each step of the anodic bonding with SEM images the µ-reactor is first exposed solely to 1kV across the µ-reactor for 1 hour before a new set of SEM images is taken. Figure 4.14 display SEM images of the well dispersed nanoparticles not affected significantly from the voltage drop across the reactor. The µ-reactor is then solely exposed to 350° C in the anodic bonding setup with active cooling on the sensitive reactor area but without the 1kV voltage applied.

The SEM images can be seen in figure 4.15. While the particles seems to have grown bigger they are clearly still nanoparticles. The anodic bonding setup does not seem to hold the complete explanation as to why some reactors are active and some are not. However, it is very user dependent. To mitigate the user dependency, hardware and software has been installed to be able to digitally control the power input and automatically monitor the temperature multiple places as described in 2.1.2.

Discussion on reproducible data

The reproducibility of catalytic results is not a unique problem to AuTi-bimetallic system. The underlying mechanism has been more extensively investigated with the AuTi system than prior systems such as NiFe; CoCu; Pt single atoms, dimers, and trimers; and dropcasted industrial catalysts. The inves-

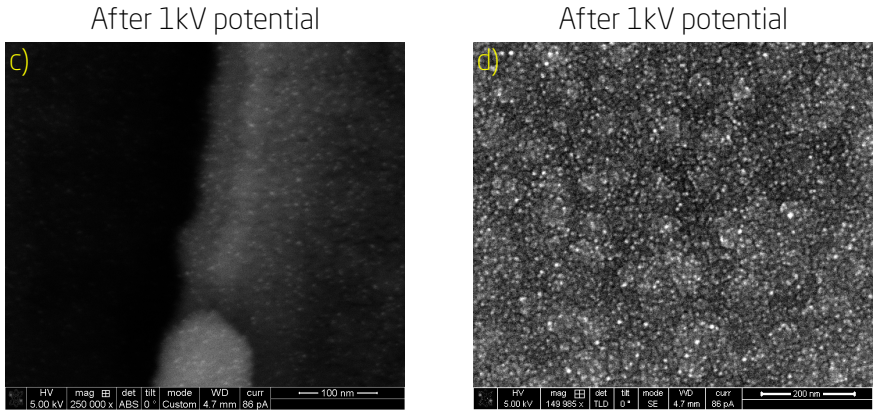

Figure 4.14: SEM images of the same µ-reactor with 50 nm TiO_2 substrate and 5% coverage of 3.5 nm AuTi nanoparticles seen in fig 4.13, after applying only voltage during the anodic bonding. Fig c and d are SEM images after applying 1kV to the sample for 1 hour.

tigations of possible issues with the system can be applied to other system in the future. The reproducibility of catalytic results with AuTi bimetallic alloy nanoparticles poses a significant challenge. Despite similar preparation processes, these nanoparticles display varied behaviors - some being very catalytically active towards CO oxidation, while others remain inactive.

XPS analysis revealed that catalytically inactive nanoparticles exhibited lower Au signals post testing. Hence, the Au either somehow disappears from the inactive samples or is never proper deposited as nanoparticles on the µ-reactors.

Intense investigation has been directed towards identifying the root cause of this problem. One considered factor was the manufacturing of the µ-reactor, especially in the uniformity of the growth of the passivating SiO_2 layer which could leave holes for Au to disappear through when sintering happens. However, no changes was made in the manufacturing process and SEM images reveal identical looking reactors. The issue could originate from the production and deposition of the AuTi nanoparticles on the µ-reactor. However, similar prepared µ-reactors have been observed to contain the expected nanoparticles, consolidating the validity of the deposition procedure from the omicron cluster source.

The Au must then disappear from the samples after being proper deposited. The Au could have clustered into larger localized particles hiding from XPS

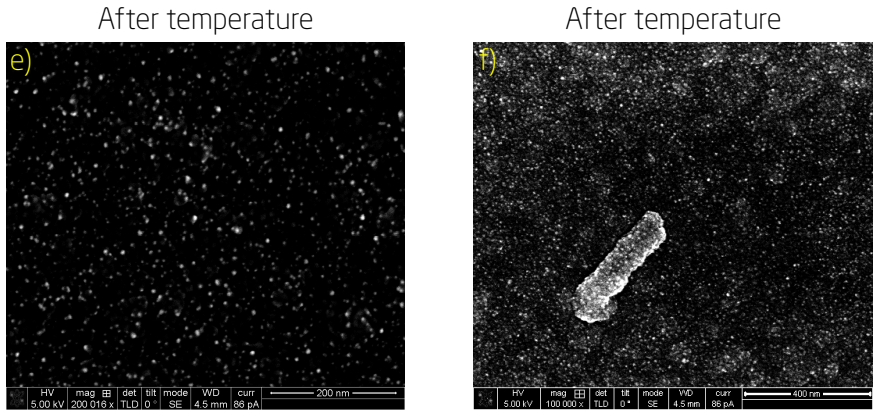

Figure 4.15: SEM images of the same µ-reactor with 50 nm TiO_2 substrate and 5% coverage of 3.5 nm AuTi nanoparticles seen in fig 4.13 and 4.14 after applying only temperature during the anodic bonding. Fig e and f are SEM images after applying 350 degrees temperature and active 10 degrees cooling on the sensitive reactor area.

and ISS signals but would be then be visible in SEM. Additionally, the active Au core of the AuTi catalyst might be covered by TiO_2, making the nanoparticles catalytically inactive.

Furthermore, the storage conditions of the prepared µ-reactors were investigated. While the nanoparticles are deposited on the µ-reactors during the same week the testing of the µ-reactors can be up to weeks per reactor. During this time the AuTi could sinter into large catalytic inactive nanoparticles. Or the oxygen could react with Ti creeping up on the Au-core creating a passivating TiO_2 layer on top of the catalytic active Au-core. The storage of the µ-reactors in the omicron vacuum chamber was in close proximity to a hot-filament gauge which could vapor of small amounts of gunk which could deposit on the µ-reactors blocking the catalytic active core. No XPS data reveal any gunk and SEM images showed no sign of degradation of the nanoparticles being well dispersed and small even after weeks of storage.

The issue could also be related to the size of the nanoparticles, which were observed to be considerably larger post catalytic activity testing. This suggests that sintering effects have taken place. This can be during the catalytic testing or the anodic bonding process where particles experience elevated temperatures. Since Au catalysts lose activity when increasing above 5 nm in size, this could be a plausible cause of the observed inactivity.

Efforts to achieve reliable catalytic activity in AuTi nanoparticles continue, with the anodic bonding process being the central concern for reproducibility, likely causing inconsistencies in the fundamental nanoparticles tested. Measures such as improved temperature monitoring and power control during anodic bonding have been implemented to reduce user dependent operation.

Extensive time requirement

The primary barrier in examining the reproducibility issue is the considerable time taken for observation and analysis. In this case, it spanned over ten months from the initial catalytic test results to the first identification of reproducibility issues.

Several elements has the potential to influence on catalytic activities, such as nanoparticle size, various support substrates used, and different catalysts deposited.

Initial tests focused on the catalytic stability of AuTi nanoparticles in comparison to Au nanoparticles. The differences in catalytic activity could be attributed to variations in the active Au-core size. Thus, a size study, ranging from 2.5 nm to 7.5 nm, was introduced to the research to reveal differences based on nanoparticle dimensions and to compare the stability of more similar catalysts. Later research involved analyzing stability on different substrates, as Au nanoparticles are known to be poor catalysts on SiO_2 substrates, prompting the exploration of alternative substrates like TiO_2.

Each different test is expected to yield various catalytic activities.

After ruling out all these factors as the cause of discrepancies in activity, rigorous testing and analysis begin to determine the reason behind the inability to reproduce catalytic activities.

A significant challenge is the extensive time required to investigate reproducibility issues thoroughly. Numerous identical µ-reactors, similair in support substrate, catalytic material composition, and nanoparticle size, are essential for this investigation. Limited time for nanoparticle deposition and the time interval between nanoparticle deposition and catalytic testing of the reactors further complicate the issue. These factors introduce multiple stages where problems might occur, requiring a multitude of tests. Ultimately, achieving a sufficient number of reactors that are successfully manufactured, deposited, bonded, tested, opened, and characterized is necessary. Each step in this process is time-consuming, and some, like the anodic bonding process, are more likely to damage the reactors, necessitating a repetition of the entire process.

The fundamental cause of unreliability in µ-reactors has not been clearly identified yet. Several factors contribute to this issue, including inconsistent µ-reactor supply, due to changing personnel in the cleanroom where the µ-reactors are manufactured, and varying yields. Additionally, there are challenges related to the preparation of samples from the cluster source, such

as the time it takes to switch between different targets and the AuTi target for sample preparation. These complexities make it difficult to pinpoint the exact sources of reproducibility issues in the microreactors.

To avoid the anodic bonding step a new re-useable design for the μ-reactor-platform has been conceptualised for thermal catalysis and a working prototype has been manufactured for photocatalytic testing. This will be discussed in the following section 4.5.

Until a new μ-reactor platform design for thermal catalysis has been tested and validated, every new catalytic system should be meticulously evaluated for reproducibility as a starting point.

This entails the comprehensive characterization and testing of multiple similarly prepared samples across various manufactured μ-reactors.

Due to the necessity for detailed characterization to guarantee the accuracy and reliability of the catalytic system, the evaluation process becomes quite time-consuming for each new catalytic system. Consequently, the μ-reactor becomes less effective as a tool for quick experimentation and testing of new catalysts, deviating from its original intent for rapid and efficient assessments.

4.3 Issues with temperature measurements in vacuum

In thermal catalysis the reaction rate is determined exponentially by the temperature, making it essential to measure and determine the correct temperature to identify the temperature range at which the catalyst is active.

The heater's power on the rear side of the μ-reactors is regulated by a feedback loop, which relies on either the resistance temperature detector (RTD) or a thermocouple (TC) placed atop the Pyrex lid. These sensors influence the PID programming values, with the RTD-measured temperature typically serving as the preferred feedback. However, not all μ-reactors can establish a reliable connection to the RTD, often due to scratches on the platinum or short circuits caused by the pogopins making contact with the steel chamber. In such cases, a repair of the mounting block or a complete new mounting block is required, and the TC is utilized as the feedback temperature.

Four distinct temperature experiments were conducted to determine the most accurate method for measuring the catalyst's temperature within the μ-reactor volume. The first and second experiments involved evacuating the containment volume, leaving the TC in a vacuum; however, in the second experiment, the TC was isolated with glass wool. The third experiment exposed the containment volume to air at atmospheric pressure, while the fourth filled the containment volume with argon gas at pressures ranging from 5 to 950 mbar. In all cases, the PID feedback temperature was based

on the RTD-measured temperature. The results of these four experiments are illustrated in Figure 4.16.

The results indicate that, in all four cases, the TC measures a lower temperature than the RTD. In vacuum, the discrepancy between the TC and RTD measurements is significantly larger, exceeding 100 K. Moreover, the difference is not constant and increases at higher temperatures. The discrepancy is smaller when a gas atmosphere surrounds the µ-reactor and TC. The difference ranges from 10-20 K at 525 K, or approximately 2-4%, with the smallest discrepancy observed in air. One issue with air surrounding the µ-reactor is air leakage into the QMS through the Viton O-rings, and an active argon flush over the O-rings is needed. This process cools the top of the µ-reactor where the TC is located and this effect should be taken into account when operating the system. When using argon in the containment volume, another concern arises due to the lid sealing the containment volume, which has a glass window for visual inspection during experiments. The heating of the gas could potentially cause localized heat buildup, leading to cracks in the glass section of the lid.

The thermal conductivity of the air gap between the TC soldering and the Pyrex lid is proportional to pressure, which could explain the significant temperature discrepancy observed in vacuum compared to a gas atmosphere down to 10 mbar [40]. Conversely, the RTD should not be affected by pressure since thermal conductivity is dominated by phonons. As a result, it is plausible that the RTD provides a more accurate measurement of the actual temperature within the reactor volume. Regrettably, the RTD loses connection in approximately 10-20% of the measurements, even though this issue has been mitigated by a former postdoctoral researcher at DanChip, Hoà Lê Thanh, who increased the annealing time from 3 hours to 24 hours during production. This adjustment resulted in more stable platinum thin films. Nonetheless, this improvement does not address the loss of connection due to pogopins short-circuiting or malfunctioning springs caused by heat stress.

To further assess the reliability of RTD-measured temperature in vacuum, a third indirect temperature measurement is conducted. This measurement is performed indirectly by monitoring changes in gas flow through the capillary within the µ-reactor using an MKS220d Baratron. By employing the capillary equation described in section 2.2.2, we can estimate a temperature based on the measured flux and compare it to a calculated flux at a given temperature T. By solving

$$\dot{n}(\eta, \mathsf{T}_{eff})_{calculated} = \dot{n}_{measured}, \tag{4.1}$$

for T the effective temperature of the capillary T_{eff} can be calculated.

As an initial estimate for the effective temperature T, one can begin by employing the following equation:

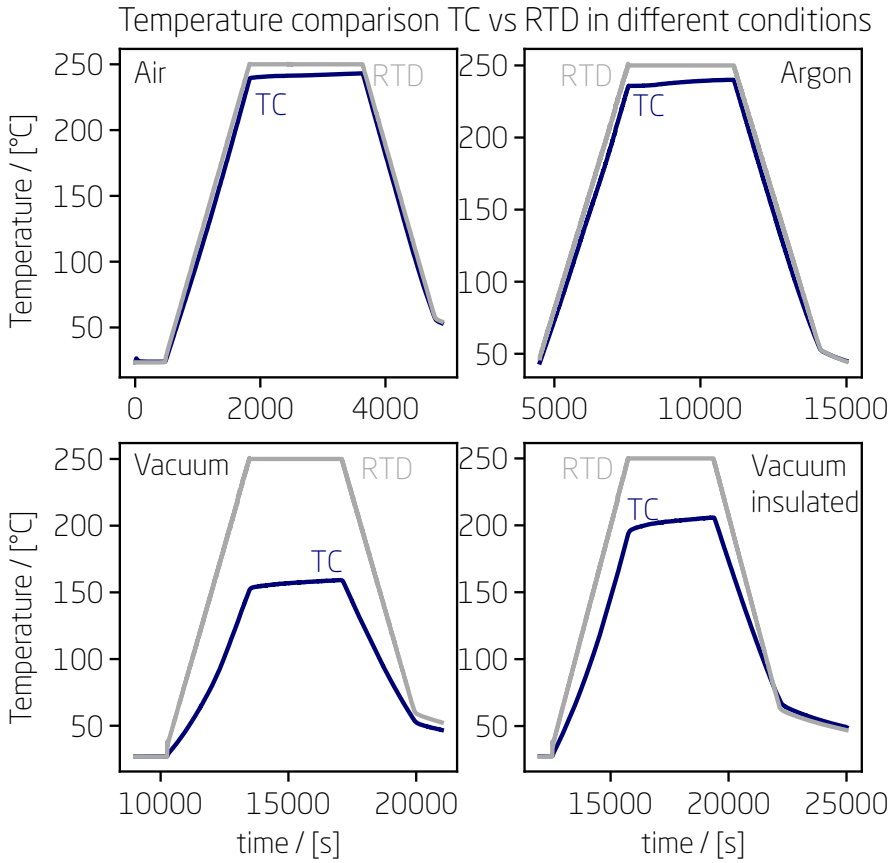

Figure 4.16: Discrepancies in TC temperature measurement and RTD temperature measurement in the μ-reactor setup with different gas mixtures and pressures around the μ-reactor in the containment volume. Air is complete open containment volume to air at atmospheric pressure. Argon is pure 6.0 equivalent Ar gas from AirLiquid ranging from 10mbar to 950 mbar of pressure in the containment volumen. Vacuum is evacuted containment volume after flushing with pure 6.0 Ar from AirLiquid twice. The insulated experiment refers to glass wool wrapped around the k-type thermocouple on top of the μ-reactor insulating from vacuum. As can be seen from these Figures the TC and RTD yield huge discrepancy in temperature measurement when experiments are done in vacuum. The discrepancy decreases significantly when exposing the surrounding atmosphere to different gas mixtures from 5mbar and up to atmospheric pressure.

$$T_{eff} = \frac{\dot{n}(\eta, T_{input})_{calculated}}{\dot{n}_{measured}} \cdot T_{input}, \tag{4.2}$$

Where T_{eff} represents the effective temperature of the capillary, T_{input} is initially the temperature measured by the RTD or TC, and $\dot{n}(\eta, T_{input})_{calculated}$ denotes the calculated flux for the given gas at a given temperature, and $\dot{n}_{measured}$ refers to the measured flux derived from the pressure increase detected by the Baratron. The effective temperature is determined by iteratively applying equation 4.2 taking T_{eff} as the new input T_{input} until T_{eff} converges to it self.

The experiment is illustrated in Figure 4.17 and Figure B.2 and summarized in table B.1. The experiment was conducted with an evacuated containment volume and 1 bar of CO_2 in the reactor volume. The temperature was controlled using a feedback loop from the RTD up to 100 °C, and the TC controlled the temperature from 100 °C to 250 °C as measured by the TC. Detailed plots showcasing the temperature profile, pressure profile, and QMS signals can be found in Appendix B.

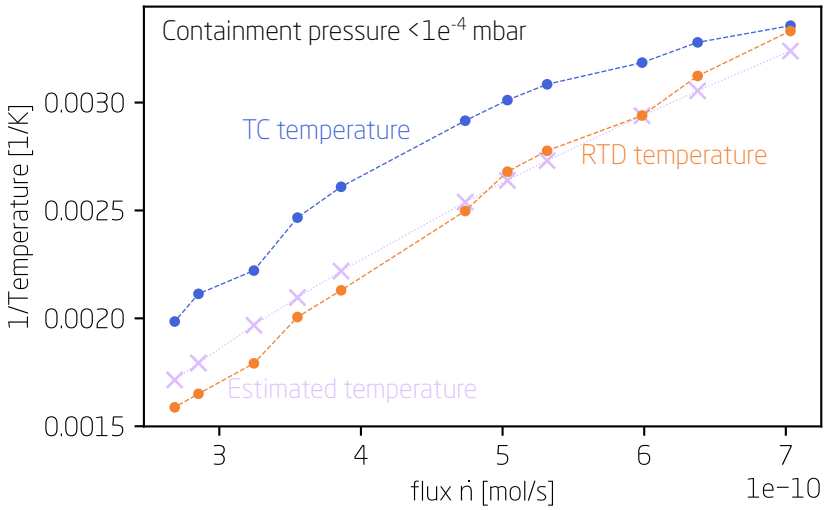

Figure 4.17: The graph presents the temperature measured by the thermocouple (TC, blue line) and the resistance temperature detector (RTD, orange line), along with the estimated temperature (Lavender line) as a function of the measured flux through the capillary, obtained from the pressure increase on the backside measured with the Baratron. The temperature recorded by the RTD aligns more closely with the expected temperature derived from the measured flux compared to the temperature measured by the TC.

As seen in Figure 4.17, the estimated temperature derived from the flux

calculation shows good agreement with the RTD-measured temperature, deviating only at higher temperatures where the estimated value falls below the RTD measurement. This discrepancy could be attributed to O-ring leaks or, more likely, to lower temperatures at the reactor's end, where the capillary is located, compared to the center of the two heater elements. The temperature profile across the μ-reactor, as seen in Figure 2.10, supports this explanation.

In conclusion, the RTD is more reliable and provides a measurement closer to the true temperature within the reactor volume compared to the TC in vacuum. This means that the RTD-measured value should be trusted when conducting experiments with an evacuated containment volume and the μ-reactor is in vacuum.

4.4 Improvements to be considered

In this section different routes to increase the versatility and usability of the μ-reactor platform will be discussed.

4.4.1 Backspacer production limitations

The μ-reactor has a Pyrex glass acting as a backspacer between the back of the μ-reactor and the viton O-rings in the mounting block. The mounting block shown in Figure 2.9 and as a schematic in Figures B.1 is made from stainless steel, which has a low thermal conductivity of 25 (W m^{-1} K^{-1}) at 20°C and 1 bar [75]. This low thermal conductivity makes the mounting block an effective heat sink. The backspacer was introduced to account for the theoretical heat loss to the mounting block, which acts as a heat sink. Additionally, it provides protection for the O-rings against extreme heat. However, the temperatures used for methanol synthesis or CO oxidation in this thesis are lower than the maximum temperatures that the O-rings can withstand.

There has been several wafers with faulty μ-reactors due to the fabrication step involving anodic bonding the pyrex back spacer on to the μ-reactors. This can be seen in figure 4.18 where the backspacer is faulty bonded or in figure 4.19 where the backspacer is misaligned during the bonding process. Both cases yield poor μ-reactor-to-wafer output and the μ-reactors are not usable.

To assess the heat sink effect from the mounting block, an infrared camera is used to capture images of the heated reactor and evaluate the heat distribution across the μ-reactor. A FLIR E60 infrared camera from FLIR Systems AB was employed to obtain images of the μ-reactor with and without a bonded backspacer, as well as the fully bonded reactor. The images were converted to grayscale for analyzing the heat distribution across the μ-reactor using the ImageJ software. The elevated temperatures of the μ-reactors, both with and without a bonded Pyrex backspacer, were controlled using similar power input and measured using a K-type thermocouple.

Figure 4.18: Image of a faulty bonded back spacer on a µ-reactor.

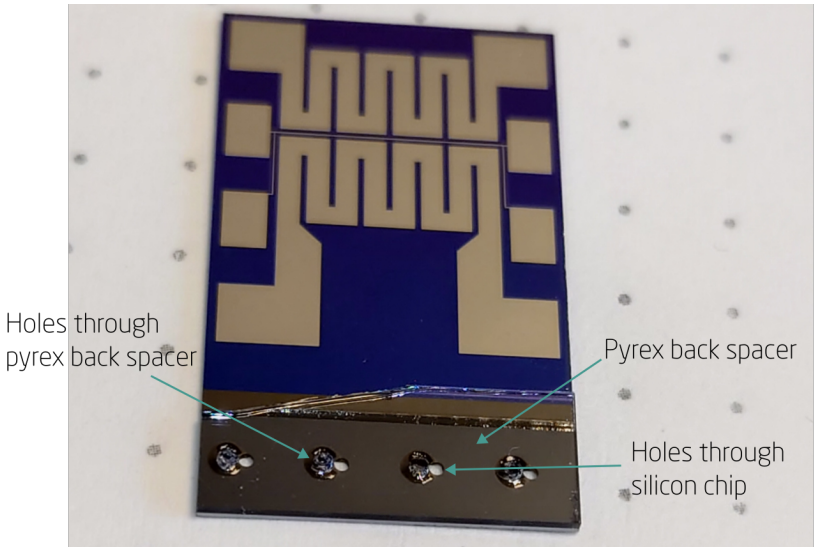

Figure 4.19: Image of a misaligned bonded back spacer on a µ-reactor.

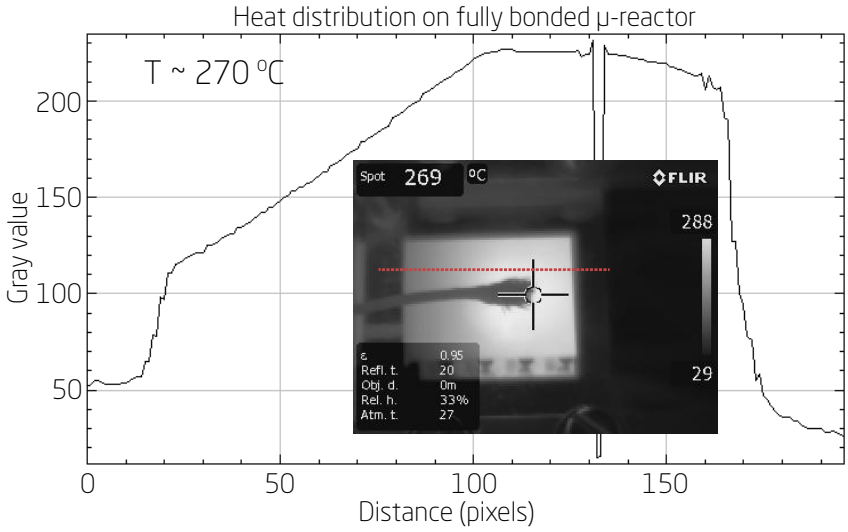

Figure 4.20: Infrared image taken with an infrared camera and analysed with imageJ for gray scale distribution plot along the red dotted line

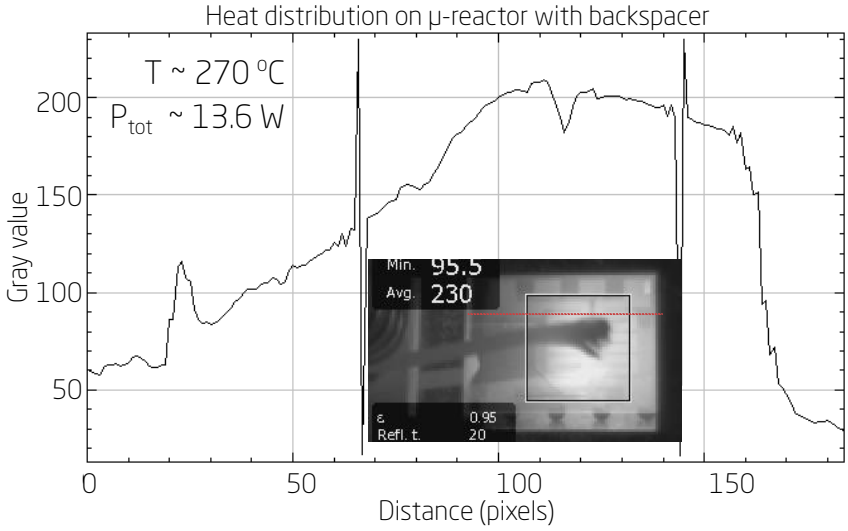

Figure 4.21: Infrared image taken with an infrared camera and analysed with imageJ for gray scale distribution plot along the red dotted line

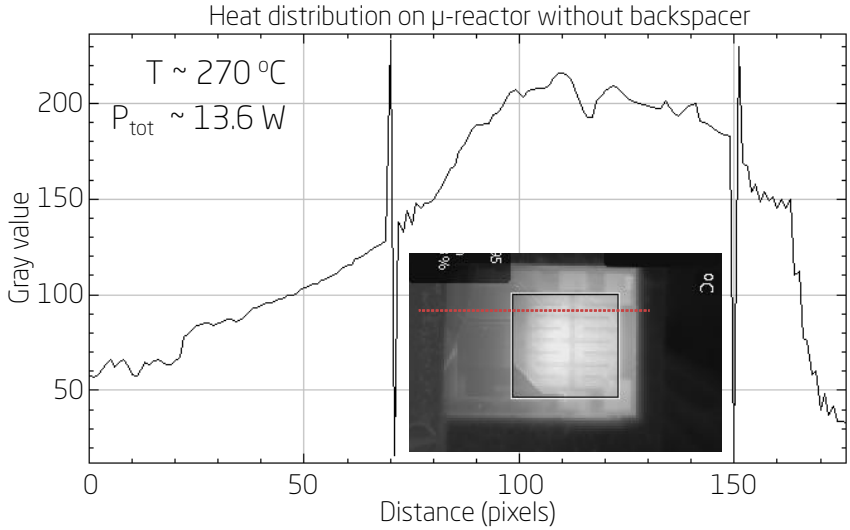

Figure 4.22: Infrared image taken with an infrared camera and analysed with imageJ for gray scale distribution plot along the red dotted line

The heat distribution of the three cases, can be seen in Figures 4.20, 4.21, and 4.22, accompanied by the corresponding images captured.

As observed from the figures, the temperature profiles exhibit similar patterns. The grayscale analysis using ImageJ reveals that for simpler production of the µ-reactor, the backspacer can be omitted when testing catalysts for low-temperature catalytic reactions. However, if the reaction temperature needs to exceed the limits that the O-rings can withstand, the backspacer can be anodically bonded during the fabrication process for that specific batch, serving as protection for the o-rings.

4.5 Rethinking µ-reactor design for Thermal and Photocatalytic Experiments

As described in section 2.1 SurfCat has investigated and analysed catalytic reactions with reactors in the micrometer dimensions [9, 35, 76, 77, 78]. To recap, these µ-reactors have minimized reaction volumes, leading to swift time responses and heightened sensitivity in measurements. The fundamental µ-reactor designs comprise a silicon base and a borosilicate pyrex top [9, 76].

The µ-reactor is then hermetically sealed by anodic bonding the pyrex top lid to the SiO_2-based µ-reactor [79]. The compact reaction volume, alongside the QMS's regulated capillary flow, allows for high time resolutions and sensitivities. This facilitates transient activity observations in thermal catalysts,

Figure 4.23: µ-reactor with an incomplete bonding on the inlet gas side.

photocatalysts, and exploration of low catalyst loadings.

Despite the many advantages, the potential of the µ-reactor platform to perform in surface catalysis research faced difficulties with respect to reproduceability in certain catalytic systems.

As discussed in section 4.2, inconsistencies were observed with Au and AuTi on SiO_2 and TiO_2 substrate. The inconsistencies in these measurements are not fully understood but are mainly ascribed to changes in the model system during the anodic bonding step which alters the morphology or composition of the catalyst. Such changes result in differences between the catalyst intended for testing and the one actually being tested.

As discussed in section 2.1.2 another aspect of the platform's reliability is the yield of successfully anodically bonded reactors. At times, the success rate can dip as low as 50% with different faulty bondings. Every time a prepared microreactor is un-successfully bonded many hours of work is wasted and the demand for more µ-reactors increases, demand for more costly catalyst increases, and the time investment increases. In figure 4.23 shows one such example of a µ-reactor which failed to bond. After multiple anodic bonding attempts there continues to be a gap in the side of the inlet fas channel.

Additionally, as outlined in section 4.4, the cleanroom fabrication process of the µ-reactor frequently results in a diminished yield of reactors. This decrease can be ascribed to three primary production challenges: issues arising during the RTD manufacturing step, malfunctioning during the an-

odic bonding of the pyrex backspacer, and cracks across the wafer. The complications associated with anodic bonding of the backspacer are illustrated in section 4.4 in figures 4.18 and 4.19.

Lastly, the current design of the platform allows for surface analysis of the catalyst after catalyst deposition but prior to anodic bonding, and after final testing. Critically, this approach lacks the capability to analyze the catalyst directly, immediately before testing, which is necessary for comprehensive understanding of the catalyst being tested. Additionally, while both pre-bonding and post final testing analyses are beneficial, they do not fully capture the dynamic changes the catalyst might undergo under different testing conditions. The ideal would be to monitor and analyze the catalyst continuously, allowing for adjustments between different testing conditions, rather than being limited to only after complete testing insights.

Inspiration from the EC-MS sniffer chip-design:

In this context, the paradigm of the microchip interface for electrochemical mass spectrometry (EC-MS) emerges as a beacon of potential evolution [42]. This microchip, connected to the mass spectrometer through a capillary, maintains a low response time and a low detection threshold, allowing in-depth analysis in hydrogen and oxygen evolution, as well as CO reduction [80, 81, 82, 83, 84]. In this reactor design, the seal is obtained without high temperature anodic bonding.

By eliminating the need for anodic bonding, there is a higher likelihood of testing the catalyst in its expected deposited state, regardless of the deposition manner (mass-selected clusersource or by dropcasting). What amplifies the dream of such a re-usable reactor is its capacity to allow analysis of the catalyst in between changes in the reaction condition. This feature provides a more detailed view into the changes in the morphology of the catalyst and also permits iterative testing of different reaction conditions on a single catalyst sample.

In summary, harnessing the principles of the microchip interface for EC-MS to develop a next-generation re-usable µ-reactor could provide answers to current challenges in the system, pushing forward the boundaries of the µ-reactor-platform for catalysis research.

4.5.1 EC-MS microchip platform for thermal catalysis testing

This section breaks down the work I have done during my PhD when developing the design for using the EC-MS interface block for thermal catalysis testing.

A schematics of a potential interface block for the EC-MS chip for thermal catalysis testing can be seen in figure 4.24

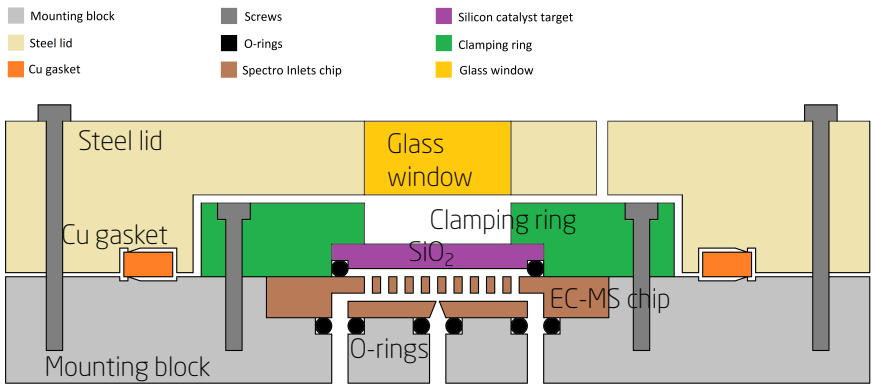

Figure 4.24: A schematics of an interface block envisioned for utilising a EC-MS re-usable µ-reactor chip for thermal catalysis testing.

The new model builds on the original design, where the chip is settled into an interface block and held by a clamping ring. Notably, this clamping ring now includes a slot for a thin SiO_2 disc, perfect for applying a catalyst. The SiO_2 disc is sealed to the top of the EC-MS chip using o-rings, as seen in Figure 4.24.

The goal is to keep a steady pressure of around 1 bar between the SiO_2 disc and EC-MS chip, while evacuating the surrounding atmosphere. This ensures that the reaction space is kept free from unwanted gases like oxygen. There is also a window in the center of the steel cover, making it possible to heat the SiO_2 disc with either a laser or a lamp. If initial tests of this system show potential, in the future an RTD with heater elements could be incorporated in a clean room fabrication on the SiO_2 disc.

Dealing with High Temperatures:

The primary concern with this particular design is to secure seal under elevated temperatures during thermal catalysis testing. SiO_2 wafers are prone to fracture under uneven compression, rendering Cu-gaskets inappropriate. Alternatives to Cu-gaskets could be Au-gaskets. The idea of using a thin gold thread, is utilizing the soft nature of gold, to have an effective vacuum seal to the surroundings that is temperature resistant. However, Au is costly and potentially catalytic active. O-rings appear more promising however, thermal limitations of the o-rings could introduce experimental anomalies from gas leaking through the o-rings. Certain variants of Kalrez® perflouroelastomer o-rings, which can withstand temperatures up to 325°C, may present a viable solution.

Furthermore, the smallest thickness of o-rings approximates 1mm. Given the requirement for a minimal interfacing gap between the chip and the SiO_2

disc (ideally in the vicinity of 100 µm), modifications to the design of the EC-MS chip or the SiO_2 disc including a narrow groove to place the o-ring in would be needed to limit the active reactor volume.

How Long Does Gas Exchange Take?:

A reasonable question arises, whether such a redesign would continue to allow for measurements on catalytic activity. To address this question, one can compare the geometric chip volumes, gas flow rate, and catalyst loading.

The EC-MS chip has an internal volume V_0 = 100 nL [42]. There is also some extra space between the chip and the SiO_2 disc (as shown in figure 4.24). To determine the total volume where the gas is, we add these two spaces:

$$V(h) = V_0 + \pi h R_{\text{disc}}^2 \tag{4.3}$$

Here, R_{disc} (the radius of the SiO_2 disc) is 2.5mm, given by the size of the EC-MS chip membrane. The total volume of the reactor is dependent of the height caused by the squeezed o-rings. Estimating the height $h = 800$ µm from an o-ring of 1mm thick and compressed up to 20%. If changes can be made, the height could possibly be reduced to around 100 µm by introducing a recess in the SiO_2 disc to accommodate partially the o-rings.

To find out the time duration, t_{exchange}, required for the entire gas to be replaced in the reactor volume, we must evaluate the volume in relation to the gas flow rate N_{cap}. The specified flow rate through the capillary in the EC-MS chip averages at 1.5 x 10^{15} molecules s^{-1}, which translates to an approximate rate of 62 nL/s under conditions of 1 bar atmospheric pressure at room temperature.

$$t_{\text{exchange}}(h) = \frac{V(h)}{N_{cap}} \tag{4.4}$$

Combining equations 4.3 and 4.4, utlizing h_1 = 100 and h_2 = 800 the exchange time becomes t_{exchange} = [30, 260] s which compared to the extraordinary fast exchange time of 11s for the current µ-reactor design is slow and makes it more difficult to investigate transient behavior. Stability test, activity test, and long experiments on low catalyst loading would still be very possible.

Within these time frames, the catalyst has to participate in enough reactions that the product should be at least 50 ppm for the QMS to detect the molecules. Ideally, it should not convert every reacting molecule. The turnover-frequency (TOF) needed for a given concentration C is:

$$TOF = \frac{C}{t_{exchange}} \frac{N_{gas}}{N_{cat}} \tag{4.5}$$

Here, N_{gas} is determined using the ideal gas law, and N_{cat} is the number of active catalytic sites. For a crude estimation one active catalytic site could be translated to one atom and the number of active sites is then given by

$$N_{cat} = (\frac{R_{disc}}{R_{atom}})^2 \cdot \Omega. \tag{4.6}$$

For a simple calculation, considering an average atomic radius (R_{atom}) of 150 pm and a coverage of 5% (Ω), the amount of catalytic active sites is then around 1.5 x 10^{13} sites which is in the same order as for the original µ-reactor design.

The TOF calculation to get a concentration above 50 ppm is then on the order of 5 x 10^{-3} molecules/site/s which is an order of magnitude higher than what could be detected for the original design however, still low enough to be able to measure methanol synthesis. It is possible to deposit more catalyst on the surface if nessecary, however 10% has been the rule of thumb for upper limit to ensure all catalyst are deposited solely and not on top of other catalyst effectively wasting catalytic material and potentially under estimating the catalytic performance.

The main hurdle to overcome is heating and monitoring the actual temperature of the gas and catalyst. Unfortunately, due to time constraints, this was never truly solved and money was not found to manufacture a prototype from the workshop.

4.5.2 Re-design of the µ-reactor platform for photocatalysis

This subsection will describe the re-designed µ-reactor platform for photocatalysis testing. The inspiration to redesign the reactor platform came through collaboration with TUM. Testing, calibration of the capillary and validation of the quantification of the gas species is my main contribution to the project

The current µ-reactor-platform has already been used for multiple experiments in photocatalysis [85, 86, 87, 88].

As described the current µ-reactor design mandates anodic bonding for sealing the pyrex lid to the SiO_2 so reuse after opening is not possible [89]. This makes traditional µ-reactors single-use.

A re-useable µ-reactor with the original's quick response and heightened sensitivity would address the limitations of the current µ-reactor-design.

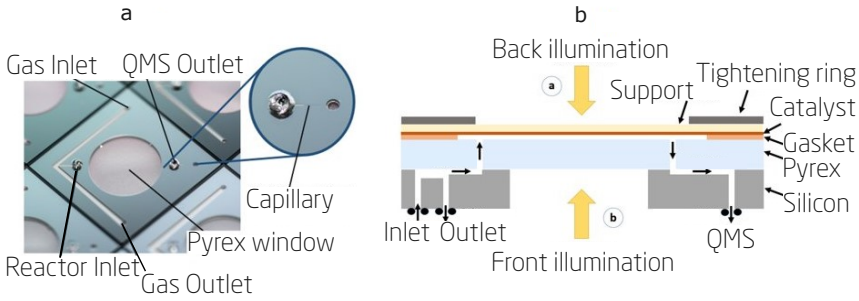

Figure 4.25: A schematics of the re-useable µ-reactor for photocatalytic testing [90].

Leveraging insights from the innovative EC-MS sniffer chip interface has been instrumental in enhancing the µ-reactor design for refining its application in photocatalysis testing [35].

The reaction volume is sealed using an o-ring, facilitating easy assembly, and multiple use of the chip. Through a parafilm gasket, the reactor is leakproof, allowing the µ-reactor to be reused for varied experiments.

The image in figure 4.25a provides a visual representation of the microchip, which includes components like the gas inlet, gas flow channel, gas outlet, entrance to the reaction volume, QMS outlet after the capillary leading to the mass spectrometer, the limiting capillary, and the borosilicate glass window.

Crafting this microchip involves employing conventional cleanroom procedures like UV lithography, deep reactive ion etching, and anodic bonding. A hallmark of the new design, akin to its earlier versions, is the limiting capillary depicted in 4.25a. This capillary restricts the flow of the analyte to the mass spectrometer, eliminating the need for differential pumping. To ensure the mass spectrometer functions reliably, it is crucial to maintain a pressure at or below the 10^{-5} mbar range. Taking into account the turbo pump used in the initial model study (with pumping speed S = 50 l/s), the maximum flux of the analyte to the mass spectrometer, denoted as $\dot{n}_v$, can be calculated as

$$\dot{n}_v = \frac{1}{RT} p_v^0 S_{pump} \approx 2\text{nmol/s} \tag{4.7}$$

Where R is the ideal gas constants, T is the temperature, p_v^0 is the desired pressure in the main chamber with the QMS of 10^{-6} mbar and S_{pump} is the pumping speed of the turbo pump (50 l/s).

Thanks to the capillary, almost 100% of the molecules entering the reactor volume are measured with the QMS since there is no need for differential pumping. Such efficiency translates to a sensitivity that is magnitudes

Table 4.2: Calculated and experimentally measured flux thorugh the capillary of the new µ-reactor design.

	Calculated $\dot{n}_{calc}$ [nmol/s]	Experimental $\dot{n}_{exp}$ [nmol/s]
CO_2	7.0	6.8
CO	6.2	6.2
O_2	5.4	5.2

higher compared to systems with differential pumping [35]. Furthermore, this efficiency enables absolute quantification as the calibrated signal directly correlates with the amount of products formed on the surface of the catalyst.

Figure 4.26 depicts the reactor assembly placed in an adapted stainless steel interface block, a commercial product from Spectro Inlets Aps. The µ-reactor chip sits atop four O-rings that ensure airtight connections to both the mass spectrometer and the gas circulation system, further illustrated in 4.25b.

Above the chip interface, a parafilm sealing gasket and a catalyst layer are positioned and held together with four screws and a tightening ring. If a silicon wafer serves as a catalyst base, an additional glassy carbon plate is added to distribute the screw pressure and avert wafer breakage.

Pre-experiment, the assembly undergoes a leak test by infusing He and tracking the decrease in air signals (oxygen at m/z = 32 and nitrogen at m/z = 28). Once the reactor is air-tight, it can be filled with the reaction gas mix. If needed, residual air can be further minimized by housing the reactor in an inert gas-filled container as used for the current thermal µ-reactor setup.

The molecular flow through the capillary was indirectly measured with a Capacitance Manometer (MKS 220d, 1 mbar pressure, Measurement 4-20 mA [91]) utilizing the same experimental technique as described in section 2.2.2. This was then compared to the mathematical modelling of the molecular flow through the capillary for various gases.

The experimental framework is portrayed in figure 4.27 and comprises the µ-reactor, specific valves, a known reference volume, and the Capacitance Manometer. After certain procedural steps, including pressure monitoring as illustrated in figure 4.28, the method allows for the computation of the molecular flow rate using the ideal gas law.

Empirical tests estimated a capillary flow of 6.8 nmol/s for CO_2 at a pressure of 1.2 bar. This aligns closely with the outcome from mathematical calculation, suggesting a flow rate of 7.0 nmol/s for CO_2 at the same pressure. The validity was further tested using CO and O_2, and results are shown in tabel 4.2.

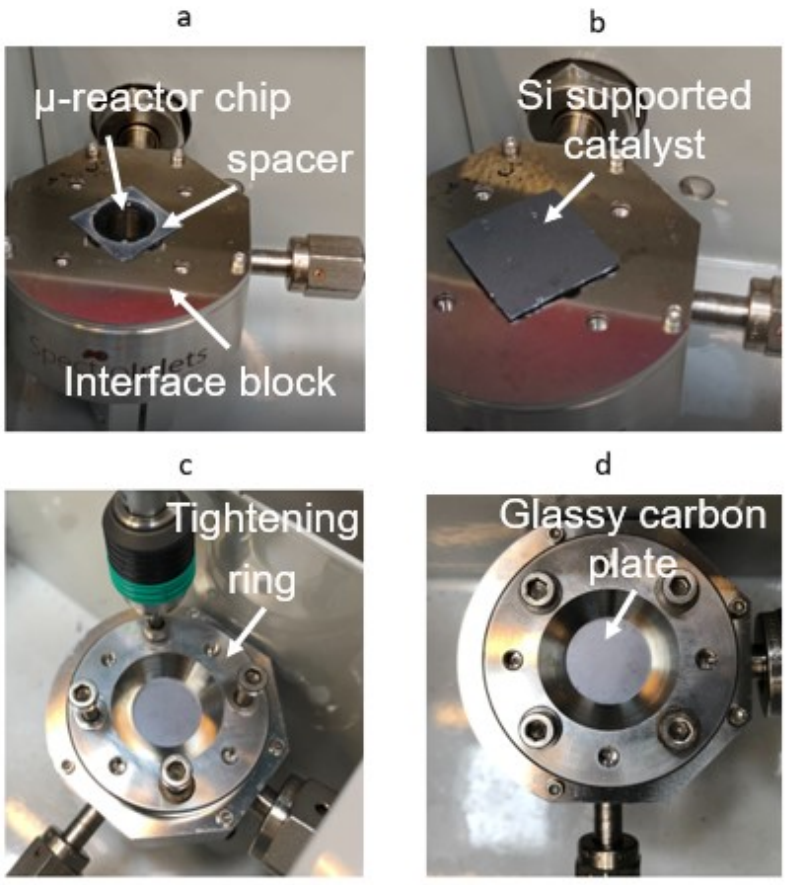

Figure 4.26: A series of pictures showing the mounting of a re-useable μ-reactor for photocatalytic testing [90].

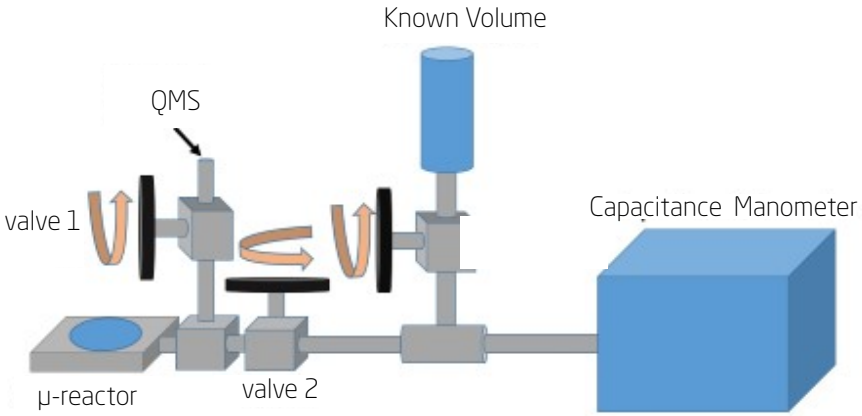

Figure 4.27: A schematics of the setup for the measuring the molecular flux through the capillary of the new re-useable design μ-reactor [90].

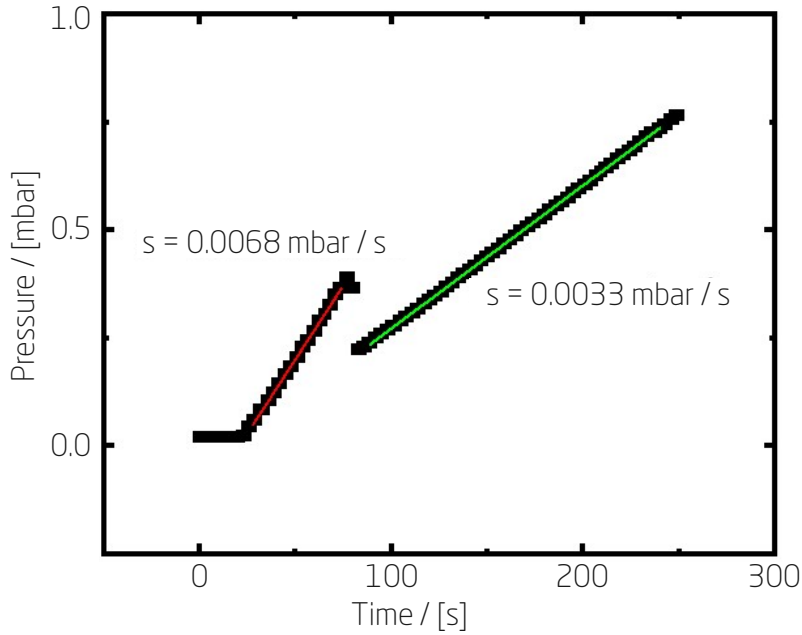

Figure 4.28: The capillary flow of CO_2 is measured by observing the pressure increase over time in an unknown volume, V_0, represented by the red line that illustrates the linear fit of the pressure increase and in the combined unknown volume V_0 plus a reference volume of 26 ml V_{ref}, depicted by the green line that represents the linear fit of the pressure increase [90].

Gas viscosities at 25 °C were sourced from the CRC Handbook of Physics and Chemistry online [92]. There is notable alignment between the experimentally and mathematically derived capillary flow values, with a minimal variance of just 3%.

This new reactor design facilitates easy interchange of catalysts and reaction conditions, which is essential for rapid screening processes for the discovery of new photocatalysts.

Although a reusable µ-reactor chip specifically for thermal catalysis testing has not yet been realized, insights gained from empirical and experimental successes in electrochemical and photocatalytic µ-reactor designs shows the promise of reusable designs. The benefits and advantages considered, efforts to develop a design compatible with various temperatures and pressures appears justifiable and promising.

Chapter 5

Outlook

In this thesis, significant progress in enhancing the µ-reactor platform and investigating heterogeneous catalysis has been made. This work includes the following improvements and programming contributions:

µ-reactor Improvements:

a. Capillary validation: Ensuring accurate and reliable gas flow measurement within the µ-reactor system.
b. Temperature validation: Confirming precise temperature control and measurements for catalytic reaction studies.
c. QMS quantification: Developing a strategy for quantifying quadrupole mass spectrometer signals from amperes to mols/s with manometer capacitance pressure measurements.
d. Heat distribution with and without pyrex spacer: Investigating the influence of a pyrex spacer on the thermal distribution within the µ-reactor.
e. Improve anodic bonding - design of microreactor setup: Optimizing the bonding process and the overall design of the µ-reactor system.

Programming Contributions:

a. Developed PID control for heating: Implementing a PID control algorithm to maintain stable and precise temperature control during catalytic studies.
b. Developed automatic temperature monitoring during anodic bonding: Ensuring accurate temperature measurements throughout the bonding process.
c. Contributed to IXDAT for easy data analysis of raw QMS data for thermal catalysis: Streamlining the analysis of QMS data for more efficient catalytic reaction studies.
d. Develop driver for XGS600 for valve control for setup: Creating a custom driver for precise valve control within the experimental setup.

These improvements and programming contributions serve to strengthen the µ-reactor platform as a versatile and powerful tool for investigating heterogeneous catalysis. By building upon the work presented in this thesis, future research can explore novel catalysts and reaction mechanisms, ultimately contributing to the development of more sustainable and efficient energy solutions.

In this thesis, the μ-reactor has been demonstrated as a thermal catalysis testing platform for mass-selected nanoparticles. The findings indicate that gold (Au) appears to be stabilized by titanium (Ti) anchoring in-flight, overcoming known challenges related to sintering effect of Au nanoparticles.

To support the claim that Ti truly anchored and stabilized the Au catalyst, and not just as a result of measuring apparent size effects of the active catalyst Au, a mass-selected size study of AuTi / Au was conducted.

Ensuring accurate and reliable measurements of catalytic activity of the metal under investigation in the μ-reactor involved an extensive process, from manufacturing at DanChip/NanoLab to thin-film sputtering alternative substrates, deposition of mass selected nanoparticles, storage in a developed Ar storage chamber, and subsequent characterization and activity testing.

Potential future research directions that was started during this PhD study include:

1. Pt single atoms, dimer, and trimers: Investigate the catalytic properties of Pt single atoms, dimers, and trimers through HD exchange experiments.
2. CoCu nanoparticles versus industrial catalyst: Compare the performance of CoCu nanoparticles for direct ethanol synthesis from syngas.
3. AuTi as a Deep Preferential Oxidation catalyst: Assess the potential of AuTi for exceptional CO oxidation and CO preferential oxidation (PROX) in excess hydrogen, aiming to achieve complete CO removal across a wide temperature window.
4. AuTi as a direct methane oxidation catalyst: Evaluate the performance of AuTi for direct oxidation of methane to methanol, contributing to a more sustainable and efficient process.
5. Develop re-usable μ-reactor platform for thermal catalysis

While all of these research directions would have made exciting experiments, time constraints limited their exploration in this thesis. However, they present promising avenues for future research, contributing to our understanding of heterogeneous catalysis and the development of more efficient and sustainable energy solutions.

Bibliography

[1] Richard E. Smalley. "Future global energy prosperity: The terawatt challenge". eng. In: Mrs Bulletin 30.6 (2005), pp. 412–417. ISSN: 19381425, 08837694. DOI: 10.1557/mrs2005.124.

[2] Anders B. Laursen et al. "Availability of elements for heterogeneous catalysis: Predicting the industrial viability of novel catalysts". In: Chinese Journal of Catalysis 39 (1 2018), pp. 16–26. ISSN: 18722067. DOI: 10.1016/S1872-2067(17)62979-6.

[3] Peter C. K. Vesborg and Thomas F. Jaramillo. "Addressing the terawatt challenge: scalability in the supply of chemical elements for renewable energy". In: RSC Advances 2 (21 2012), p. 7933. ISSN: 2046-2069. DOI: 10.1039/c2ra20839c.

[4] Zhi Wei Seh et al. "Combining theory and experiment in electrocatalysis: Insights into materials design". In: Science 355 (6321 Jan. 2017). ISSN: 0036-8075. DOI: 10.1126/science.aad4998.

[5] P. Stoltze and J. K. Nørskov. "Bridging the "Pressure Gap" between Ultrahigh-Vacuum Surface Physics and High-Pressure Catalysis". In: Physical Review Letters 55 (22 Nov. 1985), pp. 2502–2505. ISSN: 0031-9007. DOI: 10.1103/PhysRevLett.55.2502.

[6] R Imbihl, RJ Behm, and R Schl{ö}gl. "Bridging the pressure and material gap in heterogeneous catalysis". In: Physical Chemistry Chemical Physics 9 (27 2007), p. 3459. ISSN: 1463-9076. DOI: 10.1039/b706675a.

[7] H.-J. Freund et al. "Bridging the pressure and materials gaps between catalysis and surface science: clean and modified oxide surfaces". In: Topics in Catalysis 15 (2/4 2001), pp. 201–209. ISSN: 10225528. DOI: 10.1023/A:1016686322301.

[8] Sara Blomberg et al. "Bridging the Pressure Gap in CO Oxidation". In: ACS Catalysis 11 (15 Aug. 2021), pp. 9128–9135. ISSN: 2155-5435. DOI: 10.1021/acscatal.1c00806.

[9] Toke R. Henriksen et al. "Highly sensitive silicon microreactor for catalyst testing". In: Review of Scientific Instruments 80 (12 Dec. 2009), p. 124101. ISSN: 0034-6748. DOI: 10.1063/1.3270191. URL: http://aip.scitation.org/doi/10.1063/1.3270191.

[10] Ib Chorkendorff and J. W. Niemantsverdriet. Concepts of modern catalysis and kinetics. second. Wiley-VCH, 2007. DOI: 10.1002/aoc.801.

[11] Potential diagram. 2023. URL: https://en.wikipedia.org/wiki/Catalysis#/media/File:CatalysisScheme.png.

[12] Ib Chorkendorff. Surface Physics/Chemistry. 2014.

[13] MP Andersson et al. "Structure sensitivity of the methanation reaction: H2-induced CO dissociation on nickel surfaces". In: Journal of Catalysis 255.1 (2008), pp. 6–19.

[14] Masatake Haruta et al. "Low-Temperature Oxidation of CO over Gold Supported on TiO2, ⊠-Fe2O3, and Co3O4". In: Journal of Catalysis 144 (1 Nov. 1993), pp. 175–192. ISSN: 00219517. DOI: 10.1006/jcat.1993.1322. URL: https://linkinghub.elsevier.com/retrieve/pii/S0021951783713229.

[15] Masatake Haruta. "Size- and support-dependency in the catalysis of gold". In: Catalysis Today 36 (1 Apr. 1997), pp. 153–166. ISSN: 09205861. DOI: 10.1016/S0920-5861(96)00208-8. URL: http://linkinghub.elsevier.com/retrieve/pii/S0920586196002088%20https://linkinghub.elsevier.com/retrieve/pii/S0920586196002088.

[16] Lin Li et al. "Investigation of Catalytic Finite-Size-Effects of Platinum Metal Clusters". In: The Journal of Physical Chemistry Letters 4 (1 2013). PMID: 26291235, pp. 222–226. DOI: 10.1021/jz3018286. URL: https://doi.org/10.1021/jz3018286.

[17] J. Kleis et al. "Finite Size Effects in Chemical Bonding: From Small Clusters to Solids". In: Catalysis Letters 141 (8 Aug. 2011), pp. 1067–1071. ISSN: 1011-372X. DOI: 10.1007/s10562-011-0632-0.

[18] A. Sanchez et al. "When Gold Is Not Noble: Nanoscale Gold Catalysts". In: The Journal of Physical Chemistry A 103 (48 Dec. 1999), pp. 9573–9578. ISSN: 1089-5639. DOI: 10.1021/jp9935992.

[19] Uzi Landman et al. "Factors in gold nanocatalysis: oxidation of CO in the non-scalable size regime". In: Topics in Catalysis 44 (1-2 June 2007), pp. 145–158. ISSN: 1022-5528. DOI: 10.1007/s11244-007-0288-6.

[20] Toke Riishøj Henriksen. "Silicon Microreactors for Measurements of Catalytic Activity". In: (April 2010). URL: http://orbit.dtu.dk/fedora/objects/orbit:83099/datastreams/file_5216633/content.

[21] Jakob Lind Olsen. "Heterogeneous catalysis in highly sensitive microreactors". In: (2010), p. 125. URL: http://orbit.dtu.dk/fedora/objects/orbit:82897/datastreams/file%7B_%7D5138424/content.

[22] Peter Christian Kjærgaard Vesborg. "Udforskning af nye nano strukturerede materialer til fremstilling af hydrogen". In: (2010).

[23] Robert Jensen. "μ-reactors for Heterogeneous Catalysis". In: (2012).

[24] Jakob Riedel. "-reactor measurements of catalytic activity of mass selected nano-particles". In: (2016).

[25] Shigeki Yatsuya et al. "A New Technique for the Formation of Ultrafine Particles by Sputtering". In: Japanese Journal of Applied Physics 25 (1A Jan. 1986), p. L42. ISSN: 0021-4922. DOI: 10.1143/JJAP.25.L42.

[26] Yves Huttel. Gas-Phase Synthesis of Nanoparticles. Ed. by Yves Huttel. Wiley-VCH Verlag GmbH & Co. KGaA, July 2017. ISBN: 9783527698417. DOI: 10.1002/9783527698417.

[27] S. Pratontep et al. "Size-selected cluster beam source based on radio frequency magnetron plasma sputtering and gas condensation". In: Review of Scientific Instruments 76 (4 Apr. 2005), p. 045103. ISSN: 0034-6748. DOI: 10.1063/1.1869332.

[28] Anders Bodin. "Synthesis of Nanoparticle Model Systems for Sustainable Catalysis by Gas Aggregation". In: (2017).

[29] Béla Sebök. "Creating model systems for catalysis with mass-selected nanoparticles: Characterization and porperties". In: (2017).
[30] Niklas Mørch Secher. "Mass-Selected Model Systems in Catalysis: from Nanoparticles to Single Atoms". eng. 2020.
[31] Peter C. K. Vesborg et al. "Note: Anodic bonding with cooling of heat-sensitive areas". In: Review of Scientific Instruments 81 (1 Jan. 2010), p. 016111. ISSN: 0034-6748. DOI: 10.1063/1.3277117.
[32] Caroline A. Schneider, Wayne S. Rasband, and Kevin W. Eliceiri. "NIH Image to ImageJ: 25 years of image analysis". eng. In: Nature Methods 9.7 (2012), pp. 671–675. ISSN: 15487105, 15487091. DOI: 10.1038/nmeth.2089.
[33] Peter R.N. Childs. Resistance temperature detectors. Elsevier, 2001, pp. 145–193. DOI: 10.1016/B978-075065080-9/50006-X.
[34] Ulrich J. Quaade, Søren Jensen, and Ole Hansen. "Fabrication and modeling of narrow capillaries for vacuum system gas inlets". In: Journal of Applied Physics 97 (4 Feb. 2005), p. 044906. ISSN: 0021-8979. DOI: 10.1063/1.1829377.
[35] Daniel B. Trimarco et al. "Enabling real-time detection of electrochemical desorption phenomena with sub-monolayer sensitivity". In: Electrochimica Acta 268 (Apr. 2018), pp. 520–530. ISSN: 00134686. DOI: 10.1016/j.electacta.2018.02.060.
[36] B. Lautrup. Physics of Continuous Matter: Exotic and Everyday Phenomena in the Macroscopic World, Second Edition. CRC Press LLC, 2011. ISBN: 9781420077001.
[37] Alexander Roth. Vacuum Technology. third. Elsevier, 1990.
[38] Philip E. Miller and M. Bonner Denton. "The quadrupole mass filter: Basic operating concepts". In: Journal of Chemical Education 63 (7 July 1986), p. 617. ISSN: 0021-9584. DOI: 10.1021/ed063p617.
[39] John W Honour. "Benchtop mass spectrometry in clinical biochemistry". In: Annals of Clinical Biochemistry: International Journal of Laboratory Medicine 40 (6 Nov. 2003), pp. 628–638. ISSN: 0004-5632. DOI: 10.1258/000456303770367216.
[40] NIST. National Institute of Standards and Technology, NIST Chemistry WebBook. 2023. URL: https://webbook.nist.gov/.
[41] Søren Bertelsen Scott. "Isotope-Labeling Studies in Electrocatalysis for Renewable Energy Conversion". eng. 2019.
[42] Daniel Bøndergaard Trimarco. "Real-time detection of sub-monolayer desorption phenomena during electrochemical reactions: Instrument development and applications". In: Downloaded from orbit.dtu.dk on (2017). URL: https://backend.orbit.dtu.dk/ws/files/138864211/Daniel_Trimarco_PhD_thesis_Aug_2017.pdf.
[43] M. P. Seah and W. A. Dench. "Quantitative electron spectroscopy of surfaces: a standard data base for electron inelastic mean free paths in solids". eng. In: Surface and Interface Analysis 1.1 (1979), pp. 2–11. ISSN: 10969918, 01422421. DOI: 10.1002/sia.740010103.
[44] Charles C. Chusuei and D.Wayne Goodman. "X-Ray Photoelectron Spectroscopy". eng. In: Encyclopedia of Physical Science and Technology (2003), pp. 921–938. DOI: 10.1016/B0-12-227410-5/00830-9.

[45] Gratian R. Bamwenda et al. "The influence of the preparation methods on the catalytic activity of platinum and gold supported on TiO2 for CO oxidation". eng. In: Catalysis Letters 44.1-2 (1997), pp. 83–87. ISSN: 1572879x, 1011372x. DOI: 10.1023/a:1018925008633.

[46] M. Valden et al. "Structure sensitivity of CO oxidation over model Au/TiO2 catalysts". In: Catalysis Letters (1998). ISSN: 1011372X. DOI: 10.1023/A:1019028205985.

[47] B. Hammer and J. K. Norskov. "Why gold is the noblest of all the metals". In: Nature 376 (6537 July 1995), pp. 238–240. ISSN: 0028-0836. DOI: 10.1038/376238a0.

[48] William Arthur and Richard Vernon Bone Wheeler. "I. The combination of hydrogen and oxygen in contact with hot surfaces". In: Philosophical Transactions of the Royal Society of London. Series A, Containing Papers of a Mathematical or Physical Character 206 (402-412 Jan. 1906), pp. 1–67. ISSN: 0264-3952. DOI: 10.1098/rsta.1906.0015.

[49] William Arthur Bone and G.W. Andrew. "Studies upon catalytic combustion.—Part I. The union of carbon monoxide and oxygen in contact with a gold surface". In: Proceedings of the Royal Society of London. Series A, Containing Papers of a Mathematical and Physical Character 109 (751 Nov. 1925), pp. 459–476. ISSN: 0950-1207. DOI: 10.1098/rspa.1925.0138.

[50] Masatake Haruta et al. "Novel Gold Catalysts for the Oxidation of Carbon Monoxide at a Temperature far Below 0 °C". In: Chemistry Letters 16 (2 Feb. 1987), pp. 405–408. ISSN: 0366-7022. DOI: 10.1246/cl.1987.405.

[51] Ndepana A. Gaya et al. "A review on CO oxidation, methanol synthesis, and propylene epoxidation over supported gold catalysts". In: Catalysis for Sustainable Energy 6.1 (2019), pp. 13–37. DOI: doi:10.1515/cse-2019-0003. URL: https://doi.org/10.1515/cse-2019-0003.

[52] Britt Hvolbæk et al. "Catalytic activity of Au nanoparticles". In: Nano Today 2 (4 Aug. 2007), pp. 14–18. ISSN: 17480132. DOI: 10.1016/S1748-0132(07)70113-5.

[53] N Lopez. "On the origin of the catalytic activity of gold nanoparticles for low-temperature CO oxidation". In: Journal of Catalysis 223 (1 Apr. 2004), pp. 232–235. ISSN: 00219517. DOI: 10.1016/j.jcat.2004.01.001.

[54] M. Valden, X. Lai, and D. W. Goodman. "Onset of catalytic activity of gold clusters on titania with the appearance of nonmetallic properties". In: Science (1998). ISSN: 00368075. DOI: 10.1126/science.281.5383.1647.

[55] Lei Zhang, Rajendra Persaud, and Theodore E. Madey. "Ultrathin metal films on a metal oxide surface: Growth of Au on <math display="inline"> <mrow> <msub> <mrow> <mi mathvariant="normal">TiO</mi> </mrow> <mrow> <mn>2</mn> </mrow> </msub> </mrow> </math> (110)". In: Physical Review B 56 (16 Oct. 1997), pp. 10549–10557. ISSN: 0163-1829. DOI: 10.1103/PhysRevB.56.10549.

[56] S.C. Parker et al. "Island growth kinetics during the vapor deposition of gold onto TiO2(110)". In: Surface Science 441 (1 Oct. 1999), pp. 10–20. ISSN: 00396028. DOI: 10.1016/S0039-6028(99)00753-0.

[57] F. Yang, M. S. Chen, and D. W. Goodman. "Sintering of Au Particles Supported on TiO 2 (110) during CO Oxidation". In: The Journal of Physical Chemistry C 113 (1 Jan. 2009), pp. 254–260. ISSN: 1932-7447. DOI: 10.1021/jp807865w. URL: https://pubs.acs.org/doi/10.1021/jp807865w.

[58] B. K. Min et al. "Role of Defects in the Nucleation and Growth of Au Nanoclusters on SiO ₂ Thin Films". In: The Journal of Physical Chemistry B 108 (42 Oct. 2004), pp. 16339–16343. ISSN: 1520-6106. DOI: 10.1021/jp046519p.

[59] W.T. Wallace, B.K. Min, and D.W. Goodman. "The stabilization of supported gold clusters by surface defects". In: Journal of Molecular Catalysis A: Chemical 228 (1-2 Mar. 2005), pp. 3–10. ISSN: 13811169. DOI: 10.1016/j.molcata.2004.09.085.

[60] Yubiao Niu et al. "Reduced sintering of mass-selected Au clusters on SiO 2 by alloying with Ti: an aberration-corrected STEM and computational study". In: Nanoscale 10 (5 2018), pp. 2363–2370. ISSN: 2040-3364. DOI: 10.1039/C7NR06323G. URL: http://xlink.rsc.org/?DOI=C7NR06323G.

[61] Mingshu Chen and D Wayne Goodman. "Catalytically active gold on ordered titania supports". In: Chemical Society Reviews 37 (9 2008), pp. 1860–1870. ISSN: 0306-0012. DOI: 10.1039/B707318F. URL: http://dx.doi.org/10.1039/B707318F.

[62] Atsushi Beniya and Shougo Higashi. "Towards dense single-atom catalysts for future automotive applications". In: Nature Catalysis 2 (7 2019), pp. 590–602. ISSN: 2520-1158. DOI: 10.1038/s41929-019-0282-y. URL: http://dx.doi.org/10.1038/s41929-019-0282-y.

[63] Louise Olsson and Bengt Andersson. "Kinetic Modelling in Automotive Catalysis". In: Topics in Catalysis 28 (1-4 Apr. 2004), pp. 89–98. ISSN: 1022-5528. DOI: 10.1023/B:TOCA.0000024337.50617.8e.

[64] Charles T Campbell. "Nanoparticle Gold Catalysis". In: Science 306 (2004), pp. 234–235.

[65] M HARUTA. "Gold catalysts prepared by coprecipitation for low-temperature oxidation of hydrogen and of carbon monoxide". In: Journal of Catalysis 115 (2 Feb. 1989), pp. 301–309. ISSN: 00219517. DOI: 10.1016/0021-9517(89)90034-1. URL: https://linkinghub.elsevier.com/retrieve/pii/0021951789900341.

[66] Ganghua Xiang et al. "Atomically dispersed Au catalysts for preferential oxidation of CO in H2-rich stream". In: Applied Catalysis B: Environmental 296 (2021), p. 120385. ISSN: 0926-3373. DOI: https://doi.org/10.1016/j.apcatb.2021.120385. URL: https://www.sciencedirect.com/science/article/pii/S0926337321005117.

[67] J.F. Moulder and J. Chastain. Handbook of X-ray Photoelectron Spectroscopy: A Reference Book of Standard Spectra for Identification and Interpretation of XPS Data. Physical Electronics Division, Perkin-Elmer Corporation, 1992. ISBN: 9780962702624.

[68] Hailian Tang et al. "Classical strong metal–support interactions between gold nanoparticles and titanium dioxide". In: Science Advances 3 (10 Oct. 2017). ISSN: 2375-2548. DOI: 10.1126/sciadv.1700231.

[69] Soren Scott. ixdat: open source experimental data manipulation. 2020. URL: https://ixdat.readthedocs.io/en/latest/index.html.

[70] L. Mond. "The History of My Process of Nickel Extraction". In: Journal of Organometallic Chemistry 383 (1-3 Feb. 1990), pp. 7–10. ISSN: 0022328X. DOI: 10.1016/0022-328X(90)85118-I.

[71] S. Dey and N.S. Mehta. "Oxidation of carbon monoxide over various nickel oxide catalysts in different conditions: A review". In: Chemical Engineering Journal Advances 1 (Sept. 2020), p. 100008. ISSN: 26668211. DOI: 10.1016/j.ceja.2020.100008.

[72] Olivia Fjord Sloth. "Catalytic activity measurements using μ-reactors". Technical University of Denmark, 2020.

[73] Matthijs A van Spronsen, Joost W M Frenken, and Irene M N Groot. "Surface science under reaction conditions: CO oxidation on Pt and Pd model catalysts". In: Chem. Soc. Rev. 46 (14 2017), pp. 4347–4374. DOI: 10.1039/C7CS00045F. URL: http://dx.doi.org/10.1039/C7CS00045F.

[74] Rodney P. Elliott and Francis A. Shunk. "The Au–Si (Gold-Silicon) system". In: Bulletin of Alloy Phase Diagrams 2 (3 Dec. 1981), pp. 359–362. ISSN: 0197-0216. DOI: 10.1007/BF02868294.

[75] J. Carvill. Mechanical Engineer's Data Handbook. Elsevier, 1993. ISBN: 9780080511351. DOI: 10.1016/C2009-0-24207-3.

[76] Peter C.K. Vesborg et al. "Gas-phase photocatalysis in μ-reactors". In: Chemical Engineering Journal 160 (2 June 2010), pp. 738–741. ISSN: 13858947. DOI: 10.1016/j.cej.2010.03.083.

[77] Klavs F. Jensen. "Microreaction engineering — is small better?" In: Chemical Engineering Science 56 (2 Jan. 2001), pp. 293–303. ISSN: 00092509. DOI: 10.1016/S0009-2509(00)00230-X.

[78] J.J. Brandner et al. "Fast temperature cycling in microstructure devices". In: Chemical Engineering Journal 101 (1-3 Aug. 2004), pp. 217–224. ISSN: 13858947. DOI: 10.1016/j.cej.2003.11.020.

[79] George Wallis and Daniel I. Pomerantz. "Field Assisted Glass-Metal Sealing". In: Journal of Applied Physics 40 (10 Sept. 1969), pp. 3946–3949. ISSN: 0021-8979. DOI: 10.1063/1.1657121.

[80] Ya-Rong Zheng et al. "Monitoring oxygen production on mass-selected iridium–tantalum oxide electrocatalysts". In: Nature Energy 7 (1 Dec. 2021), pp. 55–64. ISSN: 2058-7546. DOI: 10.1038/s41560-021-00948-w.

[81] Degenhart Hochfilzer et al. "The Importance of Potential Control for Accurate Studies of Electrochemical CO Reduction". In: ACS Energy Letters 6 (5 May 2021), pp. 1879–1885. ISSN: 2380-8195. DOI: 10.1021/acsenergylett.1c00496.

[82] Soren B. Scott et al. "Anodic molecular hydrogen formation on Ru and Cu electrodes". In: Catalysis Science & Technology 10 (20 2020), pp. 6870–6878. ISSN: 2044-4753. DOI: 10.1039/D0CY01213K.

[83] Kevin Krempl et al. "Dynamic Interfacial Reaction Rates from Electrochemistry–Mass Spectrometry". In: Analytical Chemistry 93 (18 May 2021), pp. 7022–7028. ISSN: 0003-2700. DOI: 10.1021/acs.analchem.1c00110.

[84] Degenhart Hochfilzer et al. "Transients in Electrochemical CO Reduction Explained by Mass Transport of Buffers". In: ACS Catalysis 12 (9 May 2022), pp. 5155–5161. ISSN: 2155-5435. DOI: 10.1021/acscatal.2c00412.

[85] Morten G. Nielsen et al. "A generic model for photocatalytic activity as a function of catalyst thickness". In: Journal of Catalysis 289 (May 2012), pp. 62–72. ISSN: 00219517. DOI: 10.1016/j.jcat.2012.01.015.

[86] Peter C. K. Vesborg et al. "Quantitative Measurements of Photocatalytic CO-Oxidation as a Function of Light Intensity and Wavelength over TiO ₂ Nanotube Thin Films in μ-Reactors". In: The Journal of Physical Chemistry C 114 (25 July 2010), pp. 11162–11168. ISSN: 1932-7447. DOI: 10.1021/jp100552x.

[87] Fabio Dionigi et al. "Suppression of the water splitting back reaction on GaN:ZnO photocatalysts loaded with core/shell cocatalysts, investigated using a μ-reactor". In: Journal of Catalysis 292 (Aug. 2012), pp. 26–31. ISSN: 00219517. DOI: 10.1016/j.jcat.2012.03.021.

[88] Fabio Dionigi et al. "Gas phase photocatalytic water splitting with Rh2−yCry03/GaN:ZnO in μ-reactors". In: Energy & Environmental Science 4 (8 2011), p. 2937. ISSN: 1754-5692. DOI: 10.1039/c1ee01242h.

[89] F. Dionigi et al. "A transparent Pyrex μ-reactor for combined in situ optical characterization and photocatalytic reactivity measurements". In: Review of Scientific Instruments 84 (10 Oct. 2013). ISSN: 0034-6748. DOI: 10.1063/1.4826495.

[90] Degenhart Hochfilzer et al. "Enabling real-time detection of photocatalytic reactions by a re-useable micro-reactor". In: Measurement Science and Technology 35 (1 Jan. 2024), p. 015903. ISSN: 0957-0233. DOI: 10.1088/1361-6501/acfe2c.

[91] Pam Basu and John T. Yates. "An apparatus for temperature programmed desorption from high surface area solids: The adsorption and desorption of C2H4 from NaX-zeolite". In: Surface Science 177 (2 Dec. 1986), pp. 291–313. ISSN: 00396028. DOI: 10.1016/0039-6028(86)90140-8.

[92] CRC Handbook of Chemistry and Physics. 2023. URL: https://hbcp.chemnetbase.com/faces/contents/ContentsSearch.xhtml.

[93] Chris Parmer. Dash open source python package. 2017. URL: https://dash.plotly.com/.

[94] Kenneth Nielsen et al. "An Open-Source Data Storage and Visualization Back End for Experimental Data". In: SLAS Technology 19 (2 Apr. 2014), pp. 183–190. ISSN: 24726303. DOI: 10.1177/2211068213503824.

Appendix A

Appended papers

Paper I

Soren B. Scott[1]*, Anna Winiwarter[1, 2], Alexander Krabbe[3], Caiwu Liang[1], Kevin Krempl[3], Daisy Thornton[1], Rose Oates[1], Benjamin Moss[1], Reshma R. Rao[1], Ib Chorkendorff[3], Ifan E. L. Stephens[1], Kenneth Nielsen[2]

[1] Department of Materials, Imperial College London, UK
[2] Spectro Inlets A/S, Copenhagen, Denmark
[3] Department of Physics, Technical University of Denmark, Denmark
In preparation, 2023

Abstract

Open science, based on transparent and useful public access of research data, is expected to accelerate developments in energy conversion and storage technologies, as required to meet global challenges. However, effectively harnessing the promise of open science requires better tools for organization, analysis, and visualization of experimental data. The In-Situ Experimental Data Tool, or "ixdat", is one such tool that is optimized for the complex composite data sets generated by measurement techniques used in energy and materials sciences, especially electrochemistry and catalysis. At its core, ixdat is an open-source python package that is well-documented and easy to use (see https://ixdat.readthedocs.org). It has a pluggable design, so that raw data sources from differently formatted files or different database backends can be interchanged while preserving the user interface. A relational model of experimental data facilitates the task of lining up multiple data series from a single hyphenated measurement technique (such as electrochemistry - mass spectrometry and other in-situ techniques), as well as the task of organizing data from large research projects. Ixdat is already used to facilitate the open sourcing of experimental data and transparent analysis procedures via github repositories for a growing number of articles. This article presents the concepts behind ixdat using examples from water oxidation electrocatalysis, with a special focus on welcoming new users and developers.

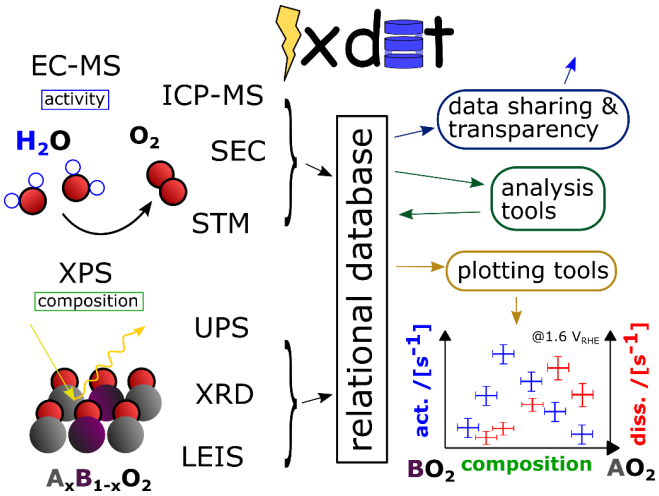
xdet
EC-MS
activity
ICP-MS
SEC
STM
XPS
composition
UPS
XRD
LEIS
relational database
data sharing & transparency
analysis tools
plotting tools
@1.6 V_RHE
act. /[s^-1]
diss. /[s^-1]
BO2 composition AO2
H2O
O2
AxB1-xO2

Figure A.1

Appendix B

μ-reactors setup

Mounting block

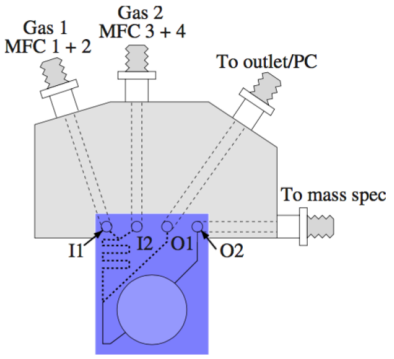

Figure B.1: Schematics of the mounting block used in the μ-reactor setups at DTU. Adapted from [24].

Baratron calibration

The molar flow rate through the capillary in the μ-reactors are calculated using a calibration measurement involving the Baratron attached on the backside. The pressure rate is measured when the μ-reactor molar flow rate $\dot{n}$ is collected in an unknown, evacuated volume V_0 (the pressure rate is $\dot{p}_1$) and with a known evacuated volume V_{ref} (pressure rate $\dot{p}_2$) added.

Using the ideal gas law, we get

$$\dot{p}_1 V_0 = \dot{n} RT \tag{B.1}$$

$$\dot{p}_2 (V_0 + V_r ef) = \dot{n} RT \tag{B.2}$$

$$\tag{B.3}$$

By eliminating the unknown volume V_0, we obtain the experimental molar flow rate

$$\dot{n}_{exp} = \frac{V_{ref}}{RT} \cdot \frac{\dot{p}_1 \dot{p}_2}{\dot{p}_1 - \dot{p}_2} \tag{B.4}$$

V_{ref} is 26mL. V_0 can then be calculated to 34mL using the fitted paramaters $p_1 = 0.00081$ mbar/s and $p_2 = 0.00046$ mbar/s seen in figure 2.12

Flux through the capillary at different temperatures

Table B.1: Expected and measured flux with temperature estimated from measured flux and TC / RTD temperature measurements. White cells indicate UHV in the containment volume and blue cells indicate Ar at 10 mbar pressure in the containment volume.

	Expected flux [nmol/s]	Measured flux [nmol/s]	Effective temperature [K]	Measured TC / RTD temperature [K]
0	7.47e-1	7.03e-1	309	298 / 300
1	7.18e-1	6.38e-1	327	305 / 320
2	6.84e-1	5.99e-1	340	314 / 340
3	6.48e-1	5.31e-1	366	324 / 360
4	6.23e-1	5.03e-1	379	332 / 373
5	5.91e-1	4.74e-1	394	343 / 400
6	4.95e-1	3.86e-1	451	383 / 470
7	4.53e-1	3.55e-1	477	405 / 498
8	3.87e-1	3.24e-1	508	450 / 558
9	3.59e-1	2.85e-1	558	473 / 606
10	3.28e-1	2.68e-1	583	504 / 630
11	3.26e-1	3.24e-1	509	506 / 558
12	3.31e-1	3.54e-1	469	501 / 530
13	5.16e-1	4.79e-1	402	373 / 387
14	5.91e-1	5.48e-1	370	343 / 351

Temperature measured by flux changes through the capillary

Plot to display the standard experimental setup estimating true temperature in the reactor volume utilizing the capillary equation and flux measurement through the capillary.

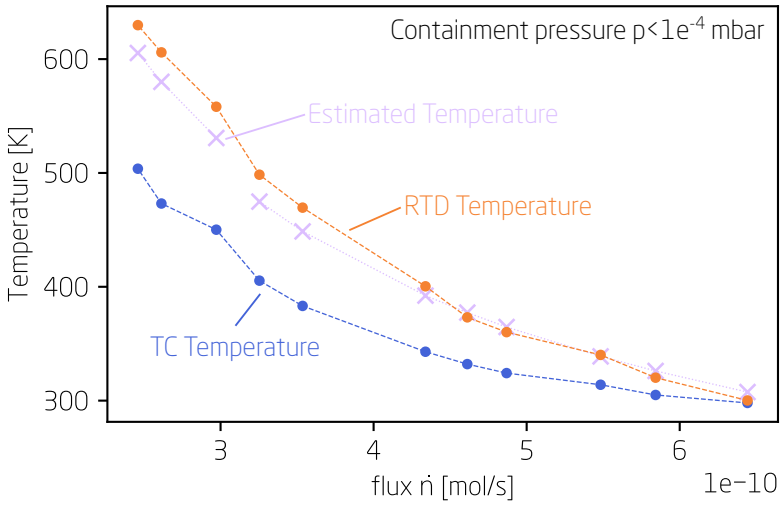

Figure B.2: The graph presents the temperature measured by the thermocouple (TC, blue line) and the resistance temperature detector (RTD, orange line), along with the estimated temperature (Lavender line) as a function of the measured flux through the capillary, obtained from the pressure increase on the backside measured with the Baratron. The temperature estimated is shifted 25K up to reflect the heat profile. The temperature recorded by the RTD aligns more closely with the expected temperature derived from the measured flux compared to the temperature measured by the TC.

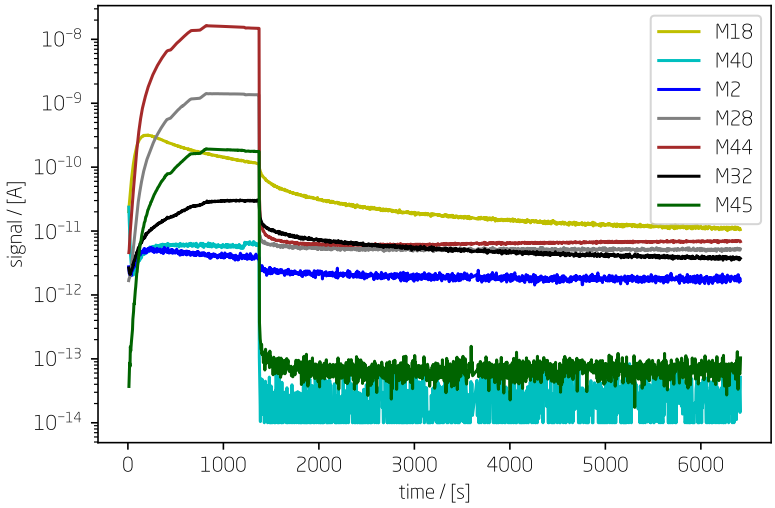

Figure B.3: Mass spec signals during temperature estimation from flux measurement through capillary

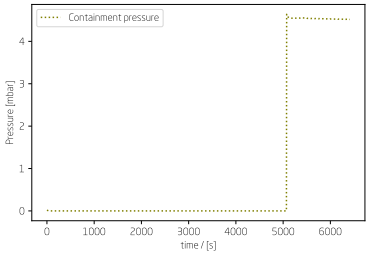

(a) Pressure profile in the containment during the experiment

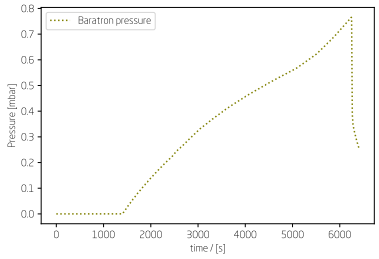

(b) Pressure profile in the baratron during the experiment

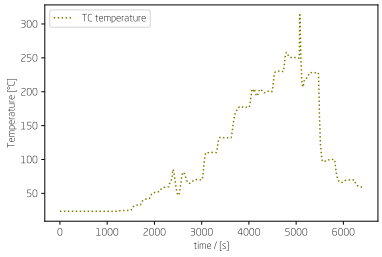

(c) Temperature profile measured by the thermo couple during the experiment

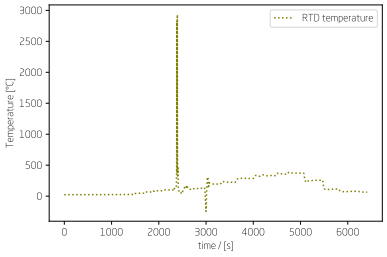

(d) Temperature profile measured by the RTD during the experiment

Appendix C

Programming

LiveWebServer in Dash

I developed a LiveWebServer in the open source framwork Dash [93] that can be found https://github.com/CINF/PyExpLabSys/tree/master/PyExpLabSys/apps

Live monitoring of an experiment is crucial for several reasons. Firstly, it allows for real-time observation of the experiment, enabling researchers to promptly detect any anomalies or unexpected results. This can save valuable time and resources by identifying potential issues early in the experiment, rather than waiting for the experiment to finish before analyzing the data and discovering problems.

Secondly, live monitoring provides researchers with the ability to make adjustments to the experiment on-the-fly, if necessary. For example, if the data shows that the flow, pressure or temperature is not within the desired range, the researchers can immediately adjust the settings to correct the issue, rather than waiting for the experiment to finish and starting over again.

Finally, by monitoring the equipment in real-time, researchers can ensure that the experiment is proceeding as planned, and that the data being collected is accurate and reliable.

PyExpLabSys

PyExpLabSys is an open source project that simplifies socket communication protocols, making it easier to control equipment and collect data. It includes multiple open source drivers used at SurfCat [94].

XGS600 improved driver

I made an enhancement to the XGS600 driver in PyExpLabSys by enabling more advanced valve control capabilities and automatic logging of the valve state. These improvements have led to better error detection and facilitated troubleshooting. The driver can be found here https://github.com/CINF/ PyExpLabSys/blob/master/PyExpLabSys/drivers/xgs600.py

Improvements of logging and controlling the anodic bonding setup

Introducing a new PyExpLabsys module for efficient database logging of meta values. This powerful tool has been employed in the µ-reactor anodic

cold bonding setup to constantly monitor the perimeter of the sensitive reactor area, including critical temperatures, voltage, current, and experimental time. This ensures accurate and reliable tracking of important metrics, helping to facilitate informed decision-making and improve overall experimental outcomes. The app can be located here https://github.com/CINF/PyExpLabSys/tree/master/PyExpLabSys/apps/qms

Customized colour scheme for channel_list.txt in VIM

I have developed a personalized color scheme for the channel_list.txt file, which is utilized to highlight mass channels and meta channels enabled and recorded throughout an experiment. This scheme facilitates easier differentiation and quick identification of channels, leading to a more efficient and seamless experiment setup process.

Data treatment

Most of the data treatment is done using the open source programming language python.

EC_MS

A collection of python scripts developed by former PhD student Søren Scott and can be found on github.com/ScottSoren/EC_MS. These scripts were used in the beginning to quantify mass spec data from the effective length of the capillary of a sniffer chip to molecules not in house as pure gas e.i. methane, methanol and ethanol.

Ixdat

Ixdat is an open-source project with two main components. The first component focuses on the raw data and the experimenter, and combines separate data files into one dataset. The second component focuses on results and the high-level researcher, and allows for querying of results. The two components are combined into one software, using a relational structure to group datasets based on metadata. This software will provide standardized analysis tools and a means of comparing results to the state-of-the-art, as well as a way to open-source data. The design will be highly pythonic, object-oriented, pluggable, and dynamic, with a focus on documentation to facilitate diverse users. In the near-to-mid future, the software will require some programming skill, but select functionality will eventually have GUIs if there is interest. The project will be collaborative, allowing anyone with time and programming skills to add tools or databases. Overall, Ixdat aims to improve the overall quality and standardization of experimental research. This package has been primarily used to calibrate QMS mass spec data obtained through the capillary of the µ-reactor and subsequent datatreatment of single measurements combining mass spectra taken over time with mass time data [69].

Appendix D

SEM images during anodic bonding

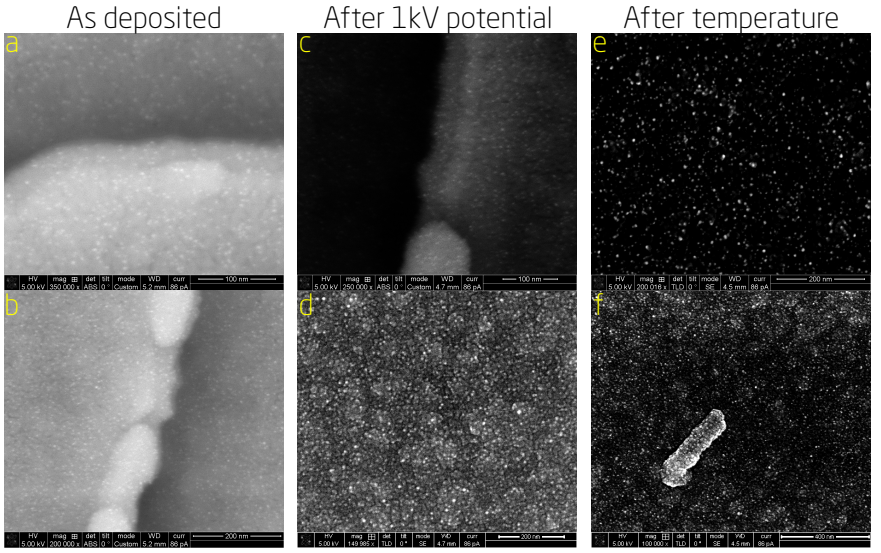

Figure D.1: SEM images of the same µ-reactor with 50 nm TiO_2 substrate and 5% coverage of 3.5 nm AuTi nanoparticles as prepared, and after the applying only voltage and after applying only temperature during anodic bonding. Fig a and b are as prepared 3.5 nm nanoparticles. Fig c and d are SEM images after applying 1kV to the sample for 1 hour. Fig e and f are SEM images after applying 350 degrees temperature and active 10 degrees cooling on the sensitive reactor area.

Appendix E

Apparent activation energy plot

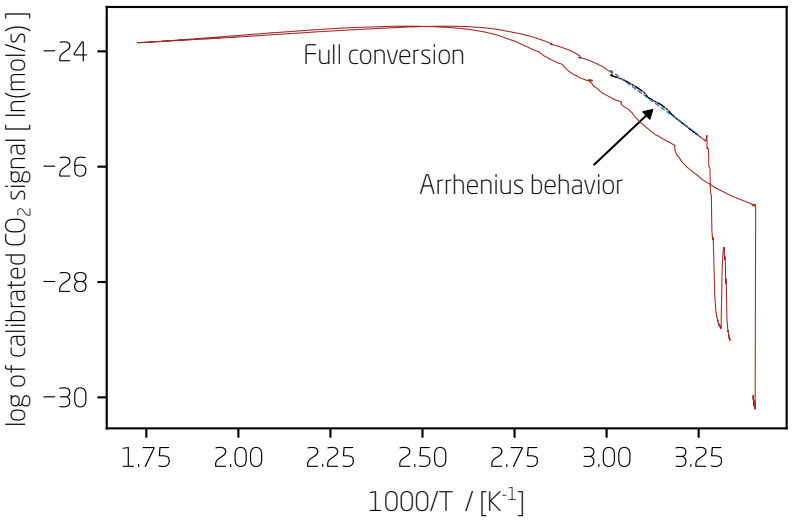

Figure E.1: A plot of the logarithm of the reaction rate versus the inverse of the temperature of a AuTi nanoparicle on SiO_2 support. The arrhnius like behaviour is pointed at with an arrow. The area where the line decline is because of full conversion of the CO and the flux through the capillary is decreasing with increasing temperature.

Technical
University of
Denmark

Fysikvej, Building 312
2800 Kgs. Lyngby
Tlf. 4525 1700

www.fysik.dtu.dk